SEMMELWEIS EGYETEM

DOKTORI ISKOLA

Ph.D. értekezések

3103.

HORVÁTH CSABA GYULA

Funkcionális Idegtudományok

című program

Programvezető: Dr. Sperlágh Beáta, c.egyetemi tanár

Témavezető: Dr. Fiáth Richárd Balázs, tudományos főmunkatárs

INTERROGATION OF THALAMOCORTICAL CIRCUITS DURING KETAMINE/XYLAZINE-INDUCED SLOW-WAVES WITH HIGH-RESOLUTION ELECTROPHYSIOLOGICAL METHODS

PhD thesis

Csaba Gyula Horváth

Neurosciences ("János Szentágothai") Doctoral School Semmelweis University

Supervisor: Richárd Fiáth, Ph.D

Official reviewers: Péter Ujma, MD, Ph.D
Andrea Slézia, Ph.D

Head of the Complex Examination Committee: Alán Alpár, MD, D.Sc

Members of the Complex Examination Committee: László Acsády, D.Sc
Zoltán Somogyvári, Ph.D

Budapest
2024

Table of Contents

List of Abbreviations

- AHP: Afterhyperpolarization
- AM: Anteromedial nucleus
- AMPA: Alpha-amino-3-hydroxy-5-methyl-4-isoxazolepropionic acid
- APT: Anterior pretectal nucleus
- APTD: Dorsal part of the anterior pretectal nucleus
- AV: Anteroventral nucleus
- AVDM: Dorsomedial part of the anteroventral nucleus
- bsc: Brachium of the superior colliculus
- CA1-CA3: Cornu Ammonis areas 1-3
- CMOS: Complementary metal-oxide-semiconductor
- CL: Centrolateral nucleus
- CM: Centromedian nucleus
- dLGN: Dorsal lateral geniculate nucleus
- EEG: Electroencephalogram
- ECOG: Electrocorticography
- eml: External medullary lamina
- EpP: Epipeduncular nucleus
- FAIR: Findable, Accessible, Interoperable, Reusable
- FRB: Fast rhythmic bursting
- GABA: Gamma-aminobutyric acid

- HPC: Hippocampus
- IGL: Intergeniculate leaf
- IKb: Inwardly rectifying potassium channels
- IKir: Inward rectifier potassium current
- IMA: Intramedullary thalamic area
- INa: Sodium current
- InG: Intermediate gray layer of the superior colliculus
- InWh: Intermediate white layer of the superior colliculus
- K2P: Two-pore-domain potassium channels
- KCa: Calcium-activated potassium channels
- KNa: Sodium-activated potassium channels
- LD: Lateral dorsal nucleus
- LDDM: Dorsomedial part of the laterodorsal nucleus
- LDVL: Ventrolateral part of the laterodorsal nucleus
- LFP: Local field potential
- LGN: Lateral geniculate nucleus
- LPLR: Laterorostral part of the lateral posterior nucleus
- LPMC: Mediocaudal part of the lateral posterior nucleus
- LPMR: Mediorostral part of the lateral posterior nucleus
- MD: Mediodorsal nucleus
- MEAs: Microelectrode arrays
- MEG: Magnetoencephalography
- MGM: Medial part of the medial geniculate nucleus
- MGD: Dorsal part of the medial geniculate nucleus
- MGV: Ventral part of the medial geniculate nucleus
- ml: Medial lemniscus

- MUA: Multi-unit activity
- MZMG: Marginal zone of the medial geniculate
- NMDA: N-methyl-D-aspartate
- NREM: Non-rapid eye movement
- NWB: Neurodata Without Borders
- OT: Nucleus of the optic tract
- PaR: Pararubral nucleus
- PB: Ponto-bulbar
- PLi: Posterior limitans nucleus
- Po: Posterior complex of the thalamus
- PoM: Posteromedial thalamic nucleus
- PoT: Triangular part of the posterior nuclear group
- PP: Peripeduncular nucleus
- PtA: Parietal association area
- REM: Rapid eye movement
- RMS: Root mean square
- Rt: Reticular thalamic nucleus
- SG: Suprageniculate thalamic nucleus
- SNL: Lateral part of the substantia nigra
- SO: Sleep oscillations
- str: Superior thalamic radiation
- SNR: Signal-to-noise ratio
- SubG: Subgeniculate nucleus
- SU: Single-unit recording
- VA: Ventral anterior nucleus
- VG: Ventral geniculate nucleus
- VLG: Ventral lateral geniculate nucleus

- VL: Ventrolateral nucleus
- Vli: Ventral linear nucleus of the thalamus
- VM: Ventromedial nucleus
- VPM: Ventral posteromedial nucleus
- VP: Ventral posterior nucleus
- vMGN: Ventral medial geniculate nucleus
- ZI: Zona incerta

1 Introduction

The phenomenon of sleep remains one of neuroscience's greatest mysteries, despite the fact that almost all species in the animal kingdom spend a significant portion of their lives in this state. Regardless of this, it is difficult to define the specific function of sleep, as numerous competing theories suggest that sleep has no single, well-defined function. It is fundamental to a number of cognitive functions, such as learning and memory consolidation (1-3). However, it is also essential for various metabolic processes that are necessary to maintain homeostasis (4, 5). Consequently, sleep deprivation and disturbances in the complex architecture of sleep are often associated with various psychiatric and other health issues (6).

During my Ph.D. research, I investigated the propagating wave nature of the predominant slow oscillation in anesthesia and natural slow-wave sleep. A rich literature has already described the properties of slow waves before, but in the past, the focus was more on the cerebral cortex. Earlier studies indicate that slow waves propagate primarily from the anterior to posterior regions of the cerebral cortex and that their spatiotemporal dynamics are complex (7). Although the neocortex is considered in the literature to be the primary generator of slow-waves (8-10), it is becoming more evident that the thalamus is involved as a modulator in the generation of slow-waves (11).

My research aimed to ascertain whether slow-wave propagating patterns in the thalamus analogous to those previously observed in the neocortex could be identified. If they appear, we also wanted to know how thalamic propagation patterns differ from cortical slow-wave propagation properties. To address this question first, we used rodent models anesthetized with a combination of ketamine and xylazine. This anesthetic cocktail induces a brain rhythm in rodents and cats with a 1-2 Hz frequency, similar to natural slow-waves but with a more regular and faster frequency (12). Later in the project, we also examined the spatiotemporal patterns of thalamic slow-waves during natural sleep using high-density probes implanted in chronic rodents. By utilizing a single high-density silicon probe capable of simultaneous recordings from multiple thalamic nuclei, it was possible to investigate and visualize the patterns of propagating population activity in the rat and mouse thalamus with high spatiotemporal resolution (13). Furthermore, using simultaneous neocortical and thalamic

recordings in anesthetized animals, I investigated whether there is a noticeable correlation between the spreading patterns observed during cortical up-states and those exhibited by thalamic population activity. In addition, using chronically implanted silicon probes in the thalamus of naturally sleeping rats, I also explored putative propagation activity patterns during slow-wave sleep.

The second study in my doctoral thesis aims to construct a publicly available dataset of high-density *in vivo* electrophysiological recordings from the rat neocortex (14). One of the primary motives of our study is to provide a high-density dataset accessible to the public, which is still scarce in the current neuroscience community. These neural data are presented in a standardized electrophysiological format to aid their reusability. These datasets included wideband raw neuronal recordings as well as data extracted from these raw cortical recordings, such as firing times, extracellular spike waveforms, and various single-unit properties. I included distributions of derived single-unit characteristics and several spike-sorting quality measures for technical validation of this dataset. In the future, such high-density *in vivo* datasets may help answer several neuroscientific questions, such as the exploration of the detailed electrical signatures of cortical neurons, potentially enhancing their classification based on electrophysiology. Furthermore, the dataset could be utilized to investigate the layer-specific neuronal activity associated with slow oscillations.

1.1 Topics overview

A brief summary of the content will be provided to enhance the thesis's readability and comprehension. Following the introduction, in the second chapter, I will give a general outline of the anatomical and physiological background essential for understanding the relationships between the structures forming the cortical-thalamocortical system. Emphasizing the thalamic nuclei, which we have covered extensively in our work. In the third chapter of this assignment, I will go into the details of the linkage between the thalamocortical system and sleep, with a particular focus on the brain oscillations taking place in sleep and under anesthesia. In the fourth chapter, I will discuss the properties of slow oscillations during anesthesia and natural sleep. There will also be a short technological overview of high-density neural probes and what they offer to comprehend neural networks. This section will also emphasize the importance of data sharing in neuroscience, point out standards and storage options for sharing data, and describe ways of ensuring that data formats and metadata are kept uniform to facilitate both the sharing of data and its reuse and integration.

The results are presented in two main parts: The first study was designed to explore the propagating wave nature of the dominant slow oscillation occurring under anesthesia and during natural slow-wave sleep. In contrast, the second study explains the creation process of a publicly available database of high-density, in vivo electrophysiological recordings from rat neocortex. I review the two studies' main findings, limitations, and open questions in the discussion and conclusion sections. In conclusion, I discuss future possibilities and the applicability of the results.

1.2 Cortico-thalamocortical system

The neocortex and the thalamus form a uniquely reciprocal connectivity system. In the following chapter, I will outline the cortical-thalamocortical system. This chapter will cover the general anatomical and functional organization of the two main structures, the thalamus, and the cerebral cortex, at both the network and cellular levels. It will provide an overview of the thalamus's major pathways and the potential distribution systems of its nuclei. We will observe that the thalamus is a significant regulator of information flow in the nervous system. The various first-order or higher-order thalamic nuclei extend axons to virtually all cortical areas. Corticothalamic outputs can originate from layers 6 and 5 of the cortex and serve different functions in the thalamus, as demonstrated in the following sections (15-17).

1.2.1 The diencephalon

The diencephalon, along with the telencephalon and hypothalamus, is one of the principal structures of the forebrain. Developmentally, it can be subdivided into three segmental domains known as prosomeres (P1-P3). Based on gene expression profiles, these segments are numbered from rostral to caudal (18-22). The diencephalon can be further subdivided into regions according to their relationship with the cerebral cortex, which includes the dorsal, ventral, epi-, and hypothalamic regions. In my study, I will focus on the dorsal part, which corresponds to the P2 prosomere (23).

1.2.2 The dorsal thalamus

For the remainder of this thesis, I consistently refer to the dorsal thalamus as "thalamus" as per scientific nomenclature. It is a substantial structure located in the diencephalon, nestled between the highly developed cerebral cortex and the evolutionarily older hindbrain along the third ventricle. It represents the largest symmetrical structure of the diencephalon, with varying degrees of fusion via the adhesio interthalamica depending on the species. The dorsal thalamus is a complex brain region that defies easy classification. Early approaches focused on the anatomical divisions of its nuclei; however, it is now clear that thalamic nuclei do not have distinct functions but serve as intricate participants in different neural processes (24). A modern classification scheme focuses on connectivity: nuclei are grouped according to

whether we study their inputs or outputs. More detailed classification within these categories depends on the specific aims of the analysis (25, 26).

1.2.3 Dorsal thalamic connectivity

1.2.3.1 Thalamic input pathways

The classification of thalamic nuclei reveals a highly complex and heterogeneous functional relationship between the cortex and thalamic nuclei, which is now understood to be more elaborate than a simple reciprocal relationship. Besides the subcortical sensory input, it is also important to note that the cortex provides the vast majority of input to the thalamus. This input is projected back reciprocally to the part of the cortex from which it originated in a topographical manner (27-29).

The thalamus integrates inputs from various brain structures with diverse properties to generate novel information, which is then relayed to the cortex via a pathway without a clearly defined canonical route. The relationship between the two structures allows a wide range of cognitive processes to emerge (29).

The heterogeneity of inputs to thalamic nuclei is well illustrated by comparing first-order (classical "relay") and higher-order nuclei. For instance, in the somatosensory system, first-order nuclei, such as the ventral posteromedial nucleus (VPM), receive subcortical primary input that terminates with multiple synapses on proximal dendrites. The final outputs are shaped by modulatory cortical layer 6 inputs and GABAergic inputs from the thalamic reticular nucleus. In contrast, higher-order nuclei have much more diverse inputs. The posteromedial complex (PoM) receives excitatory input from layer 5 of the somatosensory cortex, which has properties similar to “driver” inputs, which typically originate from subcortical regions. Additionally, they receive strong inhibitory inputs from the zona incerta (ZI) and the anterior pretectal nucleus (APT) (30-32). It now seems that different integration patterns can be found within the thalamus and even among nuclei. The assumption that the integration processes are much more extensive than the transmission of topographic information from receptor surfaces is closer to reality.

1.2.3.2 Thalamic output pathways

Thalamocortical neurons are considered the primary cell class of the thalamus and form a phenotypically homogeneous group. From an evolutionary perspective, these cells originate from a common neuroepithelium in the dorsal thalamus, while thalamic GABAergic interneurons migrate into the thalamus at a later stage of individual development (18, 33, 34).

It is important to note that, unlike primates, the presence and proportion of interneurons in the thalamus of rodents is negligible. The dorsal lateral geniculate nucleus (dLGN) is the most abundant, while the other nuclei have practically no interneurons (35). The thalamic outputs primarily project to cortical layers 4 and 6 but provide glutamatergic input to the whole cortex, except for the gyrus dentatus and CA1-CA3 regions. In addition to their role in neurotransmission, the electrical conduction properties of their cell membranes are also consistent. Somatodendritic morphology is also highly conserved with correlated function, and the cell body typically appears large while the shape is fusiform or polygonal (36). A "bushy" layout characterizes the dendritic arborization of the cells (27, 37). Notably, thalamocortical neurons do not establish excitatory recurrent connections among themselves (38); their inputs mainly determine their role as integrators and mediators, while they are modulated by the interneurons localized within each nuclei.

The diversity of thalamic outputs is reflected not in the soma or dendrites but in the wiring motifs of the axons. The thalamocortical axons leave the thalamus in an anteroventral or lateral direction without forming connections with adjacent cells and nuclei. In contrast, all thalamocortical cell axons pass through the reticular nucleus. Some axons may also give branches to different basal forebrain structures, such as the amygdala and ventral pallidum (39, 40). Once they reach different layers of the cerebral cortex, characteristic axon-wiring motifs can be found that determine the functionality of cells and their respective nuclei (41, 42). The variability of thalamocortical axonal motifs is determined by their branching patterns to different structures. Thalamic axons can be divided into two major groups based on the location of their synaptic regions of axons can be found. According to the definition, the two main groups are thalamocortical and thalamostriatal neurons. Thalamocortical neurons have most of their varicosities located in one of the cortical layers, while

thalamostriatal neurons have most of their terminals located in the striatum. The monofocal motif is primarily found in thalamocortical axons originating from the first-order nuclei, such as the ventral lateral nucleus (VL) and the dorsal lateral geniculate nucleus (dLGN) (43, 44). Except for the thalamocortical neuron, these axons typically do not provide collateral branches to other subcortical areas. They terminate in a well-defined cortical space with focal arborization. In the cortex, lateral branching forms diverse terminals in the third and fourth cortical layers, where they establish single or multiple synaptic connections with the dendrites of cortical glutamatergic and GABAergic cells (41, 45, 46).

The multifocal thalamocortical axonal pattern, unlike the monofocal arrangement, is not confined to a specific area. The axonal branches (2-5) of these neurons can form a diverse and extensive arborization across various layers of the cortex, including distant regions. Some axons can also extensively innervate subcortical regions (45, 47, 48). Multifocal axonal wiring is the dominant pattern for thalamocortical neurons in rodents, particularly in nuclei such as the posterior nucleus (Po), lateral posterior pulvinar (LP), dorsal medial geniculate (MGD), ventral lateral (VL), lateral dorsal (LD) and mediodorsal (MD) (47, 48).

The third morpho-type involves thalamocortical axons that innervate the first cortical layer with flat subpial branches, establish less elaborate axon arbors on the apical dendritic spines of pyramidal cells (49), as well as on the interneurons present in these layers (50). In the literature, subpial thalamocortical axons are also known as matrix axons (27, 51, 52) or M-type axons (53). In certain cases, small type I arborizations are formed in the striatum by subpial thalamocortical axons (54).

1.2.4 Classification of thalamic nuclei relying on thalamocortical input

The thalamic nuclei classification underwent significant changes in the mid-1990s, following the work of Sherman and Guillery (55). In the past, the thalamus was considered primarily responsible for filtering signals from subcortical regions and transmitting them faithfully to the cerebral cortex. The thalamic nuclei that transmit information from sensory or motor subcortical sources are referred to as first-order nuclei. However, this definition has been revised following the recognition of higher-order thalamic nuclei, which create reciprocal

connections with association cortical areas and transmit complex, processed information to the cortex.

The inputs that determine the operation of cells within a given thalamic nucleus are commonly referred to as "driver" inputs. In addition to these driver inputs, each thalamic nucleus receives "modulatory" inputs that influence signal processing (55, 56).

The thalamic nuclei can be divided into two main types: first-order nuclei receive their "driver" inputs from mainly peripheral sensory modalities. These signals are then projected into a well-defined region of the 4th layer of the cortex - the cortex. In parallel, the first-order nuclei also receive modulator inputs from layer 6 of the cortex. Except for olfaction, each sensory modality has its first-order thalamic nucleus. Notable examples include the dorsal lateral geniculate nucleus (dLGN), which processes visual information from the retina, and the ventral part of the medial geniculate nucleus (vMGN), which processes auditory information from the inferior colliculus or the first-order somatosensory nucleus the ventral posteromedial nucleus (VPM) (55, 56).

In contrast, higher-order thalamic nuclei receive their 'driver' inputs from layer 5 of the cortex as processed signals, which are reciprocally reflected back to the appropriate cortical regions, and modulator inputs from layer 6, like first-order thalamic nuclei. However, this classification system is not entirely rigid. Some higher-order thalamic nuclei receive their “driver” inputs not only from layer 5 but also from subcortical areas, which also function as “drivers”. For example, the mediodorsal nucleus receives driver input from the superior colliculus (25, 27, 53, 57-60).

1.2.5 Classification of thalamic nuclei relying on thalamocortical output

The classification based on outputs categorizes thalamocortical projections into two main types: core and matrix categories (51). Core-type projections, which resemble first-order nuclei, densely innervate the middle layers of the cortex within a well-defined spatial area. They primarily project sensory input to the primary cortical sensory areas. Examples of such nuclei include the lateral geniculate nucleus (LGN) and the ventral posterior nucleus (VP). In contrast, higher-order nuclei often overlap with matrix-type nuclei, they receive their

primary input from the cortex and project to secondary and associative cortical areas within cortico-thalamic-cortical loops. These nuclei are also characterized by extensive, diffuse projection patterns to cortical areas that allow them to be more involved in modulating cortical activity rather than simply relaying sensory information. Examples of such nuclei include the mediodorsal nucleus (MD) and intralaminar nuclei (e.g., the centromedial nucleus, CM) (39, 47, 48, 61).

1.2.6 Biophysical properties of thalamic cells

In addition to the anatomical and functional bases for differentiation, thalamic neurons also possess unique intrinsic electrophysiological properties that significantly influence the dynamics of their networks. This supports the concept that thalamic cells from different nuclei cannot substitute for each other, even if they use the same neurotransmitter (62).

The passive and voltage-dependent intrinsic properties of thalamic neurons significantly influence their ability to integrate information and their subthreshold spontaneous activity. The function of various active ion channels defines the resting membrane potential below the firing threshold of neurons. The hyperpolarization of cells is primarily due to the background potassium current (IKb) generated by members of the two-pore potassium (K2P) channel family and the steady-state current generated by inward-rectifying potassium channels (IKir). Conversely, the depolarization of cells is influenced by three ion currents: the Ih (hyperpolarization-activated cationic current generated by hyperpolarization-activated cyclic nucleotide-gated [HCN] channels), IT (low-threshold calcium current generated by CaV3 channels), and INa (sodium current generated by NaV channels). The resulting resting membrane potential is species- and cell-specific due to varying gene expression patterns (63). In rodents, thalamocortical neurons resting membrane potential of approximately -70 mV (64), while interneurons are more depolarized at -65 mV (65). The subthreshold ion currents in the thalamocortical network play a crucial role in developing oscillatory and resonant functions (66, 67). The integrative capacity and excitability of neurons are also largely determined by their membrane resistance which similarly exhibits species and cell specificity. Rodent first-order thalamic neurons display a resistance of 100-150 MΩ, whereas interneurons show 300-550 MΩ (65, 68-70).

Examining thalamic cells in terms of their electrical properties reveals significant differences. Thalamocortical neurons are electrically compact when examined from the soma. Local membrane potential changes originating from the dendrites are almost completely attenuated; conversely, potential changes from the soma induce only a minimal damping response in the dendrites (71). In contrast, thalamic interneurons possess different properties, showing a much stronger voltage-damping effect between the distal dendrites and the soma. This could support the notion could support the notion that interneuron dendrites and somas perform independent input and output processing (72).

1.2.6.1 Modes of action potential generation in thalamic neurons

Thalamic neurons are capable of generating two distinct action potential patterns in a state-dependent manner. The cells show burst activity in their hyperpolarized state, while in a depolarized state, they display tonic activity. Burst activity is most characteristic during various phases of slow-wave sleep, where low-frequency (<15 Hz), high-amplitude oscillatory patterns can be observed in the recorded signals. These grouped high-frequency action potentials are shaped by the cyclic interactions of membrane currents (involving CaV3, HCN, and Ca2+-activated K+ channels). During rapid eye movement sleep and wakefulness, tonic action potentials are prevalent, but burst activity can also be recorded during wakefulness (71). Furthermore, it is crucial to emphasize that bursting can serve as an indicator of various neurological and psychiatric disorders, including Parkinson's disease, epilepsy, and depression (73). Studies have demonstrated that the action potential patterns of cells within the thalamus are not uniform; these can vary among nuclei and cell types. Generally, it is observed that neurons expressing parvalbumin but not somatostatin are characterized by burst firing (74). These variations are likely determined by different modalities and their respective positions in the thalamocortical hierarchy (75).

1.2.7 Functional roles and connections of key dorsal thalamic nuclei

The following paragraphs will outline the significant relationships and functions of the dorsal thalamus, the nuclei that receive our primary focus in this research. It should be noted that numerous other nuclei and regions are involved in the study, they will not be discussed in

detail here. This section aims to enhance the understanding of the relationship between these nuclei of the cortex and thalamus and the interactions between the nuclei discussed.

Comparative analysis of the thalamus across species can be a challenging task because, in some cases, specific nuclei may be absent in certain species, and analogous nuclei and areas may fulfill their functions. A typical example of this phenomenon is the pulvinar, which is found in most mammals but is absent in most non-mammalian species. In rats and mice, the lateral posterior nucleus shows notable homologies with the pulvinar (76). Conversely, primates lack the POm nucleus, and its function is fulfilled by the anterior pulvinar and the VPL and VPM nuclei (77). The most frequently involved nuclei in our experiments have been identified as prominent actors in processing somatosensory information, operating in various ways. In rodents, the two nuclei of the ventroposterior nuclear complex, VPL and VPM, play a vital role in relaying somatosensory information. The VPL nucleus is responsible for relaying information associated with the body via the medial lemniscus tract. In contrast, the VPM nucleus in rodents transmits information from the facial whiskers along the trigeminothalamic tract in a highly topographic manner to the primary somatosensory cortex (78, 79).

In contrast to the VPM, the POm nucleus plays a far more complex role, participating as another element within the somatosensory system. Unlike the VPM, the POm is also influenced by significant excitatory inputs from the fifth layer of the primary somatosensory cortex (30). It is important to note that the final output of the POm is greatly influenced by the ZI (32) and the anterior pretectalis nucleus (APT) (31). The cortical target areas of POm axons exhibit greater heterogeneity than those of VPL projections, with inputs observed in both the first layer of the cortex and layer 5A (58, 80).

The laterodorsal nucleus and its subregions were one of the primary focus of investigation in our experiments. The LD nuclei receive the majority of their afferents from various structures that convey visual information, including the superior colliculus and the ventral lateral geniculate nucleus (81). The nucleus has been the subject of only a limited number of studies, the findings suggest that its functions extend beyond the mere transmission of visual information. In rats, the ventral lateral part of the nucleus (LDVL) receives input from both

the primary and secondary visual cortex, whereas the medial part does not (82). In mice, the LD also projects to all visual cortical areas (83). Other theories propose that the LD, through its connection with the hippocampal system, is associated with memory and learning, particularly for spatial tasks. Injuries or lesions affecting this region result in a corresponding loss of spatial memory (84-86). The evidence above suggests that the LD is a multisensory nucleus that may play a prominent role in spatial orientation and learning (87).

The nuclei involved in motor tasks were also examined, including two of the most prominent nuclei in rodents: the Ventral Anterior (VA) and Ventral Lateral (VL) nuclei. Both nuclei are responsible for processing motor information transmitted via the thalamus (27). The primary function of the VA nucleus is motor planning and movement initiation, which sends information from the basal ganglia and globus pallidus to the motor cortex (15). Moreover, it plays a crucial role in coordinating movement (88). The VL nucleus performs a comparable function, with significant connections to the cerebellum and motor cortex (89). Its primary role is to fine-tune proprioceptive information from the cerebellum and aid in motor execution. Furthermore, the VL nucleus influences muscle tone and fine motor control (89, 90).

Additionally, the auditory nucleus of the thalamus, specifically the medial geniculate nucleus (MGN), and its constituent subregions were covered. The dorsal part of the nucleus functions as a multimodal processing unit for analyzing auditory stimuli.

The dorsal part of the nucleus is involved in processes such as the perception, localization, and recognition of sound patterns (91). The middle part of the nucleus is associated with the emotional and behavioral components of hearing through its connections with the amygdala and hypothalamus.

Important phenomena influenced by this region include fear conditioning and responses to alarm signals, as well as other processes related to stress response and emotional learning (92). The ventral part is pivotal in analyzing sound frequencies and temporal resolution, with its topographic frequency representation enabling the auditory cortex to process sound accurately (93).

Among the nuclei examined, the thalamus's DLG (dorsalis lateralis geniculatus nucleus) displayed notable involvement. This nucleus is critically linked to the processing and transmission of visual information to the cortex, serving as the primary relay station for visual signals from the retina to the primary visual cortex (V1). The DLG is topographically organised, allowing for a precise representation of the visual field. It plays a crucial role in maintaining essential aspects of visual perception, including spatial resolution, contrast sensitivity, color perception, and motion detection. The neuronal activity of the DLG is significantly influenced by the regulation of visual attention, enabling the enhancement of relevant visual stimuli and the suppression of irrelevant ones. Additionally, the DLG is implicated in the temporal and spatial processing of visual information, which is essential for interpreting complex visual scenes and ensuring accurate visual perception (43, 94).

1.2.8 The architecture of the cerebral cortex: morphology and function

The cerebral cortex is the site of high-level cognitive functions. It can be divided into six main layers depending on the species (95) and cortical region (96). Additionally, the structure of these individual layers may vary or even be absent in specific brain regions, highlighting the structural complexity of the cortex. The thickness and boundaries of these layers, as well as their cellular composition, vary within species depending on the functionality of the particular brain area. Although there are some similarities between different species, significant differences can also be observed in the appearance of these layers . Phylogenetically, it is the youngest part of the cerebrum. Significant variation in structure and cellular composition exists across different brain regions (97, 98). Although regional differences exist in the layers, the main cell types and their connections are relatively uniform across all cortical areas. One of the characteristic features of the human brain is gyrification, which increases surface area and compactness, optimizing space utilization. Modern experimental techniques have further subdivided the neocortex into sub-layers that go beyond the concept of a simple division into six layers (99)(Lorente de No 1949). The thickness of the human cortex varies from 1.3 to 4.5 mm depending on the brain region, with an average thickness of 2.5 mm (97). Commonly used model animals, such as mice (~1.5

mm) and rats (~2 mm), have thinner cortices that are not gyrated, in contrast to the human cortex (100).

Layers from top to bottom:

I. Molecular layer (*lamina molecularis*) – a layer with few neurons. Here we find the dendritic bodies of the pyramidal cells and horizontal axons.

II. Outer granular layer (*lamina granularis externa*) - consists of stellate cells and small pyramidal cells whose apical dendrites terminate in layer I and send their axons to the lower cortical layers.

III. Outer pyramidal layer (*lamina pyramidalis externa*) – characterized by large and medium-sized pyramidal cells.

IV. Internal granular layer (*lamina granularis interna*) - mainly spiny stellate cells, the upper part (IVa) contains medium-sized pyramidal cells and stellate cells, while the lower part (IVb) is almost exclusively stellate cells. The outer Baillarger band is located here and consists of the axon terminals of the thalamocortical cells. These fibers terminate in the dendrites of the stellate cells of layer IV, the basal dendrites of the pyramidal cells of layer III, and the apical dendrites of the pyramidal cells of layers V and VI.

V. Inner pyramidal layer (*lamina pyramidalis interna*) - contains the largest pyramidal cells of the cerebral cortex—a significant source of projecting fibers to subcortical areas. The pyramidal cells frequently give rise to intracortical connections by axon collaterals.

VI. Multiform layer (*lamina multiformis*) - small pyramidal, stellate, and fusiform cells are found. Their axon either exits into the white matter and forms short association fibers or projects into other cortical layers. The pyramidal cells in this cortical layer also give rise to many of the corticothalamic connections

The complex cortex tissue comprises cells exhibiting diverse morphologies and multiple functions, which can be divided into two main groups. The first group includes the excitatory pyramidal cells, which release glutamate (70, 101). The second group comprises the interneurons, which communicate via the release of gamma-aminobutyric acid (102). Neurons can be subdivided into subsets based on several criteria. One method is by their electrophysiological properties. In both *in vivo* (103-105) and *in vitro* (106, 107) conditions, cells can respond to depolarizing current pulses with various firing patterns. It is important to recognize that specific firing patterns are not fixed within certain cells. Cells may exhibit atypical patterns depending on the activity of different neurotransmitter systems or momentary alertness levels (103). In general, pyramidal cells tend to have regular firing patterns, while inhibitory interneurons typically display rapid firing patterns. Furthermore, neurons have been observed to exhibit intrinsic bursting (IB) and fast rhythmic bursting (FRB) (104, 108).

We can also base our classification of neurons on morphological characteristics. The best-known cortical cell type is the pyramidal cells, named after the shape of their soma. As to their dendrites, these cells have an apical dendrite that extends toward the upper layers of the cortex. Most apical dendrites reach the first cortical layer, with the except for those in layer 6 pyramidal cells, that only extend to layer 4 (98). From the basal part of the cells, dendrites originate that move downwards and then branch out in a star-like fashion not far from the soma. Their axons extend from the basal part of the cell body towards the white matter. Pyramidal cells can also be further divided based on size into: small (1-12 μm), medium (20-25 μm), large (45-50 μm), and giant (70-100 μm) pyramidal cells. Interneurons form an exceptionally heterogeneous group of cells. The classification of interneurons is a challenging task, and there are several ways of classifying them into different groups. Their classification can be based on dendritic and axonal morphology (109, 110) or on immunohistochemical markers, including calcium-binding proteins (e.g., parvalbumin, calbindin) and neuropeptides (e.g., somatostatin, vasoactive intestinal polypeptide) (111). Moreover, the projections of neurons are characteristic, based on which we distinguish "basket cells" that target the perisomatic regions of pyramidal cells, while axo-axonal cells

terminate at the initial segment of axons (102, 112). In addition, there is a high degree of variability in their electrophysiological properties and more than a dozen firing patterns have been described to date (113). The interaction between pyramidal cells and inhibitory interneurons establishes the foundation of cortical information processing. Pyramidal cells provide the cortex's output and integrate information, while interneurons modulate these processes.

Along with with the many forms of excitatory and inhibitory neuronal cell types, the other glial cells in the brain are not to be underestimated. These cell types are now viewed as essential active players in many neural processes. The human brain is estimated to consist of about 100 billion glial cells, about tenfold the number of neurons (114). Most glial cells are oligodendrocytes (75.6%), responsible for the myelination of axons. Astrocytes, essential for healthy neural function and synaptic activity, constitute approximately 17.3% of the total glial cell population, while the least numerous are the brain's immune cells, the microglia (115).

1.3 Thalamus and sleep

1.3.1 Sleep

Sleep is an evolutionarily conserved physiological state that entails periodic disconnection from external stimuli for all organisms possessing a nervous system. This endogenous process is maintained by systems responsible for circadian rhythms and homeostasis (116). Genetic studies suggest that sleep's biochemical players and functional roles are highly conserved. In most organisms, it plays a crucial role in metabolic processes (117), memory consolidation (1), and even during ontogeny (118). In higher organisms, like mammals, with a more complex nervous system, species-specific stereotypic behaviors show up during sleep in postural changes and reduced overall motor activity and disconnection from external stimuli (119, 120). However, the presence of sleep or sleep-like functions in organisms with varying levels of organization and evolutionary advancement, such as jellyfish (121) or even sponges (122), suggests that these functions are fundamental across multiple scales.

1.3.1.1 The macro- and microstructure of sleep

In 1968, Rechtschaffen and Kales defined human sleep states in their sleep guidelines, which have been refined by the American Sleep Research Association's sleep guidelines (123). In terms of chronobiology, human sleep follows ultradian rhythmicity, alternating rapid eye movement (REM)-nonrapid eye movement (NREM) phase in 60-120 minute cycles during the night (124). During the electroencephalogram (EEG), it is seen that a synchronized, high-voltage, low-frequency activity characterizes NREM. On the contrary, REM has low-voltage, high-frequency background activity of lesser synchronization. Hypnograms are frequently used for graphical representation of these sleep stages and the course of changes during the night (Figure 1.).

In humans, the NREM stage can further be subdivided into three sub-stages (123). These stages progress from a state of superficial sleep to a state of deep sleep. The first sleep cycle phase, NREM 1, characterizes the transition from wakefulness to sleep. In this phase, alpha waves (8-12 Hz) are gradually replaced by slower theta waves (4-8 Hz). The metabolic activity falls, and other physiological parameters decrease, such as heart rate and respiration.

Stage 2 of NREM demonstrates the continuation of physiological parameters decreasing and dissociation from the environment and sensory inputs. Sleep spindles and K-complexes will be characteristic of the thalamocortical network. Background electrical activity slows, with theta waves giving way to delta rhythms (1-4 Hz).

Stage 3 NREM is also referred to as deep sleep or slow-wave sleep (SWS). This stage is characterized by an increase in the power of delta waves (1-4 Hz), with the emergence of slow-waves below 1 Hz. The frequency of both K-complexes and sleep spindles decreases while muscle tone continues to decline. The NREM3 constitutes 15–25% of total sleep time.

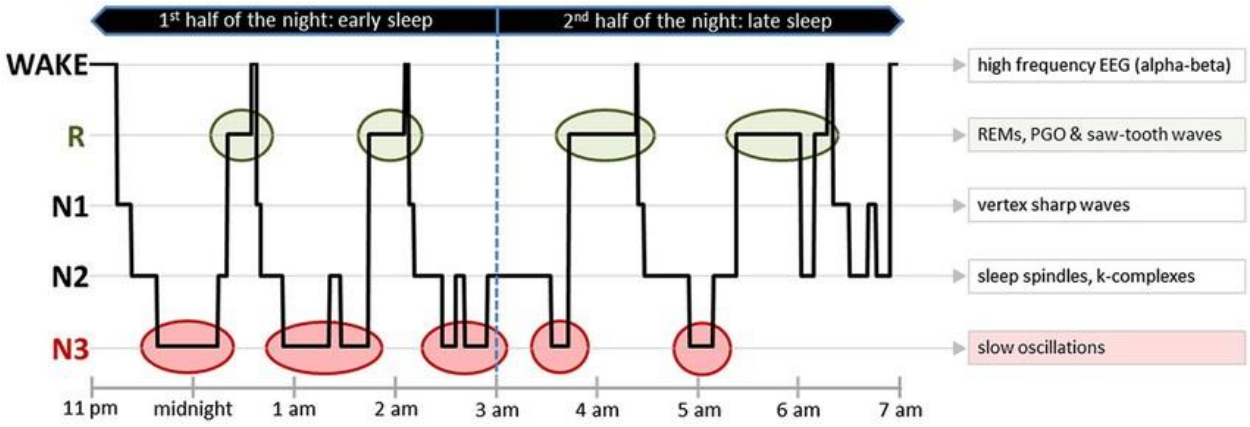

Figure 1. *A typical healthy human hypnogram illustrates the stages of an 8-hour sleep cycle. On the right edge of the figure, typical electroencephalography (EEG) elements and electromyography (EMG) and electrooculography (EOG) activity patterns are displayed, which are indicative of the sleep phase. Abbreviations: EEG: electroencephalography; EMG: electromyography; EOG: electrooculography; REMS: rapid eye movements; PGO: ponto-geniculo-occipital waves (125).*

Following this, sleep is gradually less restorative, and it usually proceeds to REM sleep, which makes up about 25% of the total sleep time. During REM, brain activity is much like during wakefulness, hence the term 'paradoxical sleep' (126). The total loss of muscle tone (atonia), ponto-genicular-occipital (PGO) waves, and a hippocampal theta rhythm of 4-10 Hz characterize REM sleep. The cardiac and respiratory rates become irregular and increase rapidly, as do cerebral blood flow and brain temperature.

In contrast to humans, rats and mice are active and polyphasic at night, with their individual sleep episodes and NREM-REM cycles being much shorter. The sleep cycles of rats are approximately 10 minutes long, while those of humans range from 60 to 120 minutes (127). The electromyogram (EMG) activity or movement of certain animals is employed to distinguish between wakefulness and sleep. The method then divides sleep periods into NREM and REM states by calculating the theta/delta spectral power ratio, utilizing three main sleep stages (wakefulness, NREM, and REM; see Figure 1). This process does not involve further division of states. The fundamental structure of sleep, comprising alternating states (NREM and REM), is conserved in rodents. However, there are biological differences and discrepancies in nomenclature.

1.3.2 The function and physiology of sleep

Although a significant part of our lives is in this state, its function is unknown. Sleep is not a uniform biological phenomenon and cannot be ascribed to one reason. It has different functions in organisms to varying levels of their organization. Hypotheses on the role of sleep can be divided into two groups. One group usually includes cognitive processes, such as memory, and those related to brain plasticity (128). The other major group constitutes processes associated with the maintenance of the integrity of the organism's other systems, for example, metabolic regulation (117), thermoregulation (4), detoxification (5), and participation in immune processes (6).

Inadequate quantity and quality of sleep may lead to considerable and diverse disturbances in both cognitive and emotional processes (129). However, defining and disentangling the cause and effect of 'oversleeping' associated with increased sleep time can be very complex. Interestingly, prolonged sleep is likely to correlate with increased mortality and cardiovascular disease (130).

1.3.3 Thalamocortical oscillations in sleep

In humans, NREM sleep can be divided into several substages (N1-3) with a characteristic cortical EEG fingerprint and a homogeneous pattern in rodents. A detailed analysis of the data obtained from the cortical electroencephalogram (EEG) recordings reveals a gradual

decline in the frequency of oscillations during the N1 stage. This decline commences with gamma oscillations (25-80 Hz) and beta oscillations (15-25 Hz), subsequently progressing to alpha oscillations (8-11 Hz) and theta waves (4.0-7.5 Hz). In the N2 stage, there is also a progressive shift in the amplitude of the waveforms and the appearance of two thalamocortical waveforms, the sleep spindles (11-14 Hz) and the K-complexes, which are sharp biphasic high-amplitude events, well-defined and lasting more than 0.5 seconds. In comparison, the third phase is dominated by high-amplitude slow oscillations (<1 Hz) and delta waves (1.0-4.5 Hz) (8).

The low-frequency, high-amplitude wave activity is characteristic of slow oscillatory rhythm, primarily but not exclusively associated with natural deep sleep (131). This pattern is highly present in EEG recordings during anesthesia. The first descriptions of that phenomenon were performed in rat models (132), and leading work by Mircea Steriade and colleagues in cats led to comprehensive exploration (8-10).

1.3.4 Slow oscillation

The slow oscillation (<1 Hz) can be considered a fundamental phenomenon of the mammalian cortex, which is expressed during NREM sleep and anesthesia. In animals, it is most prominent during the NREM phase, which in humans is most pronounced in the third and deepest phase of NREM (slow-wave sleep) (104, 123). Slow oscillation is a phenomenon observed in well-coordinated neuronal populations, characterized by rhythmic cycle of phases of increased cellular and synaptic activity (up-states) followed by hyperpolarization and cell silence (down-states) (108). As observed in animal models, similar phenomena occur in humans, with up-states accompanied by increased alpha and beta power relative to down-states (7, 133). Regarding rhythmicity, there is a distinction between animals and humans. In animals, the slow oscillation is considered to be below 1 Hz (8). However, this range is between 0.5 and 2 Hz in humans, according to the American Academy of Sleep Medicine guidelines (123). Another significant distinction is that the mean firing rate of neurons during the human up-state is only a tiny fraction of that observed in animal studies (134, 135).

In the past, there was a general consensus that slow oscillation originated from the cortex. However, recent results have significantly complicated this view. The possibility of a cortical origin was already proposed by Steriade and colleagues, who observed that slow oscillation persists even with a disrupted connection between the thalamus and the cortex (8). Most observations indicate that the origin of the slow oscillation is mainly due to the involvement of the cortex as the primary generator. Moreover, the cortex can generate this slow oscillation pattern independently of subcortical input, as evidenced by the findings of most lesion studies and *in vitro* experiments on slices (136). It is, however, essential to note that the thalamus, which plays a prominent role in the fine regulation of this global and synchronous activity, is significantly affected by uncoupling, especially in terms of reduced frequency and the initiation of up-states (11).

Several possible concepts have been proposed based on observations of the mechanisms underlying the formation and initiation of up-states. Among the two leading hypotheses, the 5th layer pyramidal cells play the pivotal role, performing a constantly active pacemaker-like function. It is also noteworthy that Lőrincz and colleagues discovered that during up and down-states in mice, a distinct subset of layer 5 regular spiny pyramidal neurons fires earlier than other neuron types (137). This suggests that these neurons may play a role in inducing up-states, consistent with intracellular recordings in anesthetized and sleeping cats during slow oscillation, showing that these cells often fire before all other recorded neuronal types prior to the onset of the up-state (12). The other leading hypothesis is that spontaneous synaptic activity may accumulate over time, resulting in the initiation of the up-state phases. Despite basic similarities, in humans the initiation of up-states occurs in the supragranular layers of the cortex, whereas in rodents and cats it originates from the infragranular layers (138-140). In humans, it has been observed that the onset of up-states is a relatively synchronous event in the cortical layer, as previously observed in intact animals (139, 140), whereas a delay was observed in slices or under anesthesia (136).

A possible mechanism for initiating the up-state state is the temporal accumulation of spontaneous, action potential-independent stimulatory synaptic potentials on a sufficient number of layer 5 pyramidal cells (141). Another possibility is that some layer 5 pyramidal

cells fire continuously during the down-state. These neurons translate the rest of the network into the up-state after quasi-network refractor mechanisms allow. There is no complete agreement on this in the related literature. Studies in anesthetized cats using intra- and extracellular recordings to characterize down-states have found no firing activity in layer 5. The above-mentioned findings are inconsistent with *in vitro* observations where spontaneous firing has been detected (136) and *in vivo* rodent studies (139, 142).

The persistence of the up-state is most often associated with synaptic activity, which is most likely supplemented by intrinsic membrane properties (143, 144). It is likely that a delicate equilibrium of excitatory and inhibitory synaptic activity has evolved to a membrane potential that maintains the network at the edge of the firing threshold.

It seems that the activation of AMPA (Alpha-amino-3-hydroxy-5-methyl-4-isoxazolepropionic acid) and NMDA (N-methyl-D-aspartate) receptors is crucial for the maintenance of up-states. In their 1993 *in vivo* study of cortical slow oscillations, Steriade and colleagues also indicated that when urethane anaesthesia was administered in combination with ketamine, the up-states were shortened by more than half (145). This finding is further supported by studies where baths with different NMDA antagonists almost abolished slow oscillations in brain slices (136, 146, 147).

In different species, the ratio of excitatory and inhibitory inputs involved in the formation of the membrane potential required to sustain up-state is variable. In general, it is observed that the excitatory and inhibitory conductances are varied concurrently and proportionally in such a way as to maintain the membrane potential close to the firing threshold. In rodents, a dominance of excitation was observed, especially in the first half of the up-states. Neske and colleagues an *in vitro* study, which demonstrated that inhibition was dominant in the deep and superficial layers of the mouse barrel cortex in vitro in a 2:1 ratio (148). In urethane-anaesthetized rats, however, the ratio of excitatory inputs to up-states was significantly higher in the superficial layers (149). In contrast, in the deep layers of the parietal association cortex of sleeping cats, inhibitory conductance strongly dominated excitatory conductance in a ratio

of 10:1 during most of the up-state (150). The excitatory and inhibitory conductance in deep layers of ferret prefrontal and visual cortex *in vitro* (141) and in deep layers of the prefrontal cortex in ketamine-xylazine-anesthetized ferrets (151) were largely similar throughout the up-state, except at the onset and termination of the up-state, where excitatory conductance became dominant.

Similarly to the questions associated with the initiation and persistence of up-states, the termination of the up-states raises a number of open questions. The key question is whether synaptic or intrinsic cellular mechanisms are responsible, or perhaps a combination of the two. On the synaptic aspect, increased inhibition by interneurons or depression of excitatory inputs may be important, while on the cellular aspect, activation of activity-dependent hyperpolarizing conductances may play an important role, as already hypothesized in the early description of cortical slow oscillation (10). Activity-dependent K+ channels, such as Ca2+-dependent K+ (KCa) and Na+-dependent K+ (KNa), play a cardinal role in the termination of up-states through their formation of long-lasting after-hyperpolarizations (AHP) (136, 152). This finding is supported by a number of studies using *in vitro* and *in silico* models. Through activity-dependent K+ currents in cortical pyramidal cells, a generalized dysfacilitation is induced, leading to the termination of up-state.

1.3.5 Thalamocortical slow oscillation during anesthesia

Several possibilities exist for a complex investigation of oscillatory patterns in slow-wave sleep. Slow oscillations can appear in all stages of natural sleep, but they can also be registered during wakefulness. Additionally, studies with different anesthetics serve as plausible models for slow oscillation research. Anesthetics produce a wave pattern with parameters broadly similar to those of natural slow-wave but differ in several quantitative characteristics, such as frequency and amplitude, that are significantly different not only from natural slow-wave activity (SWA) but also among particular anesthetics (9, 11, 12, 153-156).

1.3.5.1 Ketamine and xylazine

In our studies, we applied one of the most widely used intravenous anesthetics in rodent models, the combination of ketamine and xylazine. The essential role of ketamine, as an antagonist of NMDA receptors, plays a crucial part in the generation of slow oscillations

through partial inhibition of glutamatergic neurotransmission (157, 158). It is noteworthy that ketamine also shows inhibitory effects on nicotinic acetylcholine receptors. However, this is not thought to be of significant importance in the genesis of slow oscillations due to the intrinsically low activity of the cholinergic system during natural slow-wave sleep (103, 159, 160).

Additionally, ketamine is unlikely to influence the generation of thalamocortical oscillations through the GABAergic system; at the anesthetic dose, it only has a potentiating effect on α6β2δ and α6β3δ receptors, which are found exclusively in the granular layer of the cerebellum in mammals (161, 162). Furthermore, xylazine, which is typically co-administered with ketamine, may also impact the modulation of slow oscillations, both in terms of duration and amplitude of up- and down-states. It acts in the neocortex as an agonist of α2-adrenergic receptors, which enhance cortical activity by closing H-channels (12, 163-165).

1.4 Slow oscillation as traveling wave

It is now evident that the elements of local and global neural networks communicate with each other through complex interactions. Attempting to visualize the spontaneous or induced activity of different populations of neurons will likely result in the formation of distinct wave-like patterns with varying starting points. Just think of the visualization of EEG measurements or fMRI recordings. Virtually all brain rhythms can be described as propagating waves (166-168). Neuronal oscillations play a fundamental role in the transmission of information, communication, and interaction between populations of neurons (169-171).

Slow oscillation is defined as the spontaneous cortical-wide event of NREM sleep during which neurons switch between active and silent phases in a fraction of a second. During slow-wave activity propagation, populations of neurons in close proximity slightly depolarize their postsynaptic partners to maintain wave propagation. This mild depolarization (5 to 10 mV) in the area creates a higher probability of spiking, making the area more sensitive to inputs compared to areas where no wave propagation has occurred.

Recent advances in electrophysiological recording methods that provide high spatial resolution concurrently with large cortical coverage have led to the recent discovery of the propagating nature and complex spatiotemporal dynamics of slow-waves. Before introducing modern multichannel recording methods, scientists established a connection between the functioning of brain oscillations and zero-delay synchronization. Zero-delay synchronization is coordinating oscillations from different sources without any temporal delays. The coordination of motor behaviors relies on this underlying mechanism (172, 173). After successfully overcoming the technological barrier, it became feasible to identify subtle and delayed synchronizations.

However, with further advances in spatial and temporal resolution shifted the focus toward understanding the various traveling wave patterns formed by phase shifts. The advent of high-resolution devices also helped to subdivide traveling waves. Traveling waves can be arranged on a spatial and temporal scale. Traditionally, macroscopic waves, which can cover the whole or specific cortical regions, can be investigated with a low spatial resolution (centimeters) and high temporal resolution (milliseconds) using techniques such as EEG (electroencephalography), ECOG (electrocorticography) and magnetoencephalography (MEG). The appearance of new techniques using multielectrodes or working with different voltage-sensitive dyes with high spatial and temporal resolution has made the investigation of mesoscopic waves possible (174, 175). By examining their velocity, it can be concluded that macroscopic waves have a similar velocity to the axonal conduction of myelinated axonal fibers. In contrast, the velocity of mesoscopic propagation waves is close to the axonal conduction velocity of unmyelinated horizontal fibers in the cortex (176, 177).

The traveling of cortical SWs has been observed in humans as well as in various animal species using high-density EEG (7, 178, 179), electrocorticography (ECoG) (180-182), and multielectrode array recordings (135, 136, 139, 183, 184). Moreover, cortical SW propagation has also been detected in optical signals obtained with mesoscopic optical imaging methods, such as calcium imaging or voltage-sensitive dye imaging (184-199). Individual slow-waves are typically initiated in an anterior cortical region in humans. However, they can originate from any point of the cortex and then typically travel in the

posterior direction (7). At a more detailed spatial scale, however, SWs can be distinguished by more complex propagation patterns (181). In rodents, during anesthesia or quiet wakefulness, spontaneous cortical slow-waves predominantly propagate along the anterior-posterior axis, similarly to what was observed in humans, moving from anterior cortical areas towards posterior regions (anterior-to-posterior or front-to-back propagation), or from posterior parts of the cortex to anterior areas (posterior-to-anterior or back-to-front propagation; (180, 184, 186, 188, 197, 200-204). Furthermore, several studies have described unique and recurring spatiotemporal patterns of cortical activity, referred to as 'motifs', where the neuronal activity starts in specific cortical areas and then travels along well-defined trajectories (185, 189, 190). The majority of related research has focused on investigating the propagation patterns of SWs within the neocortex, while the spatiotemporal activity patterns generated in the thalamus, the other brain structure contributing to the generation of slow-waves, have received little attention so far (204-207).

1.5 High-density neural probes in the study of spatiotemporal activity patterns in neural networks

In the evolution of modern neurophysiology, both invasive and non-invasive techniques play a major role. The use of various extracellular electrodes *in vitro* and *in vivo* experimental settings to record single-unit (SU) and multi-unit activities (MUA) has significantly contributed to the advancements in neuroscience since their introduction nearly 70 years ago. The first such measuring device was made from a single tungsten microwire (208). Shortly thereafter, devices consisting of multiple wires twisted together from various conductive materials and equipped with insulation appeared. With the advent of stereotrodes and tetrodes, there was a significant increase in the number of simultaneously recorded and distinguishable single-unit activities (209, 210).

The technological progress in the microelectronics industry has enabled the development of silicon-based MEAs (Multielectrode Arrays) that cover the diverse needs of neuroscientists. One of the most significant advancements in MEA technology can be attributed to Wise and his colleagues, who created the Michigan arrays. The Michigan-type electrodes are characterized by their planar arrangement and are now available in a wide variety of configurations on the market (211). Another popular type of MEA, often used for neocortical recordings, is the "Utah intracortical electrode array" developed at the University of Utah (212). In this design, the electrodes are arranged in a 10 x 10 grid, each with a 1.5 mm long shank at the end (213-216). Over the past decade, the amount of single-cell activity extracted from raw data has increased, aiding neuroscientists in understanding complex network effects and brain structures. In 2010, Ian H. Stevenson and colleagues concluded that the number of simultaneously conducting neurons doubles approximately every seven years. After 1957, it took approximately 20 years for the number of simultaneously recorded neurons to reach a dozen (217). Currently, the state of the art allows for recording up to several thousand cells (218). The advent of Neuropixels 1.0, which we utilize, represents a significant advancement, with a single 10 mm, 70×20-µm cross-sectional shank of this probe containing 960 sites (12×12-µm) arranged in 4 rows and a checkerboard pattern. Of these 960 sites, we can simultaneously record on 384 channels of our choice (13). In the case of the cortical dataset

article, we used a 128-channel custom-designed silicon probe developed as part of the NeuroSeeker project (www.neuroseeker.eu). This custom probe has an 8 mm long shank, a cross-section of 100 μm × 50 μm (width (W) × thickness (T)), and a chisel-shaped tip. The square-shaped recording sites, located on the shank, have a side length of 20 μm (site area, 400 μm^2) and a spacing between the edges of the sites of 2.5 μm (corresponding to a center-to-center site distance of 22.5 μm) (219).

1.6 Advantages and challenges of high-density recording arrays

Alongside the incredible development of supporting hardware offering ever-greater spatial and temporal resolution, the detection of single-cell activities presents software challenges for researchers. The introduction of high-density probes has led to a significant increase in the number of neurons that can be simultaneously monitored in recent decades. This remarkable growth has obligated the development of sophisticated algorithms and data processing pipelines to handle this tremendous amount of generated data. This has also pushed for the development of analytical methods with which to study complex interactions in networks of neurons with many participants, thus demanding high computing power. The advent of the Neuropixels 1.0 probe (IMEC, Leuven, Belgium) has enabled monitoring of the activity of large numbers of neurons in many species, including subcortical structures, for extended periods through the use of dense arrays of recording sites produced using CMOS fabrication techniques (13). The Neuropixels version 2.0 (IMEC, Leuven, Belgium) is no longer limited to high-density recording along a plane; with its four shanks, a four-stem version can now perform dense sampling in a ~1 mm x 10 mm plane with 5120 recording sites (220). Significant progress has been made in enhancing the performance of neural interfaces *in vivo* to enable their sustained, prolonged operation in aggressive tissue environments over the past few years. This includes many optimizations for factors like chemical and mechanical stability and biocompatibility. This can be optimized to help with the development of long-term neural recordings(35).

1.7 Standardized neuro-data sharing

In the context of scientific progress, the sharing of experimental data is becoming increasingly important. Neuroscience is just beginning to develop this aspect of its practice, compared to other scientific fields where the collection and use of data in a uniform format for various meta-analyses is already a common practice (219, 221). Experiments in the field of neurophysiology address a wide range of questions, and these questions are investigated with a variety of tools. The resulting data can also be highly diverse and often lack accessibility. It is evident that data sharing does not yet occur in a format that is widely accepted and accompanied by basic metadata that can be reused by others. A further significant role is played by various data repositories, which provide storage and a searchable interface for researchers to freely share data related to neuroscience (https://dandiarchive.org, https://gin.g-node.org/UlbertLab/High_Resolution_Cortical_Spikes), as well as data from other scientific fields (https://repo.researchdata.hu/) following the FAIR data principles.

According to Wilkinson et al. (2016) (222), the FAIR data principles demand that the produced data be simple to find, easy to access, integrable with other datasets, and accessible for all users to reuse. Collaborative data and metadata standards in other scientific fields have enabled unprecedented partnerships in neuroscience (223, 224). Nevertheless, the objective of standardization should not just be limited to enabling usage among the wider community but also to improving usability and repeatability within laboratories.

In all fields of study, including neurophysiology, it is challenging to analyze data without the required metadata describing various experiments' features. In this context, metadata is information that describes the details of animals used in the experiment, measuring equipment, measurement settings, or any other information that the researcher believes is helpful so that someone else will be able to reproduce the experiment. Researchers who want to reuse the data must spend more time and resources if metadata are not defined.

Developing data ecosystems describes a space where scientific data and related applications are shared, adopting a standardized "language" that enables efficient interchange and utilization of data by potential users for their specific needs (225). Consequently, the data

generated during scientific research could be reused beyond publishing by integrating it into a greater context where it may help address complex questions in neuroscience (222, 226).

The Neurodata Without Borders (NWB) data language was developed to structure and manage the diverse and dynamic neurophysiological data types (227). NWB utilizes the Hierarchical Data Modeling Framework (HDMF) (228) to provide a standardized format for storing multimodal data and its associated metadata. NWB files include measurements from particular studies and the essential metadata required for comprehensive data comprehension. The HDF5 format, which is utilized, hierarchically enables data organization, resembling a file system, all within a single file. It is compatible with all major operating systems and can be conveniently explored using the HDFView reader. This framework enables researchers to store both raw and processed data, as well as descriptions of different measurement techniques. For instance, it permits recording spontaneous neuronal activity utilizing high-density neural probes during various stimulations in conjunction with the accompanying stimulus data. In essence, NWB facilitates incorporating various neurophysiological data and metadata into a standardized format that may be adapted to meet the evolving requirements of the scientific community. The data described in this thesis, as well as additional data sets from our research group, have been released in NWB format and are freely available on the HUN-REN Data Repository Platform (HUN-REN ARP,https://repo.researchdata.hu/dataverse/ulbertlab).

2 Objectives

Recent findings suggest that the thalamus has a significant impact on a wide range of physiological functions that were formerly overlooked. There is a growing consensus that it plays a crucial role in generating and modulating slow-waves during the deepest phase of sleep, along with the supragranular layers of the cortex. The thalamocortical slow oscillation (< 1 Hz) can be separated into two phases: a period of low activity when the cells remain mostly inactive (down-state) and a period of high activity marked by significant cellular activity (up-state). In the literature, the complex spatiotemporal patterns of slow-waves have been predominantly studied in relation to the cortex.

The objective of my research was to provide answers to the following questions:

- Is it possible to detect Multi-Unit Activity propagating patterns in the thalamus of anesthetized rodent species, similar to the patterns found in the cortex?
- What are the predominant relationships between the different thalamic propagation patterns, and what are their proportions of occurrence?
- Is there a temporal relationship between cortical and thalamic up-state propagation patterns?
- Does thalamic multi-unit activity propagation also occur in naturally sleeping rats? Furthermore, if that is the case, how do its properties differ from what is recorded under anesthesia?

The second part of the thesis focuses on an openly available high-density cortical slow-wave dataset. As previously stated, this standardized dataset includes the necessary metadata to prepare it for future analyses. Accordingly, the high-density cortical data can aid in understanding slow-waves at a more detailed single-unit level.

Based on the above, I aimed to achieve the following:

- Provide a large electrophysiological dataset collected from the neocortex of twenty anesthetized rats with a 128-site silicon probe providing high spatial resolution.
- The continuous raw and wideband recordings, along with metadata, are packaged in the Neurodata Without Borders (NWB) format, a standardized data format for ease of use.

We also share the results of spike sorting, including the spike times, multichannel spike waveforms, and several spatiotemporal properties of single units, along with various sorting quality metrics that are also published to aid potential future users.

3 Methods

3.1 Animals

All experiments associated with the two studies discussed in the thesis adhered to the Council Directive 2010/63/EU dated 22 September 2010. Every procedure was reviewed and received approval from the Animal Care Committee of the Natural Science Research Center and the National Food Chain Safety Office (license numbers PE/EA/1261-7/2020, PEI/001/2290-11/2015). Acute thalamocortical recordings were collected from adult Wistar rats (n = 34; weight: 285.22 ± 81.21 g, mean ± SD; 19 females) and adult C57BL/6J mice (n = 9; weight: 26.33 ± 7.00 g; 4 females), and two adult rats (259 g, female; 476 g, male) were used for chronic measurements (Study 1(229)). Cortical measurements with high spatial resolution were conducted on Wistar rats (n = 20; weight, 315.5 ± 59.6 g; 11 females) for the dataset project. All experimental sessions were carried out during the subjective nighttime of the animals (Study 2 (14)).

3.2 Acute in vivo experiments in anesthetized animals

3.2.1 Animal surgery

The acute experiments were carried out similarly to those described in both the two central studies of the thesis and the previous works of our research group. Initially, I will briefly outline the steps consistent across the studies, and then I will discuss the differences in the investigative methods used in the two studies. In both studies, anesthesia was administered to rats and mice using ketamine (75 mg/kg of body weight) and xylazine (10 mg/kg of body weight), which were administered either intraperitoneally or intramuscularly to maintain the appropriate depth of anesthesia. Once the animals had reached the requisite depth of anesthesia for surgery, they were placed in a stereotaxic frame (David Kopf Instruments, Tujunga, CA, USA). The skin and connective tissues were then removed from the skull. A homeothermic heating pad (Supertech, Pécs, Hungary) maintained the animals' physiological body temperature. After preparing the surface of the skull, we used a dental drill to create a

3x3 mm diameter circular craniotomy at coordinates specified by experimental considerations on the left parietal bone of the skull. Following the completion of the craniotomy, the dura mater was incised over targeted cortical areas using a 34-gauge needle in order to avoid brain dimpling. Throughout the measurements, the brain is maintained in a moist state by regularly adding room temperature physiological saline solution into the cavity of craniotomy, protecting it from potential drying out. Different single or multi-shank silicon probes are attached to motorized stereotaxic micromanipulators (Robot Stereotaxic, Neurostar, Tübingen, Germany) and implanted into the brain at a slow speed. Our group has previously demonstrated that slow implantation (~2 μm/s) of silicon probes positively impacts the quality of neuronal recordings (230). An external reference electrode and grounding were provided by a stainless steel needle that was placed into the nuchal muscle of the animals Prior to insertion, the silicon shank(s) of the probes was coated with red-fluorescent dye 1,1-dioctadecyl-3,3,3,3-tetramethylindocarbocyanine perchlorate (DiI, D-282, ~10% in ethanol, Thermo Fisher Scientific, Waltham, MA, USA) in order to enable post-mortem histological verification of the recording locations. Upon completion of the experiment, the silicon probes were removed and immersed in a 1% Tergazyme solution (Sigma-Aldrich, St. Louis, MO, USA) for a minimum of 30 minutes, followed by a thorough rinse with distilled water.

It is essential to highlight that the locations of measurements in the two studies significantly differed. Thalamic insertions followed the anatomical positioning relative to the bregma in both rats (~ -1.5 mm to -6 mm along the anterior-posterior axis (AP), 0.4 mm to 4 mm along the medial-lateral (ML) axis) and mice (~ -1 mm to -3 mm AP, 0.6 mm to 2.7 mm ML) as described by Paxinos and Franklin (2004) and Paxinos and Watson (2007)(231, 232). To examine multiple thalamic locations within a single animal, we performed consecutive insertions (2-4) using either the same or a different (unused) silicon probe of identical type. We maintained a minimum distance of 500 μm between these insertions to prevent recording near thalamic tissue that may have been compromised by earlier penetrations.

The neural activity collected for the high spatial density database was derived from multiple layers of the cortex. Measurements were spaced 500 μm apart to avoid overlap with previous

insertions. Each animal underwent an average of two probe insertions. While the ventral thickness of the cortical areas studied ranged from 1.3 to 1.8 mm (mean ± standard deviation [SD]; 1.51 ± 0.13 mm; measured post-mortem at the probe tracks after histological processing), we usually recorded from two or three depths from the same insertions that partially overlapped (from 20 to 100 μm; Fig. 20) because the vertical tissue coverage of the probe is approximately 700 micrometers.

3.3 Electrophysiological recordings of spontaneous thalamic activity in anesthetized rodents.

Spontaneous thalamic activity in anesthetized rodents was recorded using two types of silicon-based probes. The aim was to determine whether the spreading activity in the thalamus can be detected at different spatial scales. To observe the spontaneous activity of the different nuclei of the thalamus with a more extensive spatial coverage, we used a multi-shank probes (A8x8-10mm-200-200-177 probes with 64 recording sites for rats and A8x16-Edge-5mm-100-200-177 probes with 128 recording sites for mice; NeuroNexus Technologies, Ann Arbor, Michigan, USA). These probes have eight silicon shanks with a 200 μm inter-shank spacing and multiple equally distributed electrode recording sites on each shank (8 sites/shank with 200 μm inter-electrode distance for rats; 16 sites/shank with 100 μm inter-electrode distance for mice). In rodents, the dorsoventral extent of the thalamus is approximately 3-3.5 mm in rats and 1.5-2 mm in mice. Due to the limited dorsoventral coverage of the probes employed (1.5 mm), multiple overlapping consecutive measurements were conducted from the dorsal direction to the ventral direction in 500-700 μm steps following each recording. An Intan RHD-2000 electrophysiological recording system (Intan Technologies, Los Angeles, CA, USA) was used to record wideband thalamic activity (0.1 – 7500 Hz) at a sampling frequency of 20 kHz/channel and a resolution of 16 bits. A 64-channel Intan amplifier board was employed for rat recordings, while a 128-channel amplifier board was utilized for mouse recordings. A total of 82 spontaneous recordings were obtained from 14 rats using multi-shank silicon probes, with each recording lasting approximately 30 minutes on average, while 18 spontaneous recordings were collected from 5 mice (see Tables 1 and 2 for more details). The orientation of the probe shanks was parallel to the medial-lateral axis in 10 out of 14 rats and along the anterior-posterior axis in the remaining four animals. The recording system, connected to a laptop via USB 2.0, saved the continuous thalamic recordings to a network-attached storage device for subsequent analysis.

To study thalamic activity with finer spatial resolution, we used high-density Neuropixels 1.0 probes (IMEC, Leuven, Belgium), which feature 960 recording sites (electrodes) on a single shank, of which 384 can be selected for simultaneous recording. Data was acquired

using the Neuropixels recording system and a PXIe-1071 chassis with an MXI-Express interface (National Instruments, Austin, Texas, USA). Spiking activity from the thalamus was recorded at a sampling rate of 30 kHz/channel and with a resolution of 10 bits (amplifier gain: 500; high-pass filter cutoff frequency: 300 Hz), using the SpikeGLX software package (https://billkarsh.github.io/SpikeGLX/). At a sampling rate of 2.5 kHz/channel (amplifier gain: 250), local field potentials were also recorded in distinct files. Two to four hours of neuronal data from two to three thalamic insertions were usually obtained from a single animal. The data was acquired using recording sites that were closest to the probe tip (bank 0). A total of 46 spontaneous recordings were obtained from 20 rats, with 5 recordings excluded from analysis due to low signal quality or irregular slow-wave activity. Additionally, 11 recordings were made from 4 mice (see Tables 1 and 2 for further details). The duration of each recording was approximately one hour.

Table 1. Summary statistics of recordings obtained in anesthetized rats.

Rat	Multi-shank recordings	Neuropixels recordings
No. of animals	14	20
No. of penetrations	40	46
Average number of penetrations per animal	2.86 ± 0.86	2.30 ± 1.13
No. of recordings	82	46
Average number of recordings per animal	5.86 ± 2.03	2.30 ± 1.13
Average duration of recordings (min)	29.93 ± 6.50	56.44 ± 17.54

Table 2. Summary statistics of recordings obtained in anesthetized mice.

Mouse	Multi-shank recordings	Neuropixels recordings
No. of animals	5	4
No. of penetrations	10	11
Average number of penetrations per animal	2.00 ± 1.00	2.75 ± 0.96
No. of recordings	18	11
Average number of recordings per animal	3.60 ± 1.67	2.75 ± 0.96
Average duration of recordings (min)	57.94 ± 11.75	57.99 ± 4.41

3.4 Simultaneous electrophysiological recordings from the thalamus and neocortex

In order to gain a more detailed understanding of the relationship between thalamic and neocortical activity during sleep, we conducted simultaneous spontaneous population activity recordings with two types of probes in a subset of our rat experiments (n = 5 animals). The Neuropixels probe was positioned at a dorsoventral depth of 7 - 7.5 mm (target coordinates, AP: -3 mm; ML: +2 mm) into the thalamic area, targeting both first-order somatosensory nuclei such as the ventral posteromedial nucleus (VPM) and higher-order nuclei including the posterior nucleus (Po) and the laterodorsal nucleus (LD). For simultaneous recordings, we implanted a NeuroNexus Buzsaki64 into the neocortex at a depth of 1.1 mm to capture the spontaneous activity of layer 5. This particular multi-shank probe features eight shanks with an inter-shank distance of 200 μm, with eight tightly grouped sites at the tip of each shank, arranged in a V-shape. The probe was implanted at a lateral inclination of 15° from the vertical (relative to the sagittal plane), so that the shanks were perpendicular to cortical layers. The shanks of the probe were aligned along the anterior-posterior axis (providing a

cortical coverage of ~1.5 mm along the AP axis), with the first shank located in the most anterior position. The majority of the probe shanks were situated within the somatosensory cortex. However, some of the posterior shanks may have recorded the activity of the parietal association cortex (approximate position of the first shank, AP: -1.5 mm; ML: +4 mm from the bregma). The two recording systems (Intan-based and Neuropixels systems) recorded brain electrical activity simultaneously at a 30 kHz sampling rate (all other recording parameters remained the same as previously mentioned). The two recording systems were synchronized by initiating cortical and thalamic recordings concurrently with TTL (transistor-transistor logic) pulses generated by a PulsePal device (233).

3.5 Chronic in vivo experiments in freely moving, naturally sleeping rats

3.5.1 Animal surgery

The *in vivo* chronic probe implantations were performed using the same equipment for the acute experiments, including the stereotaxic frame and heating pad. The surgical procedure was conducted following the methodology outlined in van Daal et al. (234). Surgical instruments were sterilized prior to the implantation process. Before implanting the probe, a reusable 3D-printed single-probe fixture from ATLAS Neuroengineering in Leuven, Belgium, consisting of three main components, was prepared (234). The main body of the fixture accommodates a single-shank Neuropixels 1.0 silicon probe with an attached headstage, featuring a skull connector for secure attachment to the skull and a protective cover to safeguard the electronic components from damage. Once the 3D-printed fixture had been assembled, the silicon shank of the Neuropixels probe was coated with fluorescent DiI to verify the recording site in the thalamus post-mortem. Adult Wistar rats (n = 2) were anesthetized using ketamine/xylazine following the same procedure as outlined previously for the acute surgery. After the animal reached the surgical level of anesthesia, 0.1 ml meloxicam (Dopharma Research, Raamsdonksveer, Netherlands) was administered subcutaneously (1 mg/kg), then the rat was placed in the stereotaxic frame. During the surgical procedure, the animal's physiological body temperature was maintained using a homeothermic heating pad, and ophthalmic gel (Corneregel, Dr. Gerhard Mann Chem.-Pharm. Fabrik, Berlin, Germany) was applied to keep the eyes moist. After trimming the hair

from the head of the animal, the surface of the scalp was disinfected with Betadine (Mundipharma, Cambridge, England) and 70% alcohol. Subsequently, the skin was gently retracted from the top of the skull using four pean forceps after a small incision was made in the skin along the midline, between the eye line and the lambda, to gain access to the skull. After that, the connective tissue was removed from the skull, and then a small portion of dental etching gel (Etch-Rite, PULPDENT Corporation, Watertown, MA, USA) containing 38% phosphoric acid was applied to the cleaned area to roughen the skull surface for better adhesion of the dental cement used to secure the 3D-printed fixture. To further stabilize the fixture, four bone screws (0.9 mm in diameter and 2 mm in length; ATLAS Neuroengineering, Leuven, Belgium) were mounted in the skull over the right hemisphere, and a fifth bone screw (0.9 mm in diameter and 3 mm in length) with a wire soldered to it, serving as the reference and ground electrode for recordings, was positioned above the cerebellum. Using a dental drill, a 2 mm × 2 mm rectangular craniotomy was created over the thalamic area of interest (posterior and lateral posterior thalamic nuclei; AP: –3.6 mm, ML: 2.5 mm, relative to the bregma). In order to minimize brain dimpling during probe insertion, the dura mater was cautiously punctured above the insertion site using a sterile 34-gauge needle. Sterile physiological saline solution at room temperature was regularly dripped into the cranial cavity to keep the neocortex hydrated until the probe was implanted. The Neuropixels probe was positioned over the insertion site, attached to the 3D-printed fixture, and mounted on a motorized stereotaxic micromanipulator. A hermetic seal was created at the base of the probe shank to protect the probe from dental cement by applying a mixture of bone wax and paraffin oil. Then, to minimize insertion-related mechanical tissue damage, the probe was inserted into the brain tissue at a depth of 7 mm from the cortical surface at a slow insertion speed of 2 μm/s. After implanting the probe, the exposed cortex was sealed with a soft, two-component silicone gel (DuraGel, Cambridge NeuroTech, Cambridge, United Kingdom) to minimize the risk of inflammation and prevent cerebrospinal fluid leakage. Next, the skull connector was secured to both the surface of the skull and the bone screws with light-curing dental cement (RelyX Universal Resin Cement, 3M, St. Paul, MN, USA). Following that, the reference electrode was attached to the pin extending from the skull connector, and then the animal's skin was sutured around the fixture using 2-3 stitches.

Finally, while still lightly anesthetized, a brief (~10 min) recording was made to check the signal quality and record thalamic activity in the anesthetized state. Subsequently, the rat was moved to the animal facility for a five-day recovery period, during which it was administered antibiotics (Augmentin, Glaxo Wellcome Production, Mayenne, France; 20 mg/kg body weight) and analgesics (Panadol Baby, Farmaclair, Hérouville-Saint-Clair, France; 2 mg/ml).

3.6 Chronic electrophysiological recording sessions

The animal was transported from the animal facility to a soundproof, dark Faraday cage for the recording sessions and then connected to the Neuropixels recording system. We began recording when there was a significant reduction in movement artifacts on the continuously monitored thalamic signals, suggesting that the animal was likely beginning its first sleep cycle. Starting on the fifth day following the implantation of the probe, we monitored thalamic activity every day for roughly two weeks. The recording sessions ranged from 0.5 to 3 hours, but each session typically lasted for several sleep-wake cycles. The data acquisition parameters were identical to those mentioned previously for the acute Neuropixels experiments.

3.7 Thalamic data analysis

3.7.1 Detection of up-state onsets and computation of the up-state onset locked multiunit activity average

To accurately determine the onset times of thalamic or cortical up-states during slow oscillations in anesthetized animals, we used a modified version of a multiunit activity (MUA)-based method previously outlined in previous studies (235, 236). This technique is suitable for analyzing data recorded from anesthetized animals using either single-shank (Neuropixels) or multi-shank probes. Initially, we eliminated low-frequency components such as local field potentials from wideband recordings made with multi-shank probes, using a third-order Butterworth bandpass filter with a range of 500 – 5000 Hz and zero-phase shift. After filtering, the signal was rectified to produce the MUA signal. Subsequently, we downsampled the MUA by a factor of ten to accelerate processing (e.g., from 20 kHz to 2 kHz for multi-shank recordings). Following, a single-channel time series representing the

instantaneous intensity of population activity in the thalamus (or cortex) was created by summing up the samples of the downsampled MUA across all channels. In the case of Neuropixels recordings, we first excluded all channels not located within the thalamus, such as hippocampal channels, before aggregating the samples. To obtain the smoothed population activity (SPA), the summed signal was smoothed using a third-order Butterworth filter, 50 Hz, zero-phase shift. The amplitude histogram of the SPA showed a distinct bimodal distribution in most cases.

To determine the onset of up- and down-states, first we calculated an amplitude threshold level. This was achieved by determining the average (AVG) and standard deviation (SD) of the thalamic or cortical activity during down-states (periods without action potential firing) using the SPA signal. We identified the center of the down-states and then calculated the average amplitude over a 50 ms window centered on this point. Empirical data indicated that setting a threshold at AVG + (2.5 * SD) was generally acceptable for precisely identifying the onset of up- and down-states. Within the state detection algorithm, up-states were required to have a minimum duration of 50 ms, while down-states were set to have a minimum duration of 100 ms. For recordings where the precision of onset detection was lacking, adjustments were made to the minimum duration of the states and the value of the standard deviation multiplier. The onset of an up-state was defined as the time point when the amplitude value of the SPA signal exceeded the calculated threshold level. This time point had to be preceded by a down-state with a duration equal to or longer than the defined minimum state duration. The extracted up-state onset times were collected into files. Lastly, we only retained up-states with a duration of AVG ± (1.5 * SD) in order to minimize the impact of outliers (i.e., very short or very long up-states that are frequently the result of incorrect or inaccurate state detections) on the up-state onset locked thalamic/cortical MUA averages. These MUA averages, also known as MUA depth profiles for thalamic recordings, were calculated by averaging short segments of the continuous MUA recordings around the up-state onset (300 ms after the onset and 100/150 ms before), which were filtered between 500 and 5000 Hz and rectified. Finally, the MUA average was smoothed using a third-order Butterworth filter (50 Hz, low-pass, zero-phase shift), then z-score normalization was applied to the smoothed MUA average.

3.7.2 Identifying preferred propagation patterns during thalamic up-states in neuropixels recordings

To identify the preferred directions of MUA propagation observed in our thalamic recordings (e.g., dorsal-to-ventral or ventral-to-dorsal), we selected Neuropixels recordings where the propagations were clearly visible (evident also in the up-state onset locked MUA depth profiles; n = 15 recordings from 14 rats), and it was approximately possible to choose the channel numbers associated with the start and termination of propagation along the thalamus's dorsoventral axis.

Afterward, we chose ten adjacent channels with at least moderate MUA levels at three thalamic positions: the previously mentioned ventral and dorsal propagation borders and midway between the two. Using the aforementioned state detection algorithm, we then identified the onset times of up-states at these three positions. Only up-states detected at all three locations within a short time frame were kept for further analysis (i.e., within a time window of ±200 ms with respect to up-state onsets detected at the ventral thalamic location used as reference). Delays of up-state onsets between the three thalamic locations were calculated, and then the sequence of MUA initiation (propagation pattern) was determined for each up-state. Finally, the rate of occurrence and the proportion of all six possible propagation patterns were calculated.

3.7.3 Correlation between cortical and thalamic propagation patterns during up-states

To identify the temporal relationship between cortical and thalamic slow-waves, we calculated MUA averages in both cortical and thalamic areas using the onset of cortical up-states (detected based on the summed population activity of all cortical channels) in the simultaneous recordings (n = 5 recordings from 5 rats), as previously described. Furthermore, we identified up-state onsets at three cortical and three thalamic positions to examine the relationship between cortical and thalamic propagation patterns. For the cortex, these positions were the following: between shanks 1 and 2 (by detecting up-state onsets on both

shanks and calculating their average; anterior position), between shanks 4 and 5 (middle position) and between shanks 7 and 8 (posterior position). The direction of cortical activity propagation during up-states (e.g., anterior-to-posterior or posterior-to-anterior) was identified based on the up-state onset delays between cortical positions. The exact process outlined above was used to determine thalamic propagation patterns. Lastly, the frequency of occurrence and the percentage of each of the six potential propagation patterns were determined for both the cortex and the thalamus.

3.7.4 Scoring sleep stages in chronic recordings

To determine the different phases of slow-wave sleep and any potentially emerging propagating activities in chronically implanted animals, we created spectrograms using Chronux (v2.12) from local field potential recordings that were made in the frequency range between 0.1 and 100 Hz on a channel located in the hippocampus (Fig. 2). Afterward, we calculated the mean power in the delta (1 - 4 Hz) and theta (5.5 - 8 Hz) frequency bands, along with the theta/delta ratio (theta/delta ratio; Fig. 2).

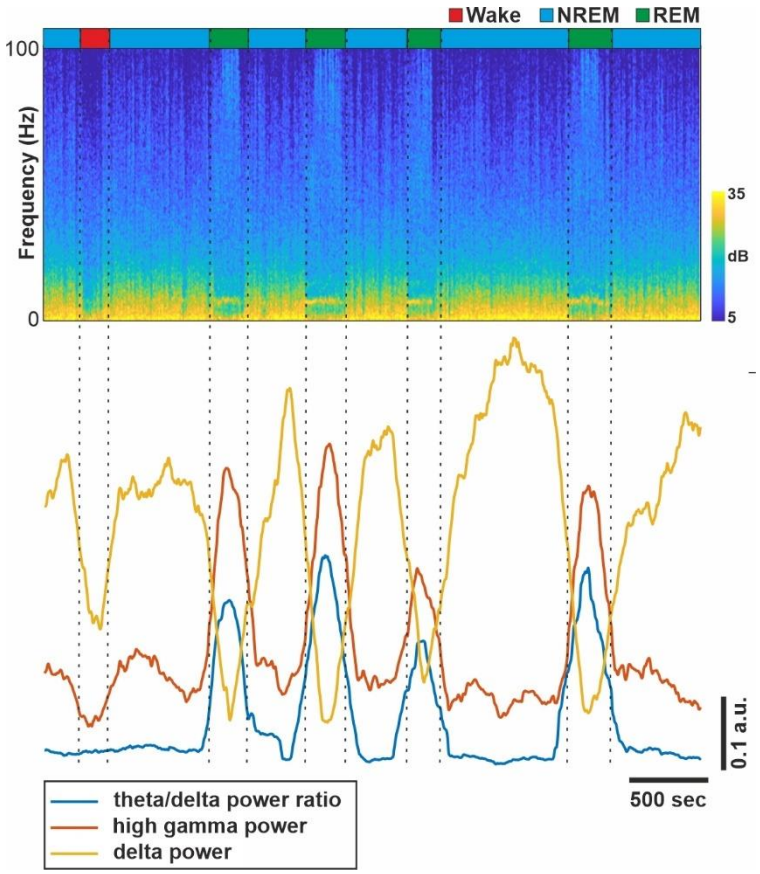

Figure 2. Example of sleep stage scoring in chronically implanted, naturally sleeping rats. *The time course of several spectral features (e.g., power in the delta frequency band) were calculated from the spectrogram (top) and used to determine the actual sleep stage (see the Methods section for details). Vertical dashed black lines indicate the transition between different sleep stages. NREM – non-rapid eye movement sleep, REM – rapid eye movement sleep.*

These spectral features enabled us to reliably differentiate NREM sleep, characterized by decreased theta and increased delta power (low theta/delta ratio), REM sleep and wake states, which were marked by increased theta power and decreased delta power (high theta/delta ratio; Fig. 2). Moreover, a distinction between REM and wake states could be achieved by examining the mean power of the high gamma band (70–100 Hz). Compared to wakefulness, REM sleep was distinguished by a markedly elevated level of high gamma activity (see Figure 2). Further evidence of wake states included movement artifacts and a weaker theta

rhythm. The visual inspection of thalamic activity during the identified NREM sleep periods was employed to detect and mark propagating MUA events. Each recording session typically examined a single NREM sleep period, which lasted at least five minutes (with an average duration of NREM periods of 12.04 ± 4.66 minutes). In total, 21 recording sessions for two chronically implanted rats (13 and 8 sessions, respectively) were analyzed, and we calculated the rate of occurrence of identified propagating MUA events and computed averages of MUA depth profiles locked to the onset of these events.

3.7.5 Identification of thalamic nuclei

The identification of the thalamic nuclei from which population activity was recorded was achieved by verifying probe track positions, examining Nissl-stained brain sections, and analyzing neuronal activity in electrophysiological recordings. In certain instances, the localization of the sensory (relay) thalamic nuclei has been facilitated by using somatosensory, auditory, or visual stimulation. To delineate the thalamic nuclei in Nissl-stained sections with probe tracks, we initially identified vital anatomical landmarks, such as parts of the hippocampus and internal capsule. This was followed by comparing these sections to the rat/mouse brain stereotaxic atlas (231, 232) the results were refined using knowledge from spontaneous and stimulation-evoked neuronal recordings. When a significant discrepancy was found between the original implantation coordinates and the actual anatomical position of the probe, evidenced by differences greater than 200 µm in AP, ML, or DV coordinates based on anatomical and electrophysiological data, we updated the implantation coordinates to enhance the accuracy of the colormaps that summarize the locations of thalamic recordings in rats.

3.8 High-density electrophysiological recordings.

In the second study, we used a high-density silicon probe to record spontaneous cortical activity(219). Numerous earlier investigations have utilized this probe type, consistently yielding high-quality recordings in diverse acute and chronic animal models (230, 237-242). The probe was developed within the NeuroSeeker project (www.neuroseeker.eu), and it features a single shank with 128 titanium nitride electrodes (see Fig. 19A). It was produced with a custom-made design at the Interuniversity Microelectronics Center (IMEC; Leuven, Belgium) and is not available commercially. The probe comprises an 8 mm long implantable shank with dimensions of 100 μm in width by 50 μm in thickness, which terminates in a chisel-shaped tip. The probe comprises square recording sites, each with dimensions of 20 μm (site area, 400 μm²) and separated by edges spaced 2.5 μm apart, resulting in a center-to-center distance of 22.5 μm between sites. The recording sites are configured into a tightly packed 32 × 4 array with uniform spacing (219). All microelectrodes have a low impedance of approximately 50 kΩ at 1 kHz, except for one electrode with a larger surface area that has a lower impedance of around 10 kΩ. Positioned in the upper right corner of the array, this electrode could potentially serve as an internal reference electrode. However, in our cortical recording sessions, we used it as a standard recording site (see Fig. 19A). The probe tip is located 300 μm from the bottom row of recording sites, and the dense array of microelectrodes spans 87.5 μm x 717.5 μm (horizontal × vertical) (219).

To record spontaneous cortical activity with 128 channels, we used two 32-channel and one 64-channel headstages. The recording device was an RHD-2000 electrophysiological recording system (Intan Technologies, Los Angeles, CA, USA). Wideband signals (0.1–7500 Hz) were acquired with 16-bit resolution and at a sampling rate of 20 kHz per channel. Approximately 30 minutes of multichannel neuronal data were gathered at each recording site, with an average duration of 37.55 ± 11.29 minutes and a range from 15.13 to 61.94 minutes. At the end of the experiment, the recordings (n=109) were saved onto a network storage device. The mapping of recording sites to channels is depicted in Figure 1a, with channel numbering beginning at the site positioned in the top left corner of the array. It should

be noted that the probe used for data collection had two shorted recording sites (sites 64 and 65; this occurred only in recordings from Rat04 to Rat20), and another site failed to function during one of the experiments (Rat20; channel 2). It is possible to interpolate data from these defective channels using the signals from nearby channels. However, in this instance, we chose not to interpolate or eliminate these channels. Additionally, during one penetration (Rat07; second insertion), no data was captured due to visible bleeding caused by the probe insertion, resulting in the absence of cortical spiking activity.

A previously reported approach (238) was employed to estimate the noise level in cortical recordings (see Fig. 21A). In brief, the down-states of the ketamine/xylazine-induced slow oscillation (see Fig. 19C for an example) were used to identify time periods when nearly all cortical neurons temporarily stop firing. The noise-contaminating levels of the recordings were estimated during these short periods of neuronal inactivity. Initially, the distinction between up-states (high spiking activity) and down-states (low spiking activity) was made by implementing a state detection algorithm (236, 238). Following the application of a Butterworth 3rd-order bandpass filter (300–6000 Hz; zero-phase shift) and rectified recording, we computed the root mean square (RMS) value for a 50 ms segment situated at the midpoint of down-states with a minimum duration of 200 ms. Subsequently, these RMS values were averaged across all channels within the cortex. The RMS of the neuronal activity was calculated using the same method as previously outlined for the RMS noise level to estimate the signal level in our recordings (Fig. 21B), except that measurements were made during up-states rather than down-states. To evaluate the contamination of the dataset by power line noise (refer to Fig. 19D), the power spectral density at 50 Hz was calculated for the first 10 minutes of each recording using SpikeInterface (243). The power spectral density values from 10 channels at various cortical depths were averaged. In addition to determining the absolute value of the 50 Hz noise (i.e., the power spectral density at 50 Hz; see Fig. 21C), we also assessed the relative increase in noise level by calculating the ratio of the power spectral density at 50 Hz to that at an uncontaminated nearby frequency (49 Hz; see Fig. 21D). All calculated noise and signal metrics are recorded in the "Recording_characteristics" Comma Separated Values (CSV) file included in the dataset.

3.9 Spike sorting

The Kilosort2 MATLAB package (244) was employed for spike sorting to isolate single-unit activity. The procedure was conducted with the default settings (defined in the StandardConfig.m file) alongside a channel map file created according to the design of the silicon probe used in this study. The only parameters modified were the sampling rate (ops.fs = 20,000), threshold (ops.Th = [8 3]), and minimum firing rate (ops.minfr_goodchannels = 0).

The next step involved analyzing the output from Kilosort, which essentially consists of a list of identified clusters that can appear as single units or multi-units. This list was reviewed using Phy (245), a Python library developed specifically for manual curation. Within Phy, we can remove artifactual templates and units considered as noise (e.g., units with atypical spike waveform shapes) or multi-unit activity (e.g., clusters with a contaminated refractory period). Additionally, Phy allows for cluster merging, splitting, and tagging through its GUI-based interactive visualization. Our goal was to retain only those clusters (marked as good units) in our dataset that exhibited a minimum of 100 spikes, a clear refractory period, a trough-to-peak amplitude greater than 30 μV of the mean spike waveform at the peak waveform channel (refer to the following section for definitions), and a regular waveform shape.

When dealing with bursting neurons or when changes in spike waveform caused by electrode drift resulted in multiple clusters forming from the same unit, two or more clusters were merged if they contained spikes from the same single unit. If two distinct clusters emerged on any of the two-dimensional scatterplots of principal components derived from the spike waveforms of a specific unit (FeatureView in Phy), the clusters were separated, and each newly formed cluster was assessed independently. Following manual curation, duplicate units were identified using their cross-correlograms with a custom MATLAB script. Potentially duplicated clusters were indicated by a significant peak on the cross-correlogram at about zero milliseconds after identifying the primary cluster. This was clearly

distinguishable because the negative peak of its spike waveform was centered at 0 ms. All duplicates of the primary cluster were removed. In the end, the dataset was cleared of single units not located in the neocortex (for example, hippocampal neurons collected at the deepest locations in some instances). It is also important to mention that duplicates arising from the overlap in recordings were not removed; thus, some identified neurons may appear twice.

3.10 Histology

In both studies, we used a previously described histological procedure to locate the traces of the silicon probes in the brain tissue and to identify the thalamic nuclei or the boundaries of the cortical layers (230, 236). Briefly, after collecting thalamic recordings, animals were deeply anaesthetized and transcardially perfused with physiological saline (100 ml), followed by a fixative solution containing 4% paraformaldehyde in 0.1M phosphate buffer (PB; pH = 7.4, 250 ml). Coronal brain slices of 60 μm thickness were then cut using a vibratome (Leica VT1200, Leica Microsystems, Wetzlar, Germany). Sagittal sections were prepared for rats in which the shanks of multi-shank probes were implanted along the anterior-posterior axis. Sections were rinsed in 0.1 M PB, mounted on gelatin slides, and air dried. To locate brain sections with fluorescent DiI marks indicating probe tracks, the slides were analyzed using a light microscope (Leica DM2500, Leica Microsystems) equipped with a fluorescent LED light source (SFL4000, Leica Microsystems) and a digital camera (DP73, Olympus, Tokyo, Japan). Brain sections were then stained with cresyl violet (Nissl), dehydrated in xylene, and coverslipped with DePex (SERVA Electrophoresis, Heidelberg, Germany). Finally, the Nissl-stained sections containing the silicon probe traces were photographed under a microscope.

4 Results

4.1 Propagation of neuronal population activity is common during spontaneous up-states in dorsal thalamic nuclei of rats under anesthesia

Apparent propagation of multiunit activity (MUA, 500 – 5000 Hz) during up-states was observed in our study involving 14 rats across various thalamic nuclei (Figs. 3 and 6) during 40 implantations. In these experiments, using an 8-shank, 64-electrode silicon probe, a visible delay (> 10 ms) in the onset of up-states was noted on at least three adjacent channels/electrodes (the distance between adjacent electrodes and shanks of multi-shank probes was 200 µm), and this delay gradually increased as a function of distance from the channel where the spiking activity initiated (i.e., the channel with the earliest up-state onset).

In the case of propagating up-states, we observed that the delay between the initiation at the starting channel and the channel showing the most prolonged delay could be as long as several hundred milliseconds, averaging around 100 ms (Fig. 3D and E; Figure 4. and Figure 5.). Regarding spatial propagation, we noted that it could extend several hundred micrometers in various directions (Fig. 15A and B; Figure 4. and Figure 5.). Spatial propagation was typically recorded simultaneously across multiple electrodes (3-8) and several probe shanks (2-5).

The appearance of propagating thalamic population activity depends on its anatomical position. Our findings are based on the computed up-state onset locked MUA depth profile averages and histological results (e.g., Fig. 15C). In the dorsal thalamus, particularly in higher-order nuclei such as the posterior (Po), lateral posterior (LP), or laterodorsal (LD) nucleus (Fig. 14), thalamic activity propagation was observed. In contrast, in ventral thalamic structures, it was less common. Except for the propagation of sleep spindles (see further details below), such as in the ventral posteromedial nucleus (VPM; Fig. 15A) or the ventral division of the medial geniculate nucleus (MGV; Fig. 15B), this phenomenon was virtually absent. In these nuclei, up-states are typically initiated on adjacent channels almost synchronously (Fig. 15A and B).

In thalamic areas, up-state propagation was noted to consistently follow a dominant, highly stereotypical pattern. This was particularly evident from the distinct propagation observed along the dorsoventral axis (generally from ventral to dorsal; n = 41/82 recordings; ~50%), as shown in the MUA depth profiles locked to up-state onsets, which demonstrated minimal variability (Fig. 15) across the recordings (n = 43/82 recordings in 14 rats; ~52%). Additionally, alternative propagation patterns were detected such as dorsal-to-ventral propagation, but they were less frequent than the dominant stereotypical patterns. We looked at the propagation of activity along the anterior-posterior or medial-lateral axis (across probe shanks). Even though we have seen posterior-to-anterior propagation (n = 5/27 recordings in 2 out of 4 rats; ~19%; Figure 4) and medial-to-lateral propagation (n = 5/55 recordings in 4 out of 10 rats, ~9%; Figure 5.) of thalamic MUA activity, these patterns of propagation were less frequent compared to activity propagation along the dorsoventral axis (~50% vs. ~9%/~19% of recordings, respectively). The propagation patterns from posterior to anterior and medial to lateral were less reliable and uniform and often had shorter delays, typically less than 100 milliseconds. Therefore, for the remainder of the study, our main focus was characterizing the thalamic up-states that spread throughout the dorsoventral.

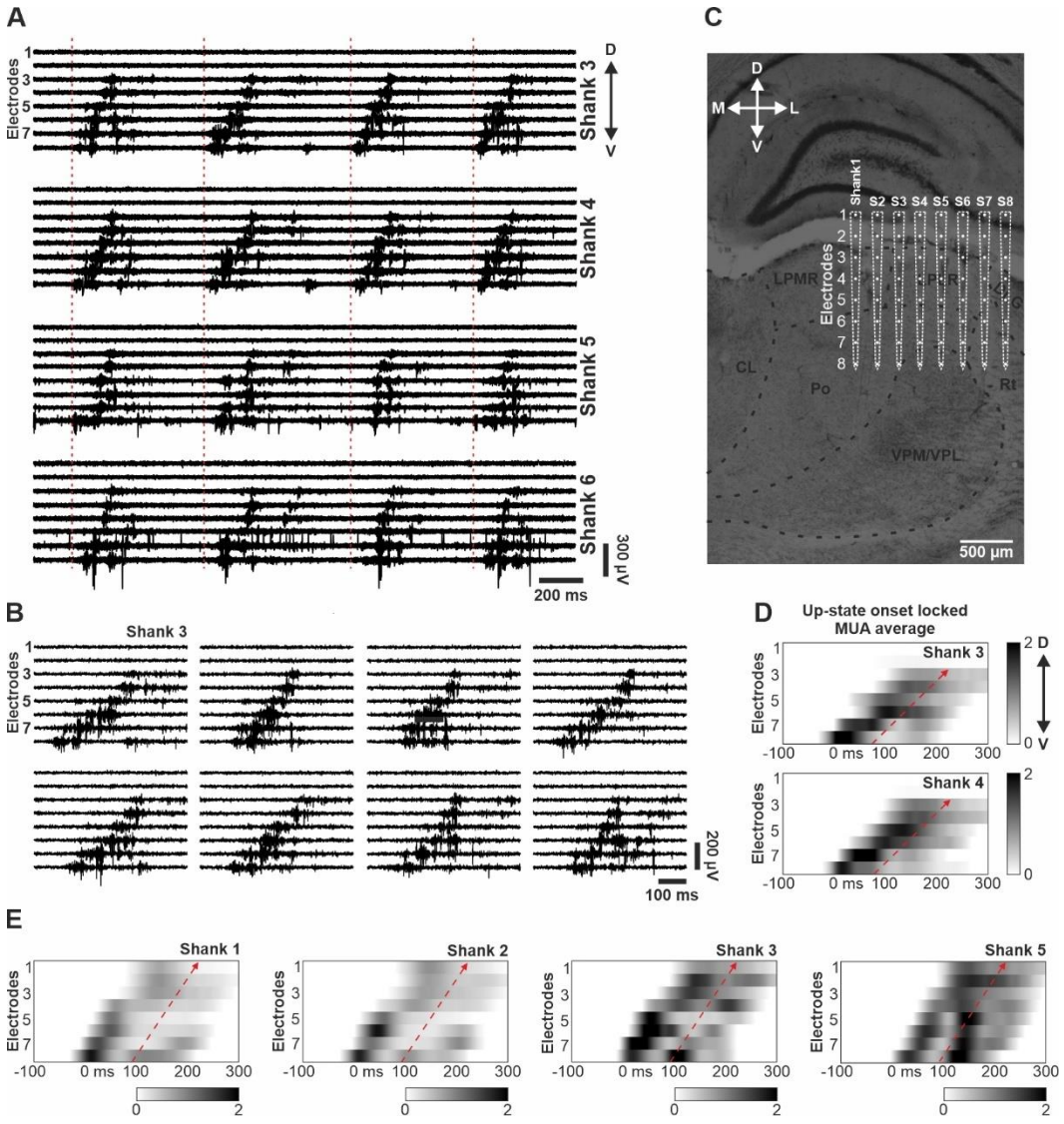

Figure 3. Propagating thalamic population activity observed with multi-shank silicon probes under ketamine/xylazine anesthesia in rats. *(A) Representative spontaneous thalamic multiunit activity (MUA) traces recorded on four adjacent shanks in the posterior (Po) and lateral posterior (LP) thalamic nuclei. Up-state onsets are indicated by vertical dashed red lines. Activity propagation from ventral (bottom electrodes) to dorsal (top electrodes) regions of the thalamus is visible on shanks 3 and 4. (B) Examples of individual thalamic up-states exhibiting propagating MUA recorded on shank 3 at various time points of the 30-minute-long recording. (C) Nissl-stained coronal brain section illustrating the approximate location of the shanks and recording sites (electrodes) of the silicon probe*

relative to major thalamic nuclei. Shanks 3 and 4 recorded mainly from two higher-order nuclei (Po and LP). (D) Normalized (z-score) MUA depth profile averages locked to the up-state onsets (n = 2452 up-states) on shanks 3 (top) and 4 (bottom) showing ventral-to-dorsal propagation of thalamic activity (dashed red arrow). The up-state starts at time point zero. (E) Normalized (z-score) up-state onset (n = 2857 up-states) locked MUA depth profile averages on four shanks located in the dorsal thalamus (Po and LP) of another rat. D – dorsal; V – ventral; M – medial; L – lateral.

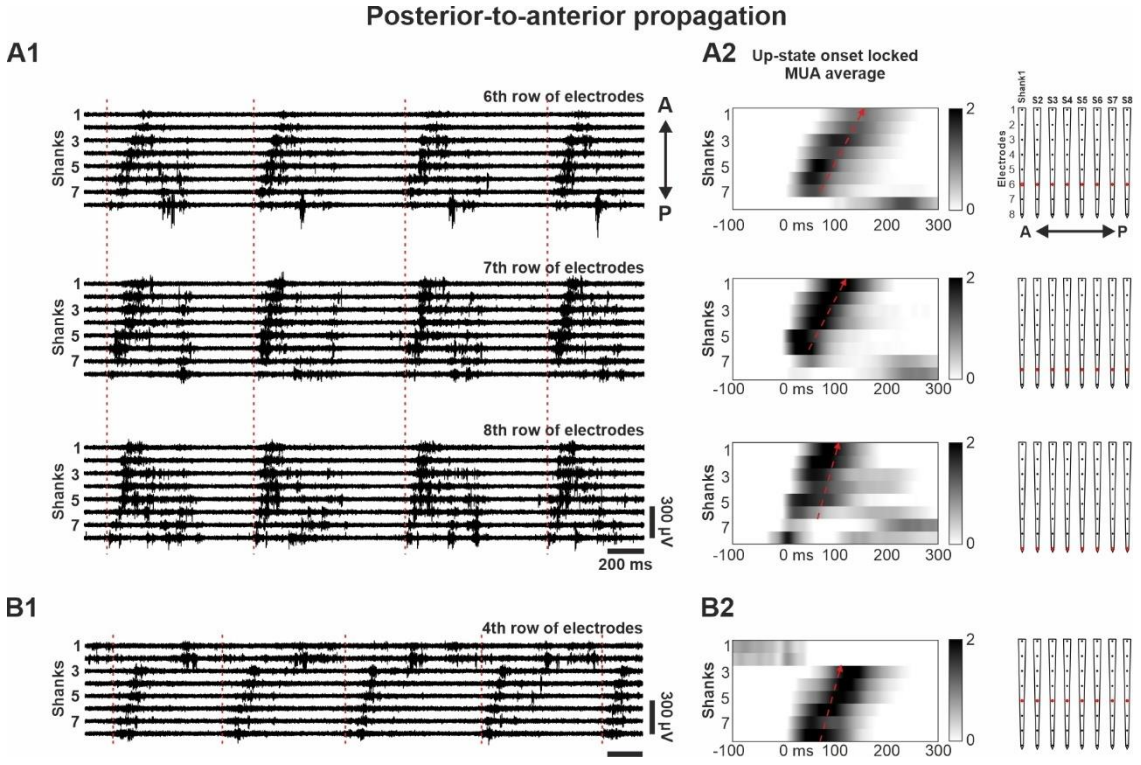

Figure 4. Posterior-to-anterior propagation of population activity observed with multi-shank silicon probes in the thalamus of anesthetized rats. *(A1) Representative thalamic multiunit activity (MUA) recording obtained by three adjacent rows of electrodes on eight shanks of the recording probe from an anesthetized rat. Up-state onsets are indicated by dashed red vertical lines. (A2) Normalized (z-score) MUA depth profile averages locked to the up-state onsets (n = 2007 up-states) on the three rows of electrodes showing posterior-to-anterior propagation in the thalamus (oblique dashed red arrow). The up-state starts at time point zero. The row of electrodes used is indicated on the right in red. (B1-B2) Example*

recording from another rat obtained with a single row of electrodes (n = 2051 up-states). A – anterior; P – posterior.

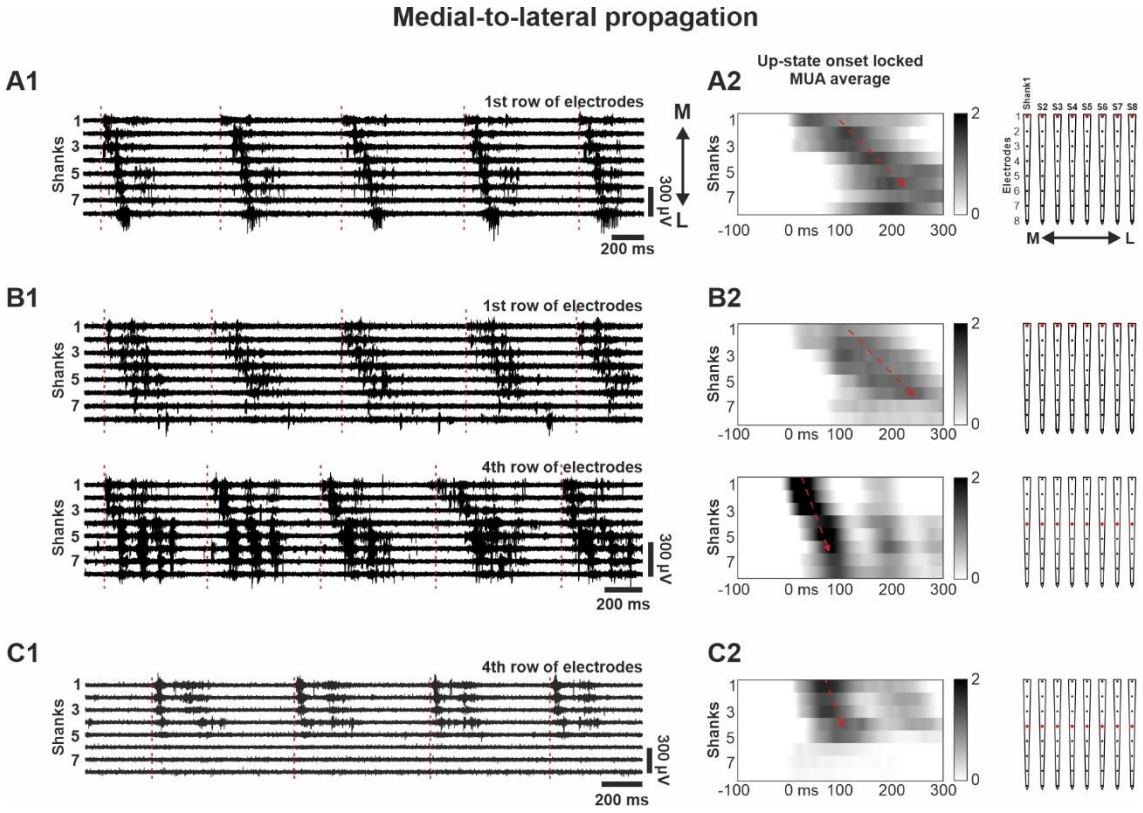

Figure 5. Medial-to-lateral propagation of population activity observed with multi-shank silicon probes in the thalamus of anesthetized rats. *(A1) Representative thalamic MUA recording obtained by a single row of electrodes on eight shanks of the recording probe from an anesthetized rat. Up-state onsets are indicated by dashed red vertical lines. (A2) Normalized (z-score) MUA depth profile average locked to the up-state onsets (n = 2608 up-states) on the row of electrodes showing medial-to-lateral propagation in the thalamus (oblique dashed red arrow). The up-state starts at time point zero. The row of electrodes used is indicated on the right in red. (B1-B2 and C1-C2) Example recordings from two other rats (n = 1983 and 1867 up-states, respectively). M – medial; L – lateral.*

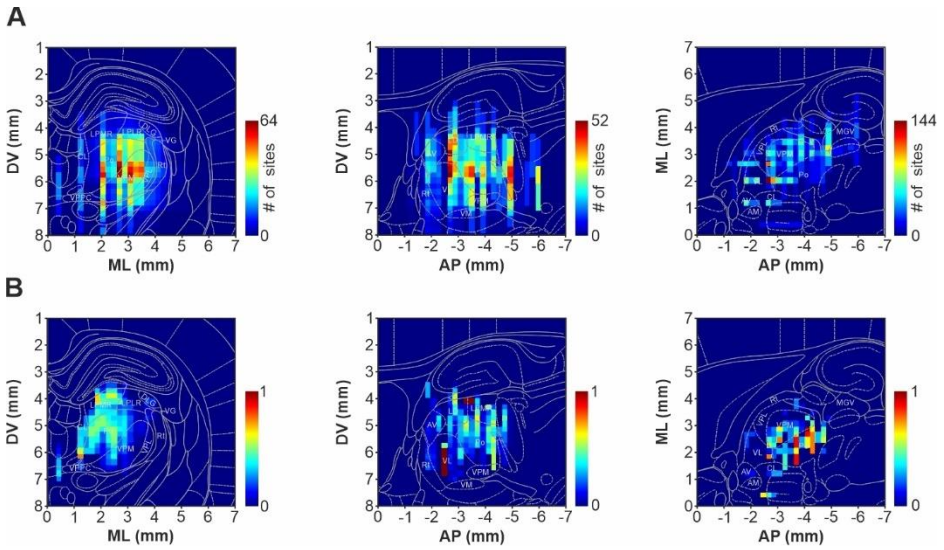

Figure 6. Colormaps illustrating the distribution of recording site locations used to collect thalamic activity with multi-shank silicon probes in anesthetized rats *(A) along the three anatomical axes (left: anterior-posterior (AP) axis; middle: medial-lateral (ML) axis; right: dorsal-ventral (DV) axis), and the probability of observing propagating activity along the dorsoventral axis at these sites (B). Each pixel within these colormaps represents a small quadratic region in the brain with an area of 0.2 mm x 0.2 mm. The pixel values represent cumulative values along one of the three anatomical axes. Schematic brain sections overlaid on the colormaps indicate the location of relevant thalamic nuclei at coordinates AP -3.6 mm (left), ML 1.9 mm (middle) and DV 5.6 mm (right), relative to the bregma.*

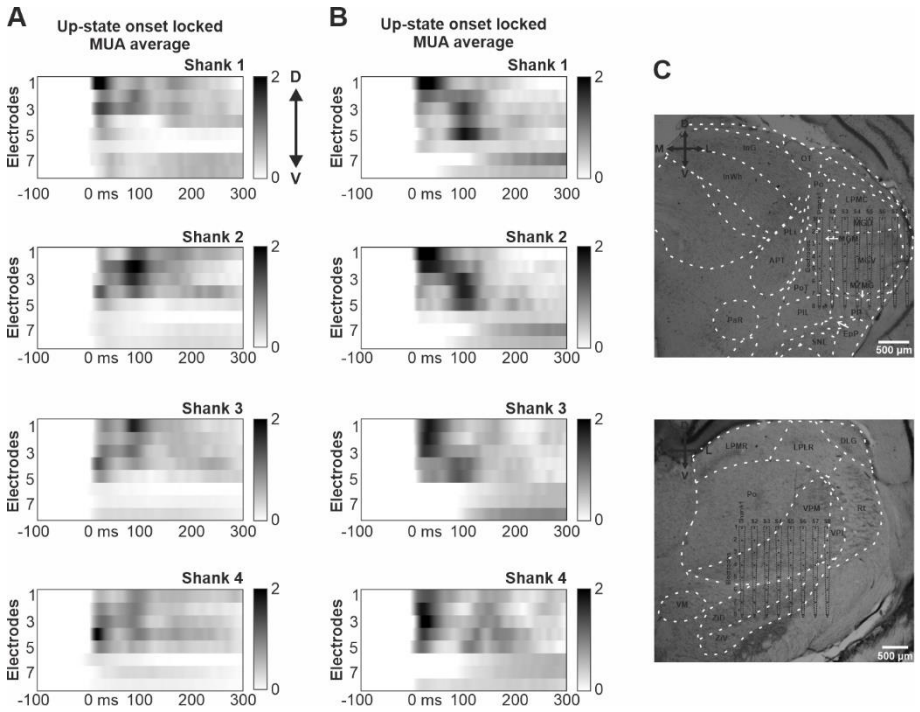

Figure 7. Synchronous multiunit activity at the up-state onset observed in the thalamus with multi-shank probes in anesthetized rats. *(A-B) Normalized (z-score) up-state onset locked MUA depth profile averages on four shanks located in ventral (A; ventrobasal complex; n = 1285 up-states) and posterior (B; auditory thalamic nuclei; n = 2269 up-states) regions of the thalamus. The up-state starts at time point zero. Note that MUA at the up-state onset starts nearly simultaneously on different electrodes. (C) Nissl-stained coronal brain sections illustrating the approximate location of the shanks and electrodes of the silicon probe relative to major thalamic nuclei (top brain section corresponds to panel A; bottom brain section corresponds to panel B). D – dorsal; V – ventral; M – medial; L – lateral.*

Implanting neural probes with multiple shanks may cause considerably greater tissue damage than single-shank devices. Depending on their construction, they could potentially cause more serious brain tissue alteration and pose additional challenges in avoiding elements of the brain's vascular system during the implantation process. These disadvantages originate from the larger total volume they take up (246, 247). After completing histological processing, we frequently noticed bleeding or tissue damage near the insertion site in the brain tissue sections (Fig. S8A). In severe cases, the hemorrhage can fully isolate whole

shanks from neural tissue, leading to significantly reduced amplitude or even the absence of MUA (Fig. S8B).

After successfully identifying the thalamic areas that showed the propagation of population activity, we proceeded to the next step in our study. In this phase, we further investigated thalamic slow-waves using single-shank, high-density Neuropixels 1.0 silicon probes (n = 46 insertions; Table 1; Figure 9.). Through taking advantage of a single shank probe, we efficiently targeted our attention on the pre-established regions, which led to a significant decrease in brain tissue impairment. Furthermore, because of the increased electrode density, we acquired a more reliable and detailed representation of the spatiotemporal patterns of multi-unit activity (MUA) occurring in the thalamic regions.

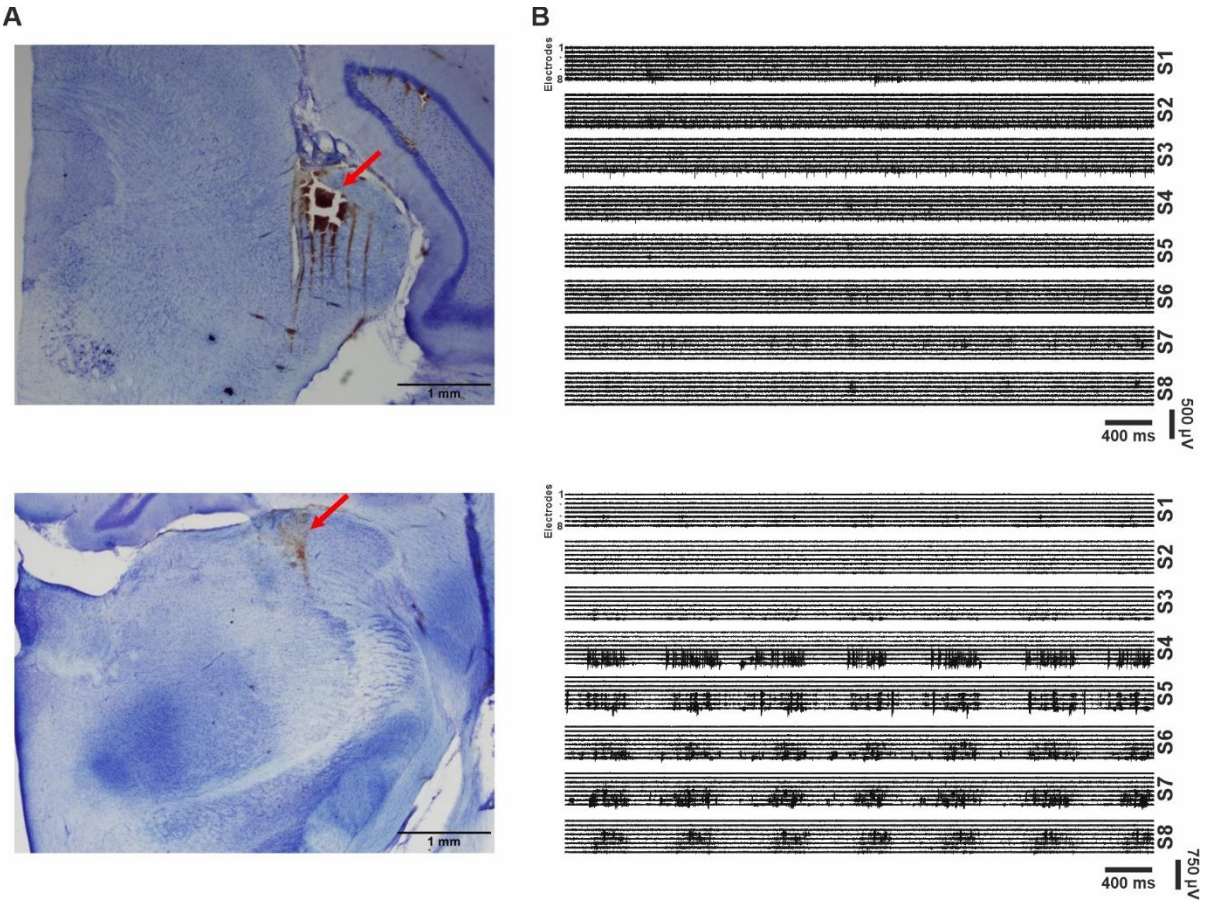

Figure 8. *(A) Nissl-stained coronal rat brain slices with signs of bleeding and tissue damage in the thalamus (red arrows). (B) Sample MUA traces recorded with multi-shank probes at thalamic sites shown in panel A. Note the significantly reduced MUA on all shanks (S1-S8) in the top example and on the first three shanks (S1-S3) in the bottom example.*

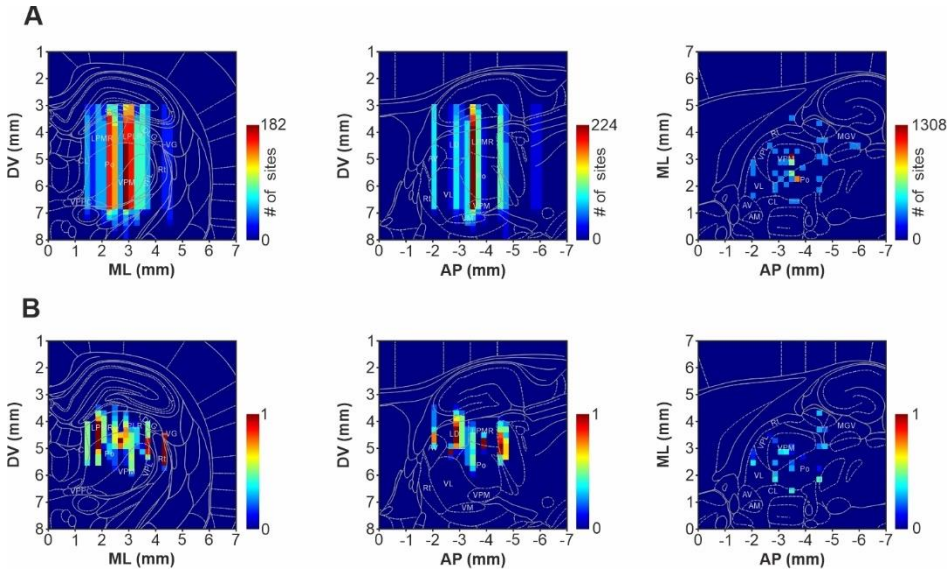

Figure 9. Colormaps showing the distribution of all recording site locations used to collect thalamic activity with single-shank Neuropixels high-density silicon probes in anesthetized rats *(A) along the three anatomical axes (left: anterior-posterior (AP) axis; middle: medial-lateral (ML) axis; right: dorsal-ventral (DV) axis), and the probability of detecting propagating activity along the dorsoventral axis at these sites (B). Each pixel within these colormaps represents a small quadratic region in the brain with an area of 0.2 mm x 0.2 mm. The pixel values represent cumulative values along one of the three anatomical axes. Schematic brain sections overlaid on the colormaps indicate the location of relevant thalamic nuclei at coordinates AP -3.6 mm (left), ML 1.9 mm (middle) and DV 5.6 mm (right), relative to the bregma.*

The Neuropixels probes recorded spontaneous thalamic activity in anesthetized rats, also revealed a gradual propagation of the multi-unit activity (MUA) inside and between the

dorsal thalamic nuclei such as the Po (Fig. 11A), the LP (Fig. 11A and B) or the dorsal lateral geniculate nucleus (DLG; Fig. 11C; propagation was detected in 34 out of 41 recordings, ~83%). The MUA depth profiles, aligned with the up-state onset locked MUA depth profiles, also indicated that the predominant direction of MUA propagation in the dorsal nuclei was ventral-to-dorsal. Additional patterns could be identified, such as the propagation of activity from the dorsal to ventral regions, the initiation of activity at a particular location in the thalamus and its propagation in both dorsal and ventral directions, or the synchronous multi-unit activity (MUA) as shown in Figure 10.

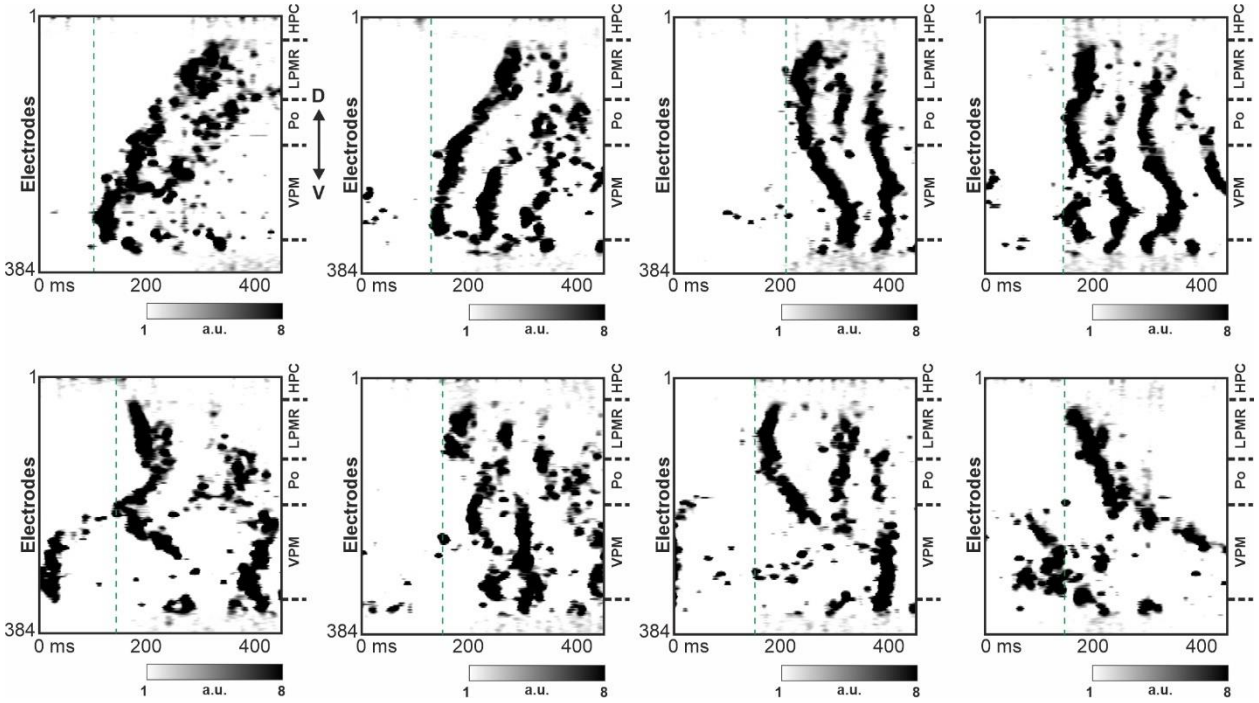

Figure 10. Examples showing the variety of thalamic propagation patterns in a single recording from an anesthetized rat. *Boundaries of major thalamic nuclei are marked by horizontal dashed lines on the right side of the multiunit activity maps. Vertical dashed green lines mark the approximate onset of up-states.*

However, the multi-unit activity (MUA) in the ventral regions of the thalamus occurred almost at the exact same time as the initiation of the up-state (Fig. 11A-C). In other thalamic areas, such as the ventral or dorsal parts of the medial geniculate nucleus (MGV and MGD),

the up-states are also initiated roughly simultaneously at different depths within the thalamus (Fig. 11D).

Additionally, it is essential to mention that propagation patterns were detected in specific thalamic nuclei during sleep spindles, such as the VPM and VPL (as shown in Figure 4A). However, the primary difference is that compared to the propagation of multi-unit activity (MUA) during up-states, the propagation during sleep spindles was steeper, indicating that it was faster. Furthermore, it is intriguing that the individual spindles comprising each cycle may exhibit distinct propagation patterns within a cycle. Additionally, it was less consistent and more variable, as multiple spindle cycles could occur within a single up-state, and each spindle cycle could exhibit a distinct propagation pattern. In addition, the thalamic multi-unit activity (MUA) depth profile reveals that, on average, the MUA associated with sleep spindles in the VPM/VPL nuclei began virtually simultaneously at the start of the up-state. Interestingly, a less prominent pattern of propagation can be observed in subsequent spindle cycles (Fig. 11A). Due to our primary focus on describing the propagation of slow-waves, we did not conduct any further analysis on the characteristics of propagation during sleep spindles.

To summarize, the thalamic multi-unit activity (MUA) during up-states exhibits propagating behavior in rats anesthetized by ketamine/xylazine. Propagation primarily occurs in the dorsal regions of the thalamus, which are typically dominated by higher-order nuclei. The range of propagation distance varied from several hundred micrometers to a maximum of 1.8 mm (1.14 ± 0.39 mm). The propagation delay was approximately 100 ms, leading to a propagation speed of 14.6 ± 8.6 mm/s (measured in n = 13 Neuropixels recordings).

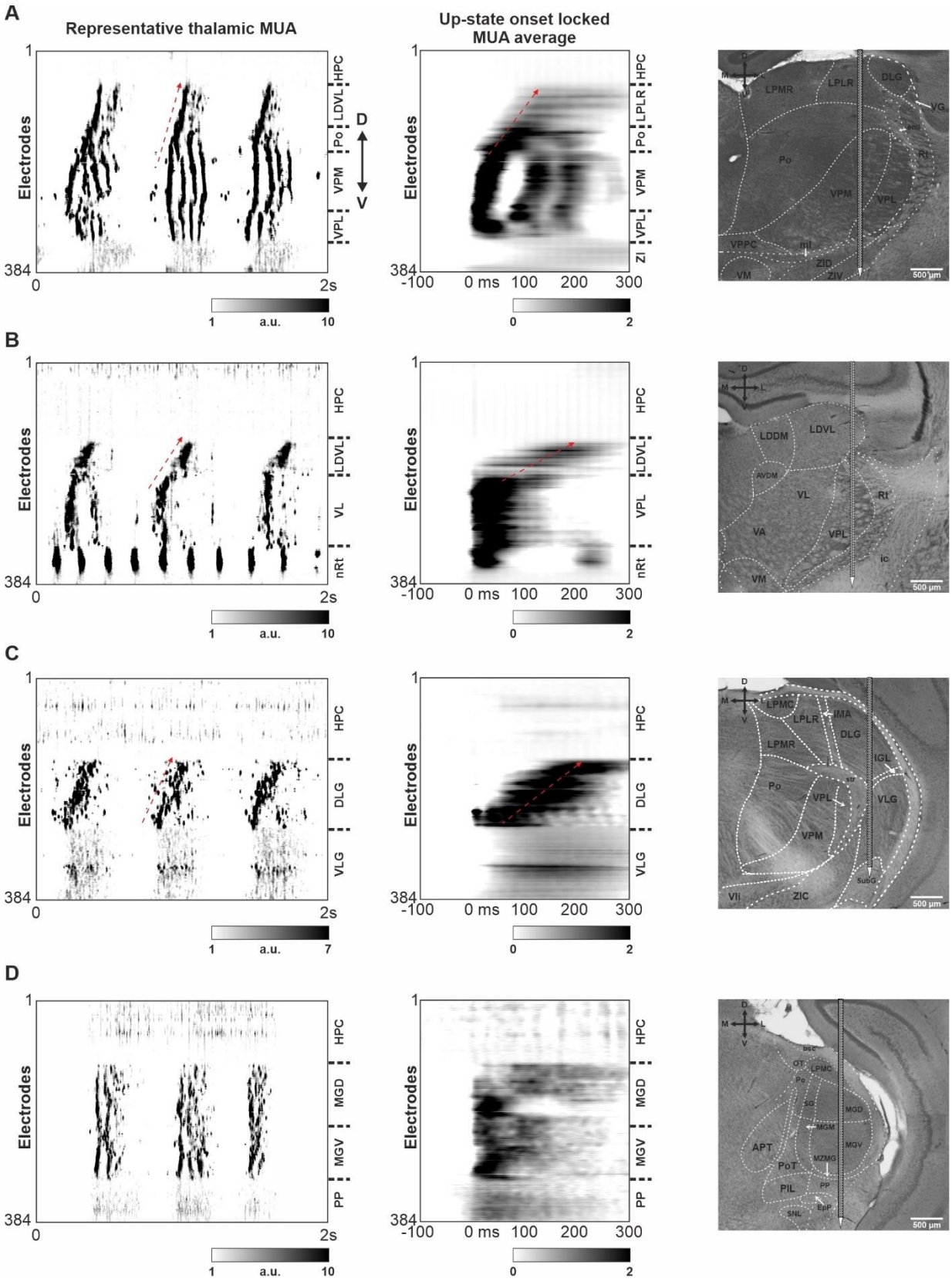
A
Representative thalamic MUA
Up-state onset locked MUA average
Electrodes
1
384
0
2s
HPC
LDVL
Po
VPM
VPL
D
V
-100
0 ms
100
200
300
1
a.u.
10
0
2
LPMR
LPLR
DLG
VG
Rt
VPPC
ZID
ZIV
VM
500 µm
B
LDDM
AVDM
VL
VA
nRt
ic
C
LPMC
IMA
IGL
VLG
ZIC
SubG
7
D
MGD
MGV
PP
APT
PoT
PIL
SNL
EpP
MZMG

Figure 11. Propagating thalamic population activity observed with single-shank high-density silicon probes under ketamine/xylazine anesthesia in rats. *(A-C) Left: two-second-long recordings of spontaneous multiunit activity from different thalamic regions demonstrating the characteristic ventral-to-dorsal pattern of MUA propagation during up-states. To improve the visualization of neuronal activity, the grayscale MUA maps are smoothed both in time (50 Hz low-pass filter) and in space (data from two adjacent electrodes are averaged). Boundaries between major thalamic nuclei are marked by horizontal dashed lines on the right side of the MUA maps. Oblique dashed red arrows indicate the direction of propagation. Middle: normalized (z-score) up-state onset locked MUA depth profile averages (n = 2398, 3488 and 1787 up-states for panels A-C, respectively). The up-state starts at time point zero. Right: Nissl-stained coronal brain sections illustrating the approximate location of the probe shank and electrodes relative to major thalamic nuclei. (D) Another thalamic recording position without visible MUA propagation (the MUA average was computed from n = 645 up-states). D – dorsal; V – ventral; M – medial; L - lateral.*

4.2 Up-states in the dorsal thalamus tend to propagate primarily in the ventral to dorsal direction.

After the visual evaluation, it proved obvious that the propagation of MUA in the thalamic nuclei we examined shows a preference for propagating from the ventral to dorsal direction (see Figs. 1, 4 and 5A) along the dorsoventral axis. However, it is clear that in addition to the prevailing pattern, various patterns can be identified, including propagation in the opposite direction (Fig. 12B). It is important to recognize that these patterns of propagation might differ not only in their direction but also in their speed to a significant extent (Fig.5A and B, left vs. right). Based on our observations, the average propagation speed was around 15 millimeters per second. Afterward, we measured the occurrence and proportion of various propagation patterns. The quantification was derived from 15 recordings in which distinct and consistent patterns of thalamic propagation were identified. To carry out this, we determined three positions evenly spaced in the region where MUA propagation occurred. These locations were associated with the dorsal and ventral boundaries of the propagation,

and a location was placed precisely halfway between the two borders (see the Methods section for more details; Fig. 12C). Subsequently, we analyzed the sequence of MUA initiation at each up-state position and calculated the frequency of the various sequences.

As expected, out of the six propagation patterns, the ventral-to-dorsal direction was the most prevalent, appearing in around 71% of cases (Fig. 12C). The other five patterns had lower occurrence rates, ranging from 3% to 10% (Fig. 12C). The up-state onset supports the presence of different propagation patterns locked MUA depth profiles, which were obtained from up-states that correspond to these specific patterns (e.g., ventral-to-dorsal and dorsal-to-ventral; Fig. 12D). As a result, it can be concluded that although the ventral-to-dorsal propagation pattern is mainly observed, there are also additional recognizable patterns, some of which are more complex, in the anesthetized rat thalamus (Fig. 17).

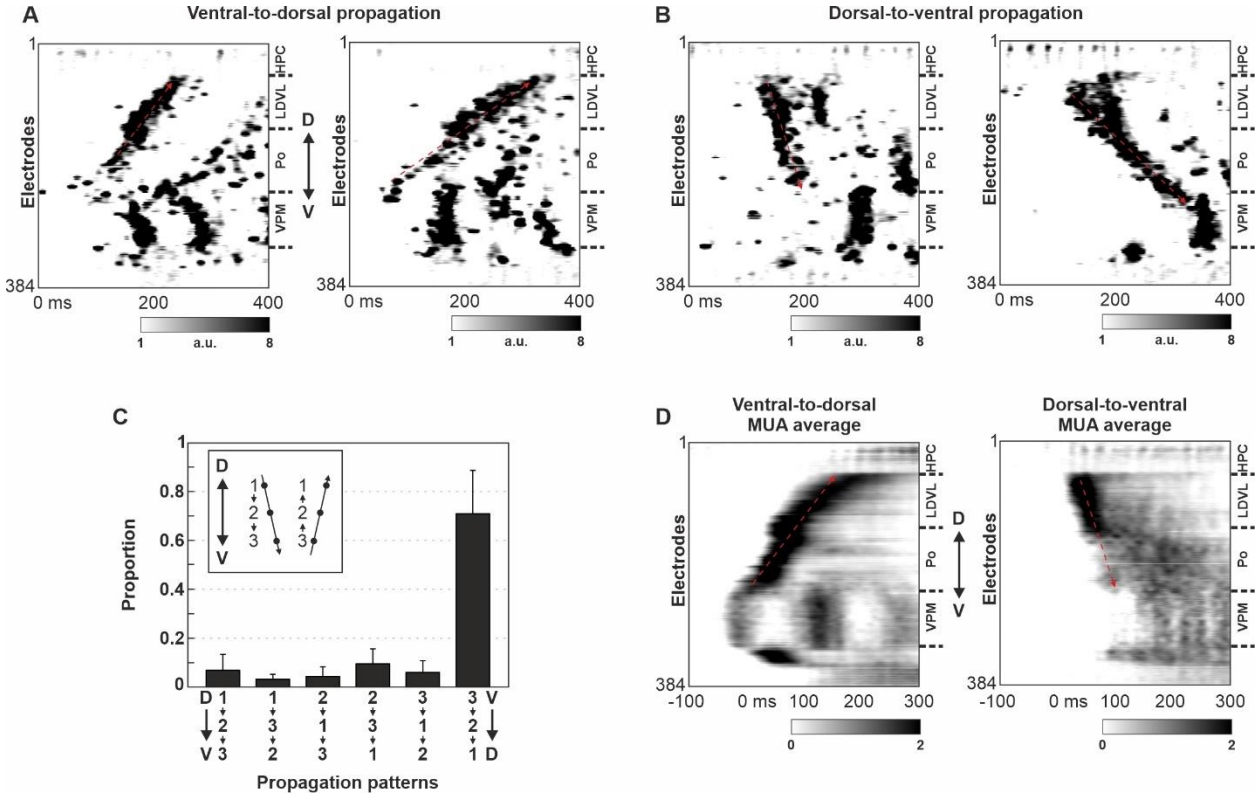

Figure 12. Distinct propagation patterns can be observed in the dorsal thalamus of anesthetized rats, but propagation in the ventral-to-dorsal direction is the most frequent. *(A) Two examples of the characteristic ventral-to-dorsal MUA propagation in the dorsal*

thalamus. Note the difference in propagation speed between the two up-states. (B) Two examples of the less frequent dorsal-to-ventral propagation pattern recorded at the same thalamic location. Note the difference in the propagation speed between the two up-states. (C) Proportion of different thalamic propagation patterns (n = 15 recordings from 14 rats). Sequence 1-2-3 corresponds to dorsal-to-ventral propagation, while sequence 3-2-1 indicates the proportion of up-states with ventral-to-dorsal propagation. Thalamic locations: 1 – most dorsal, 2 – midway between locations 1 and 3; 3 – most ventral. (D) Normalized (z-score) up-state onset locked MUA depth profile averages for the ventral-to-dorsal (left, n = 980 up-states) and dorsal-to-ventral (right, n = 335 up-states) propagation patterns in a single animal. MUA averages were calculated from the same recording from which examples are shown in panels A and B. Boundaries of major thalamic nuclei are marked by horizontal dashed lines on the right side of the MUA maps. Oblique dashed red arrows indicate the direction of propagation. The up-state starts at time point zero. D – dorsal, V – ventral.

4.3 Spontaneously arising dorsal thalamic up-states are synchronized with cortical up-state activity.

In the thalamocortical system, it is well-known that the propagation of slow-waves under anesthesia in rodents is observed along the anterior-posterior axis in the neocortex, as described by Greenberg et al. (184), Greenberg and Dickson (200), Ruiz-Mejias et al. (203), and Stroh et al. (195). After assessing both spatial distributions of slow-waves in the thalamus, we aimed to gain insight into the relationship between the patterns of multi-unit activity (MUA) during cortical and thalamic up-states. We performed additional experiments (n = 5 rats) to address this question. We inserted a Neuropixels 1.0 probe into the thalamus, specifically targeting regions most likely to exhibit propagation, such as the Po, LD, and VPM nuclei. We also implanted an eight-shank silicon probe aligned along the anterior-posterior axis and recorded simultaneous neural activity from the neocortex. During these simultaneous thalamocortical recordings, we observed that multi-unit activity (MUA) in the cortex typically began at the electrodes located anteriorly located shanks (or almost simultaneously on all electrodes), while thalamic activity followed a distinct pattern of

propagating from the ventral-to-dorsal, with MUA starting in the ventral region of the Po and concluding in the dorsal region of the LD nucleus (see Figure 6).

In order to investigate the possible impact of the neocortex on thalamic activity patterns, we computed and contrasted MUA depth profiles that were locked to either cortical (Fig. 14 B and D) or thalamic up-state onsets. For up-state onset detection, we incorporated depth profiles from either all dorsal thalamic channels (refer to Fig. 13A) or those channels that exhibited activity propagation exclusively (see Fig. 13B). The thalamic MUA depth profiles that most clearly demonstrated ventral-to-dorsal propagation were those synchronized with cortical up-state onsets (compare Fig. 14B and D vs. Fig. 13), suggesting a tight temporal alignment of dorsal thalamic MUA with cortical up-states and a significant influence of the neocortex on thalamic propagation patterns. Another notable finding was that in four out of five rats, MUA associated with up-states initiated in the ventral part of the Po nucleus, preceding the onset of cortical up-states by approximately 50 ms (Fig. 14B and D). Additionally, the propagation speed of thalamic MUA was recorded at 12.4 ± 4.5 mm/s, significantly slower compared to the cortical MUA, which propagated at a rate roughly three times faster, averaging 37.9 ± 18.0 mm/s.

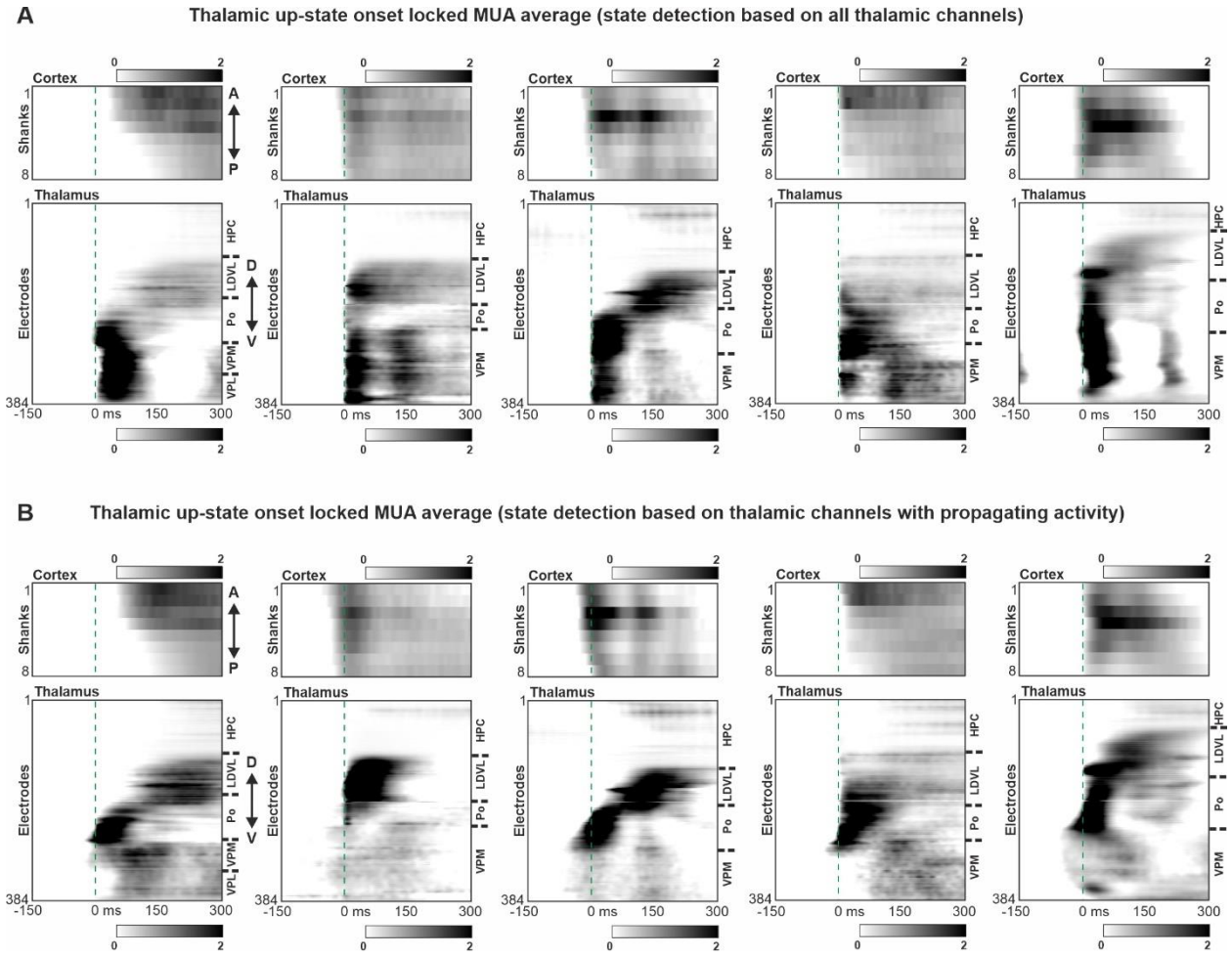

Figure 13. *(A) Normalized (z-score) thalamic up-state onset locked (using all thalamic channels for up-state onset detection) cortical (top) and thalamic (bottom) MUA depth profile averages of simultaneous cortical and thalamic recordings from five different animals (n = 4721, 4459, 2215, 2469 and 3577 up-states from left to right, respectively). (B) Here, only that part of the thalamus was selected for up-state detection that showed activity propagation (n = 3000, 3419, 1792, 2069 and 4180 up-states from left to right, respectively). Boundaries of major thalamic nuclei are marked by horizontal dashed lines on the right side of the MUA maps. Vertical dashed green lines mark the thalamic up-state onsets.*

To investigate the connections between the spontaneously emerging cortical and thalamic MUA propagation patterns, we initially identified the primary characteristics of both cortical and thalamic MUA patterns, as mentioned earlier. The ventral-to-dorsal propagation was the

most prevalent in the thalamus. At the same time, in the cortex, we noticed that the primary direction of up-state propagation was anterior-to-posterior, corresponding to approximately 49% of up-states (Fig. 15A). The thalamus predominant pattern of ventral-to-dorsal propagation occurs at a similar frequency as the anterior-to-posterior traveling cortical up-states (about 55%, as shown in Figure 7B). Therefore, cortical anterior-to-posterior propagation patterns were frequently accompanied by ventral-to-dorsal MUA propagation in the thalamus; however, only with an incidence similar to the frequency of ventral-to-dorsal propagation in the thalamus (~52% of up-states, Fig. 15C). However, the ventral-to-dorsal propagation in the thalamus was even more pronounced in the MUA depth profiles that were synchronized with the anterior-to-posterior cortical up-state onsets (for example, see the comparison between the third column of Fig. 14D and Fig. 15C).

In addition, there was a noticeable occurrence of cortical up-states propagating in the opposite direction (from posterior to anterior), which happened less frequently (approximately 13% of up-states). This was often observed in conjunction with thalamic multi-unit activity (MUA) propagating from the dorsal to ventral direction (which is opposite to the most common direction of thalamic propagation, occurring approximately 11% of the time, as shown in Figure 7D). Remarkably, in one of the rats that were studied, this connection was observed in the multi-unit activity (MUA) depth profile, which was synchronized with cortical up-states that spread from the posterior to the anterior direction (Fig. 15D) . Therefore, while each thalamic propagation pattern can occur in the thalamus during each of the cortical traveling patterns, our results indicate that there can be a weak correlation between the ongoing cortical and thalamic MUA patterns.

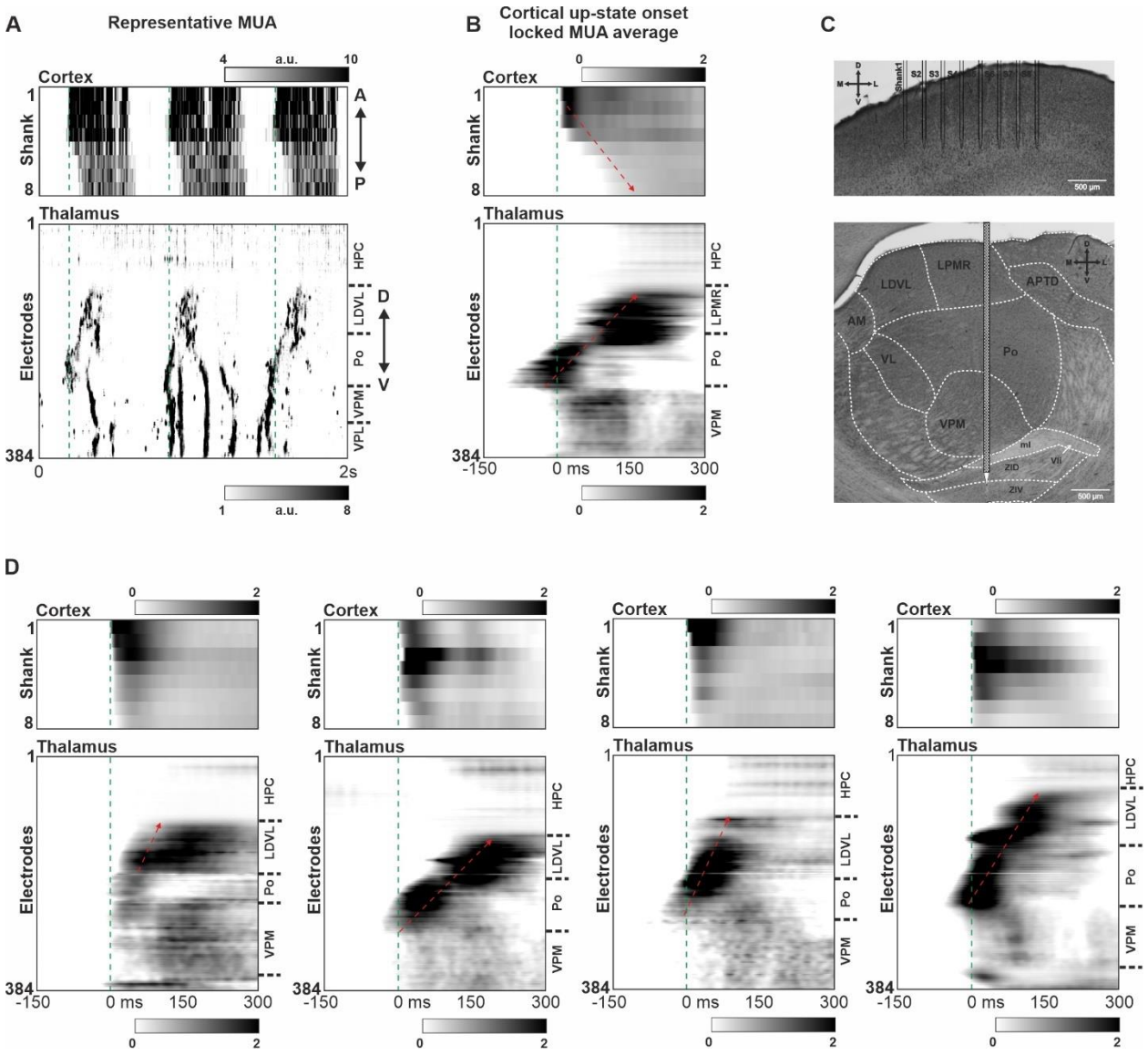

Figure 14. Simultaneous cortical and thalamic multiunit activity recordings in anesthetized rats display propagation of neuronal activity during up-states in both regions. *(A) Two-second-long representative recordings from the neocortex (top, multi-shank probe) and the thalamus (bottom, Neuropixels probe) demonstrating anterior-to-posterior propagation in the neocortex and the characteristic ventral-to-dorsal propagation in the thalamus. For the neocortex, MUA recorded by all electrodes (n = 8) located on a single shank was averaged for each shank. (B) Normalized (z-score) cortical up-state onset locked cortical (top) and thalamic (bottom) MUA depth profile averages (n = 3420 up-states) of one of the experiments. (C) Nissl-stained sagittal brain section illustrating the approximate*

location of the shanks and electrodes of the two silicon probes in the neocortex (top) and the thalamus (bottom). (D) Cortical up-state onset locked MUA depth profile averages in the other four rats (n = 4159, 1803, 2341 and 5141 up-states from left to right, respectively). Boundaries of major thalamic nuclei are marked by horizontal dashed lines on the right side of the MUA maps. Oblique dashed red arrows indicate the direction of propagation. Vertical dashed green lines mark the cortical up-state onsets. A – anterior, P – posterior, D – dorsal, V – ventral.

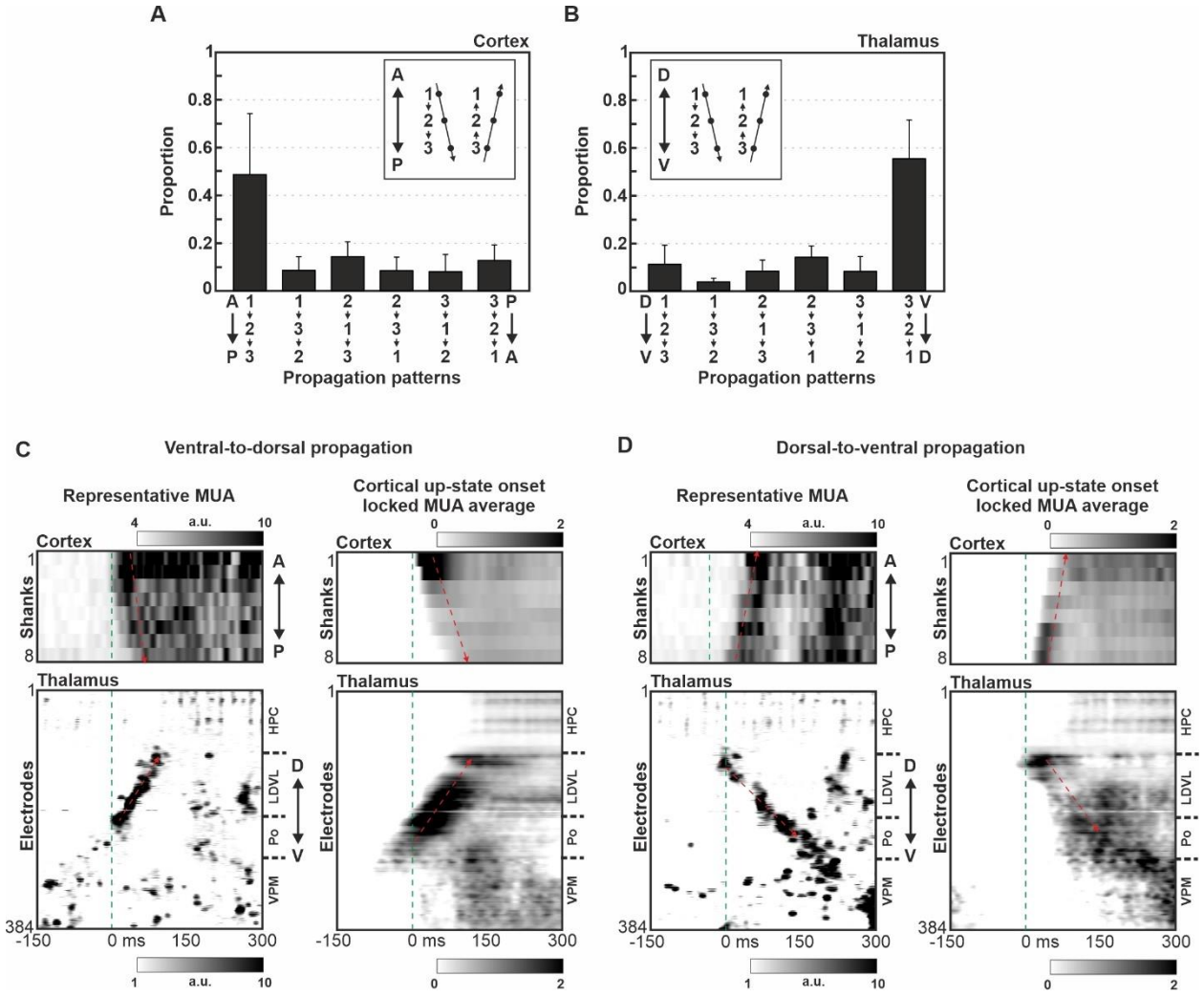

Figure 15. Cortical and thalamic propagation patterns observed during up-states are weakly correlated. *(A) The proportion of distinct cortical propagation patterns (n = 5 thalamocortical recordings). Sequence 1-2-3 corresponds to anterior-to-posterior*

propagation, while sequence 3-2-1 indicates the proportion of up-states with posterior-to-anterior propagation. Cortical locations used to examine propagation patterns: 1 – between anteriorly located shanks 1 and 2, 2 – between shanks 3 and 4; 3 – between posteriorly located shanks 7 and 8. (B) The proportion of

different thalamic propagation patterns in the same recordings. Sequence 1-2-3 corresponds to dorsal-to-ventral propagation, while sequence 3-2-1 indicates the proportion of up-states with ventral-to-dorsal propagation. Thalamic locations: 1 – most dorsally located electrodes in the thalamus displaying MUA propagation, 2 – midway between location 1 and 3; 3 – most ventral electrodes in the thalamus displaying MUA propagation. (C) Left: Example of a thalamic ventral-to-dorsal MUA propagation during a cortical up-state traveling in the anterior-to-posterior direction. Right: Normalized (z-score) cortical up-state onset locked cortical (top) and thalamic (bottom) MUA depth profile averages (n = 887 anterior-to-posterior cortical up-states). (D) Left: Example of a thalamic dorsal-to-ventral MUA propagation during a cortical up-state traveling in the posterior-to-anterior direction. Right: Normalized (z-score) cortical up-state onset locked cortical (top) and thalamic (bottom) MUA averages (n = 190 posterior-to-anterior cortical up-states). Boundaries of major thalamic nuclei are marked by horizontal dashed lines on the right side of the MUA maps. Oblique dashed red arrows indicate the direction of propagation. Vertical dashed green lines mark the cortical up-state onsets. A – anterior, P – posterior, D – dorsal, V – ventral.

4.4 Thalamic multiunit activity has similar propagation properties during spontaneous up-states in anesthetized mice

In further investigations of spontaneously occurring thalamic up-states, we were also curious whether similar patterns could be discovered in other rodent species. To answer this question, we measured population activity from the thalamus of ketamine/xylazine-anesthetized mice using Neuropixels probes (Fig. 16A and B) as well as multi-shank silicon probes (Fig. 16C and D). Although thalamic MUA propagation in up-states was reliably observed, the smaller size of the mouse thalamus compared to that of rats limited the propagation of thalamic population activity to smaller areas, and this size difference also introduced greater

uncertainty in accurately identifying the thalamic nuclei from which activity was recorded, complicating the demarcation of these nuclei. In mice, like in rats, thalamic MUA propagation predominantly occurred in the dorsal region, specifically in higher-order nuclei such as the Po or LD, with the dominant pattern consistently beginning in the ventral areas and progressing dorsally (Fig. 16). Similar to what was observed in rats, additional MUA (multi-unit activity) patterns also occurred, but fewer times. Notably, although the thalamic MUA depth profiles indicated a detectable ventral-dorsal propagation in the mice analyzed, certain parts of the dorsal thalamus were not involved in the observed MUA propagation (see Figure 8C). Similar to the delay in propagation observed in rats, the time between the initiation and termination of the up-state in mice varied between 100 and 300 milliseconds. Assuming the smaller dimensions of the mouse thalamus, this suggests a propagation velocity of marginally slower than 5 mm/s.

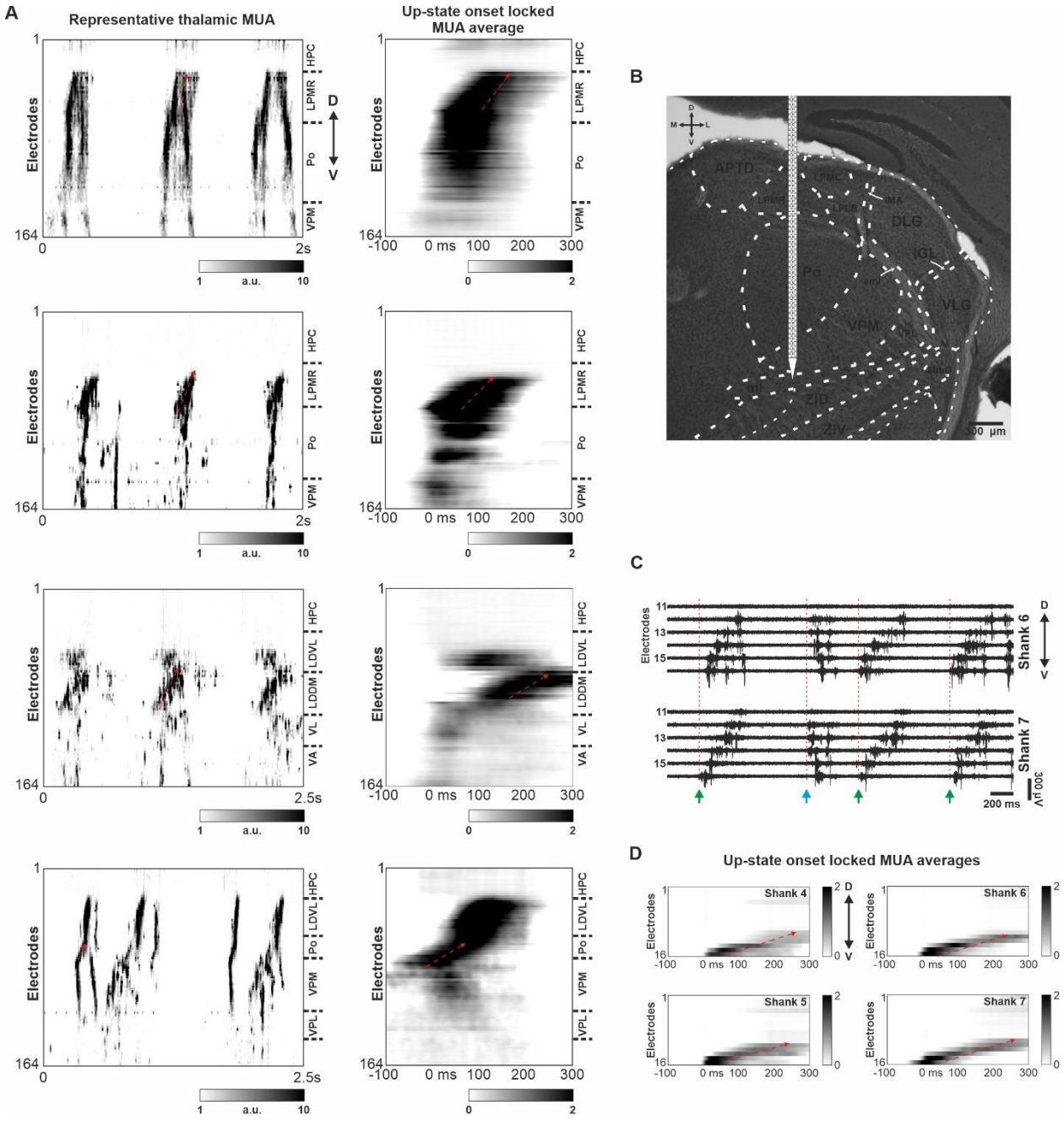

Figure 16. Multiunit activity propagation during up-states observed in the dorsal thalamus of ketamine/xylazine-anesthetized mice. *(A) Left: Two-second-long representative thalamic MUA recordings (Neuropixels) from two mice (n = 2 insertions/mice; top two rows correspond to one animal, bottom two rows correspond to the other mouse). Right: Normalized (z-score) up-state onset locked thalamic MUA depth profile averages (n = 1555,*

2261, 2450, 994 up-states from top to bottom, respectively). (B) Nissl-stained coronal brain section illustrating the approximate location of the probe shank and recording sites (electrodes) relative to major thalamic nuclei. The brain section corresponds to the recording shown in the first row of panel A. (C) Example thalamic MUA recorded in a mouse on two adjacent shanks of a multi-shank probe. Up-state onsets are indicated by vertical dashed red lines. Note ventral-to-dorsal (green arrows) and dorsal-to-ventral (blue arrow) propagation patterns. (D) Normalized (z-score) MUA depth profile averages locked to the up-state onsets (n = 2132 up-states) on shanks 4–7 showing ventral-to-dorsal propagation (dashed red arrow). The MUA average was computed from the recording partially shown in panel C. In the MUA depth profiles, the up-state starts at time point zero. D – dorsal; V – ventral; M – medial; L – lateral.

4.5 Thalamic activity propagation is less frequent and faster during natural sleep in rats

The ketamine/xylazine anesthetic generates artificially slow-waves in experiments and is a well-acknowledged model for investigating natural slow-wave sleep (SWS; (11, 248)). In our subsequent analysis, we sought to ascertain the distinctions between the properties and spatiotemporal patterns of multi-unit activity (MUA) recorded in the thalamocortical system and those observed during natural slow-wave sleep. To investigate potential characteristics of the thalamic multi-unit activity (MUA) and their potential propagating manners, we chronically implanted Neuropixels probes in the thalamus of two rats. Specifically, we targeted the thalamic nuclei (Po and LP) where MUA propagation was typically observed. Following the animals had recovered entirely from the implantation procedure, we carefully monitored their sleep-wave patterns daily for several days. Subsequently, we identified the phases of sleep and wakefulness in these recorded sessions (Fig. 17*).* Thalamic activity during wake periods and REM sleep stages were desynchronized with MUA of active neuronal populations showing no signs of propagation (Fig. 17A). In addition, the population activity measured during NREM sleep allows for a more apparent distinction between adjacent thalamic nuclei (Fig. 17). Due to lower levels of neuronal synchronization compared

to ketamine/xylazine anesthesia, the neuronal activity in the thalamic nuclei examined was mainly independent. In particular, short multi-unit activity (MUA) events were restricted to a single nucleus and exhibited different levels of synchronization. However, at brief time intervals (specifically, for the length of many consecutive up-states), the multi-unit activity (MUA) events between surrounding nuclei were synchronized, with a small subset of these events also exhibiting propagation.

Although we were able to detect the propagation of thalamic population activity during NREM sleep, the rate of occurrence of these events was much lower (1.89 ± 0.72 events/min) compared to ketamine/xylazine anesthesia where clear propagation was observed, on average, during every second up-state (~45 events/min considering 1.5 Hz slow oscillation frequency). To directly compare the properties of propagating thalamic events between anesthesia and natural SWS, we computed the average thalamic MUA depth profiles locked to propagating MUA events visually detected during NREM periods, as well as MUA depth profiles locked to up-state onsets detected during light anesthesia (Fig. 18). Qualitative properties of thalamic up-states emerging during light anesthesia were very similar to those recorded during deep anesthesia, including the preferred direction of propagation (e.g., compare Fig. 11A vs. Fig. 18A). Analogous to anesthesia-induced up-states, thalamic propagating MUA events detected during NREM sleep also displayed a ventral-to-dorsal spread of activity (Fig. 18A vs. Fig. 18B). However, these MUA events were shorter, and the activity propagation was faster compared to up-states recorded under ketamine/xylazine anesthesia (Fig. 18A vs. Fig. 18B). Interestingly, thalamic MUA depth profiles were very similar between the two rats examined, suggesting that consistent and stereotyped activity patterns emerge in this part of the thalamus both during natural sleep and anesthesia (Fig. 18A1 vs. Fig. 18A2; Fig. 18B1 vs. Fig. 18B2). Finally, in a single animal, we also obtained data from the parietal association cortex simultaneously with thalamic activity (see Methods for details). Cortical and thalamic MUA averages locked to detected propagating thalamic MUA events demonstrated that Po activity precedes MUA in the cortex and the LP by around 25 ms, while neuronal activity in the cortex and the LP initiates at a nearly identical time (Fig. 19).

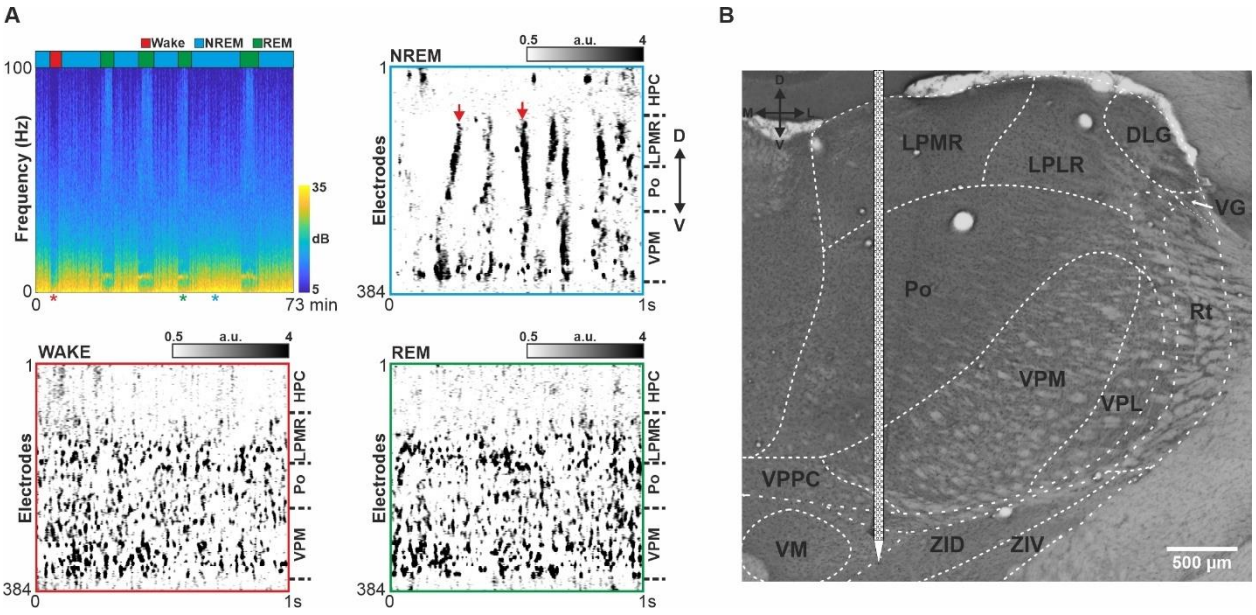

Figure 17. Thalamic MUA propagation is present only during non-rapid eye movement (NREM) sleep in naturally sleeping rats. *(A) Spectrogram (top left) of a 73-minute-long recording session from a chronically implanted (Neuropixels probe) rat showing multiple periods of NREM sleep, REM (rapid eye movement) sleep and wake. A short thalamic MUA snippet is shown for each sleep/wake state (top right, NREM; bottom left, wake; bottom right, REM). Red arrows in the NREM sleep recording demonstrate examples of propagating population activity in the thalamus. Asterisks below the spectrogram mark the time points of the MUA snippets. The color-coded horizontal bars above the spectrogram indicate sleep and wake periods. Boundaries of major thalamic nuclei are marked by horizontal dashed lines on the right side of the MUA maps. (B) Nissl-stained coronal brain section illustrating the approximate location of the probe shank and recording sites (electrodes) relative to major thalamic nuclei in one of the chronically implanted rats.*

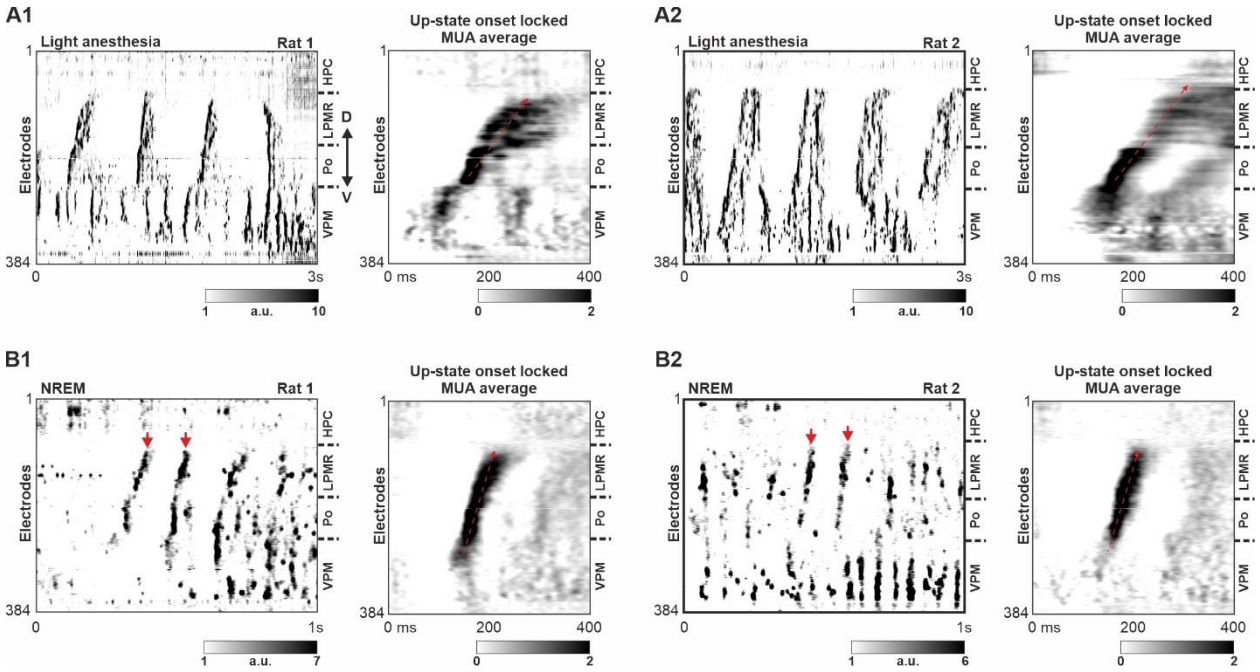

Figure 18. Propagating thalamic population activity during light anesthesia and natural NREM sleep. (A1-A2) *Left: representative thalamic MUA recordings obtained under light anesthesia with a Neuropixels probe at the end of the implantation surgery in two chronically implanted rats. Right: Normalized (z-score) up-state onset locked thalamic MUA depth profile averages (n = 90 and 589 up-states for the two rats, respectively). (B1-B2) Left: representative MUA recordings with propagating activity obtained during NREM sleep in the two chronically implanted animals. Right: Normalized (z-score) thalamic MUA depth profile averages locked to the onset of detected propagating MUA events (n = 407 and 141 up-states for the two rats, respectively). Red arrows in the NREM recording mark examples of propagation population activity in the thalamus. Boundaries of major thalamic nuclei are indicated by horizontal dashed lines on the right side of the MUA maps. Oblique dashed red arrows indicate the direction of propagation. Note the difference in propagation speed between anesthesia-induced MUA propagation and MUA propagation during NREM sleep. D – dorsal, V – ventral.*

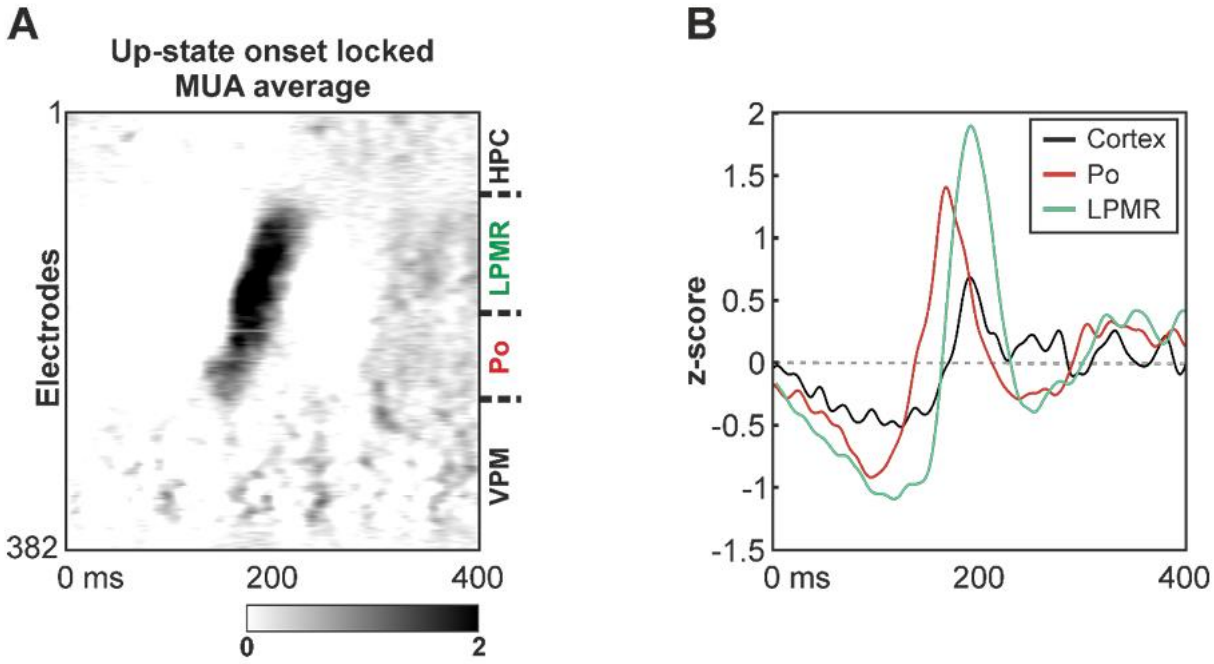

Figure 19. (A) Normalized (z-score) thalamic MUA depth profile average locked to the onset of detected propagating MUA events (n = 123 up-states) during NREM sleep in simultaneous thalamic (n = 382 channels) and cortical (n = 2 channels; parietal association cortex; MUA average shown in panel B) recordings. *Boundaries of major thalamic nuclei are indicated by horizontal dashed lines on the right side of the MUA map. (B) Z-scored MUA averaged across channels and events in the cortex (black, n = 2 channels), Po (red, n = 30 channels) and LPRM (green, n = 42 channels). The MUA average is locked to the onset of propagating thalamic activity. Note that activity in Po starts before MUA in the cortex and LPMR.*

4.6 Results of high-resolution cortical activity data from anesthetized rats

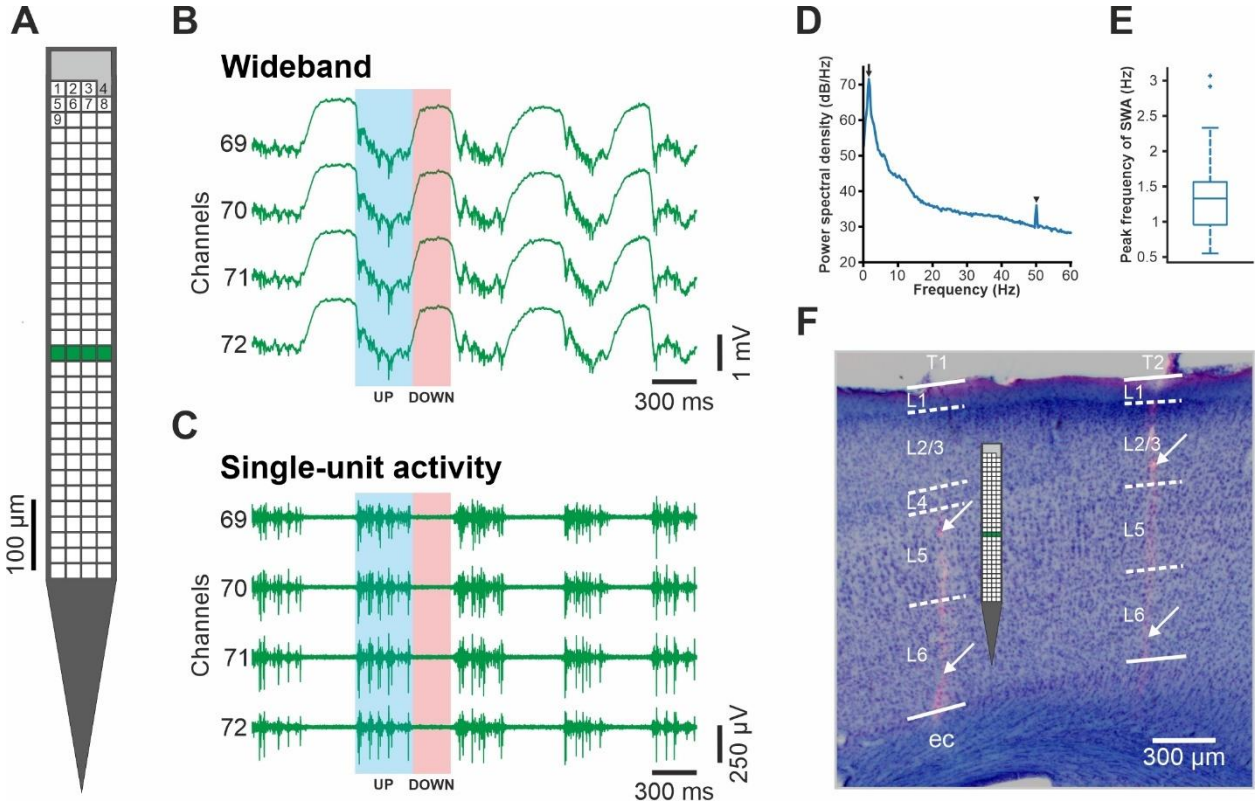

Figure 19. Cortical slow-wave activity (SWA) recorded with high spatial resolution. *(a) Schematic of the 128-site silicon probe used to collect the dataset. Recording sites (white squares) are arranged in a 32 × 4 dense array. The site located in the upper right corner of the array (with gray color) has a larger area and might be used as an internal reference electrode. The recording site – channel mapping is indicated by the numbering located at the top of the array. (b,c) Three-second-long wideband (0.1–7500 Hz) and highpass-filtered (500 Hz; single-unit activity) layer 5 activity in the cortex recorded on four channels (green sites on panel a). Under ketamine/xylazine anesthesia, SWA is the dominant brain rhythm emerging in the cortex. During SWA, two phases alternate: up-states (high spiking activity; example shown with the blue shaded area; UP) and down-states (cessation of spiking activity; example indicated with the red shaded area; DOWN). (d) Power spectrum of a*

recording from deep cortical layers demonstrating the characteristic peak frequency of the SWA at ~1.5 Hz (black arrow). The arrowhead indicates the degree of contamination by the power line (50 Hz) noise. (e) Boxplot showing the distribution of SWA peak frequencies of all recordings (n = 109). The central mark indicates the median, the bottom and top edges of the box mark the 25th and 75th percentiles, respectively. The whiskers extend to the most extreme data points not considered outliers. Outliers are plotted individually using the '+' symbol. The features of boxplots are the same on following figures. (f) The recording positions of the silicon probe (tracks) were verified by examining fluorescent marks of DiI in the cortical brain sections (white arrows). Nissl-staining was used to determine the borders of cortical layers. The probe schematic shows the estimated cortical depth from where traces on panel b and c were acquired. The probe track on the left (T1) is located in the primary somatosensory cortex, while the track on the right (T2) is in the motor cortex. L, layer; ec, external capsule.

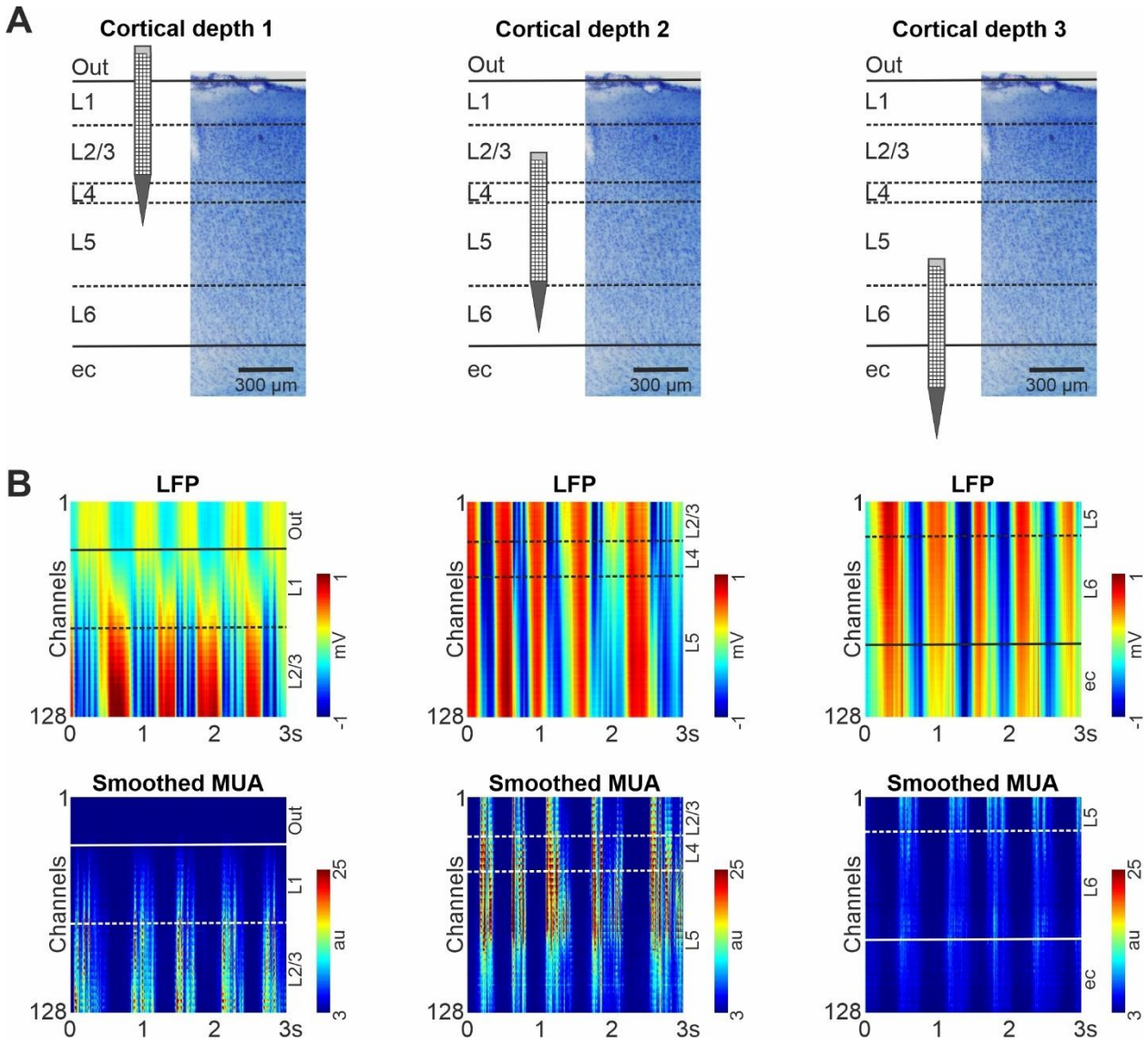

Figure 20. The recording protocol used to collect the cortical data and examples of cortical activity depth profiles. *(a) The silicon probe was first inserted into the superficial layers of the cortex (left; cortical depth 1; some recording sites at the top of the array were outside of the cortex), then after successful data acquisition it was moved to deeper layers (middle; cortical depth 2). In the case the bottommost sites were still located in the cortex (indicated by the measured activity), the probe was advanced deeper (right; cortical depth 3) to collect activity from all cortical layers. (b) Color maps constructed from three-second-long traces of local field potentials (LFP; 0.1–300 Hz; top row) and multi-unit activity (MUA; 300–5000*

Hz, rectified; bottom row). All channels were used to construct the color maps. The MUA was smoothed using a 50 Hz lowpass filter. High and low spiking activity on the MUA color maps are indicated by red and blue colors, respectively. Color maps in the same column correspond to the cortical depth shown directly above the maps, on panel a. Estimated positions of cortical layer boundaries are indicated with dashed lines. The dorsoventral (vertical) tissue coverage of the probe is about 717 µm. au, arbitrary unit; ec, external capsule; L, layer.

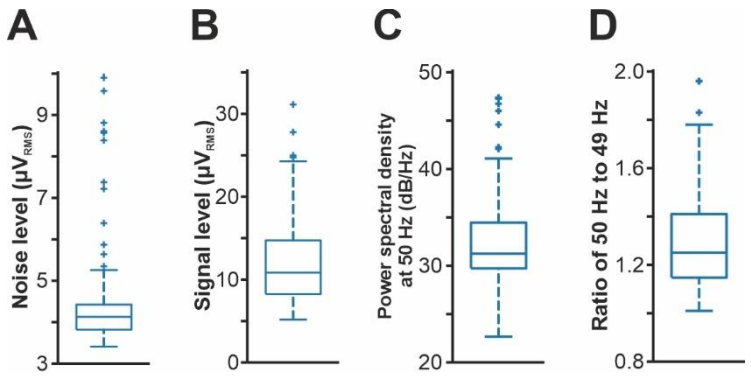

Figure 21. Quality assessment of cortical recordings (n = 109). *(a) Distribution of the root mean square (RMS) noise levels estimated from the recordings. (b) Distribution of the estimated RMS signal levels. (c) Distribution of power spectral density values measured at 50 Hz to demonstrate power line noise contamination (see also panel d of Fig. 19). (d) Distribution of the ratios of the power spectral density value measured at 50 Hz to the power spectral density value computed at a nearby frequency (49 Hz) without power line noise contamination.*

4.7 Extracted single-unit properties.

Following manual curation, we calculated and shared numerous properties related to spike waveforms and firing patterns for the selected single units, as illustrated in Figure 5. From the wideband (0.1–7500 Hz) and the filtered (300–6000 Hz bandpass; 3rd order Butterworth filter) continuous recordings, we also computed multichannel mean spike waveforms for selected single units (examples shown in Figure 23). We segmented the recordings into 4 ms

data snippets (81 sample points in total) around each spike of a particular unit on each channel (with the spike waveform peak located in the center of the snippet) to calculate the average waveforms, then averaged the spikes and calculated the standard deviations.

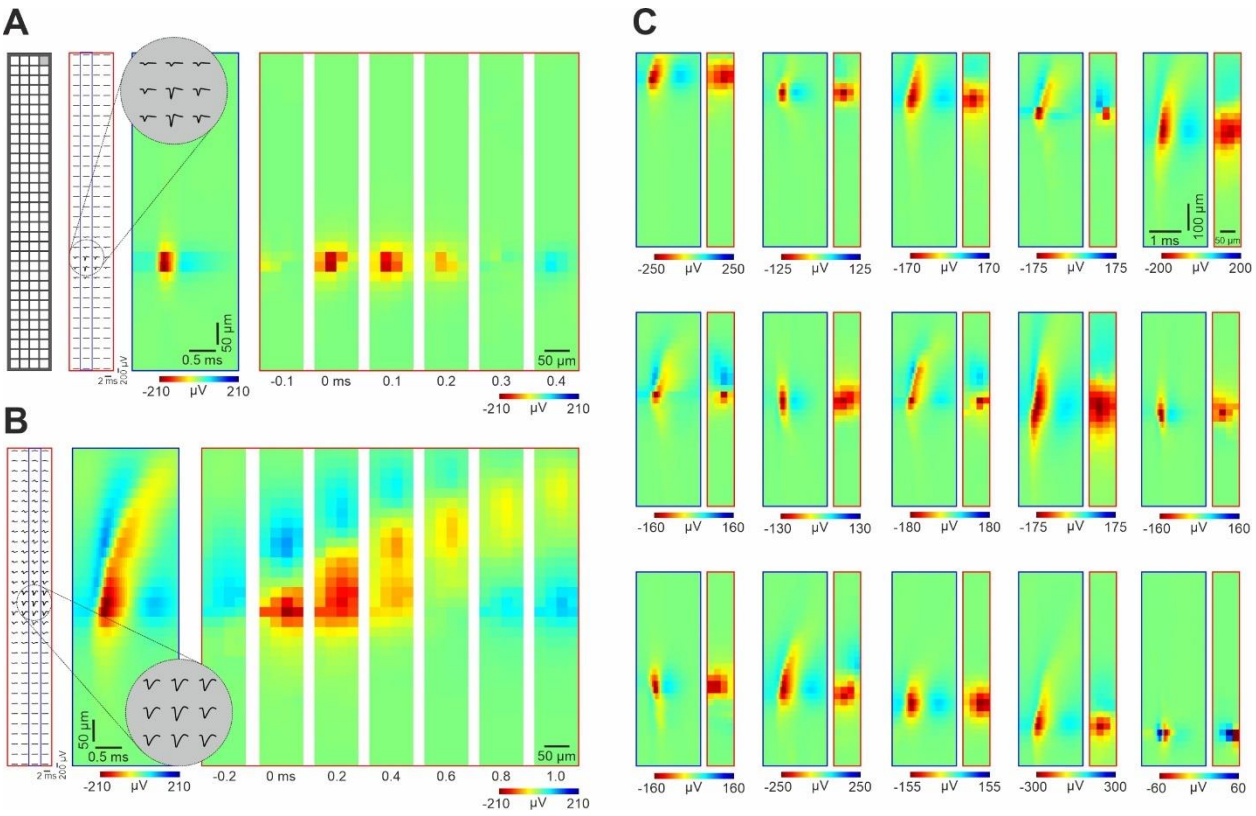

Figure 22. Spatiotemporal profiles of high-resolution spike waveforms of sorted single units. *(a) Left: schematic of the recording site layout. Middle left: Mean spike waveforms of a cortical neuron with a narrow spike (putative interneuron) on all channels. Middle right: Color map showing the spatiotemporal profile of the spike waveform on channels (n = 32) framed by the blue rectangle in the middle left (column of sites which contain the peak waveform channel). The inset at the top demonstrates magnified mean spike waveforms on nine adjacent channels which recorded the spikes with the largest amplitudes. Right: Color maps illustrating the two dimensional spatial profiles of the spike waveform on all channels (red rectangle in the middle left) at multiple time points (time step, 0.1 ms). Time zero corresponds to the trough (negative peak) of the spike waveform. (b) The spatiotemporal profile of the spike waveform of a neuron with a wide spike (putative principal cell). Note the*

longer duration and the dorsal propagation of the spike in the color maps (time step on the right, 0.2 ms). (c) Additional examples (n = 15) of extracellular spike waveforms of various single units. For each pair of color map, the left (with a blue frame) shows the spatiotemporal pattern of the spike waveform at the column of sites comprising the peak waveform channel. The right color map (with a red frame) illustrates the two-dimensional potential profile of the spike waveform measured at the trough of the waveform. The examples are ordered by the vertical position of their spike waveform on the array. For illustration purposes, only units with their spike waveform located in the center of the array are shown.

The *firing rate*, measured in Hz, indicates the quantity of spikes discharged per second.

The *burst index*, as defined by Mizuseki and colleagues(249), is a metric that quantifies the proportion of spikes that occur in bursts. A spike is considered part of a burst if the interspike interval to an adjacent spike is less than 6 milliseconds.

The *trough-to-peak amplitude*, expressed in microvolts (μV), represents the absolute amplitude difference between the lowest point (trough) and the highest point (peak) of the average spike waveform, calculated from the bandpass-filtered data on the channel with the highest spike amplitude (peak waveform channel; also illustrated in Fig. 23E).

The *trough-to-peak time*, also known as spike duration and measured in milliseconds (ms), is the time interval between the trough and the following peak of the average spike waveform (filtered).
The difference in time between the trough and the subsequent peak of the filtered mean spike waveform is known as the trough-to-peak time (also called spike duration; measured in milliseconds). The peak waveform channel is where the spike duration is measured (see also Fig. 23F).

The *AB-ratio*, indicative of waveform asymmetry, is calculated as the ratio of the two positive peaks on the filtered spike waveform at the peak waveform channel, as outlined in the CellExplorer software (250). This is also depicted in Figure 23I.

The dense sampling of spike waveforms yields high spatial resolution, which may provide additional valuable information to characterize neurons further. We thus extracted the following multichannel waveform features (computed from the filtered recordings) for each unit from the mean spike waveforms.

The *relative one-dimensional spike waveform spread*, measured in micrometers, describes the range of channels where the spike waveform's trough-to-peak amplitude surpasses 20% of the peak amplitude. For this calculation, only recording sites situated in the same column as the peak waveform channel were considered, as illustrated in the inset of Figure 23J, which shows the average spike waveform spread derived from the spike waveforms of all single units. Although we used a higher threshold of 20% rather than 12%, our calculation techniques were similar to those reported in the study by Jia and colleagues(251). By using the more conservative threshold, we hoped to prevent overestimating the waveform spread in specific situations, such as when there was high background activity on multiple channels due to highly synchronized cortical activity, which could have an impact on the mean multichannel spike waveform, or when the mean spike waveforms' signal-to-noise ratio was lower because of low spike counts or low amplitudes.

The *absolute one-dimensional spike waveform spread* (in μm), uses a fixed threshold of 20 μV, similar to the method described above.

The *relative two-dimensional spike waveform spread* is defined as the count of channels where the trough-to-peak amplitude of the spike waveform exceeds 20% of the peak channel's amplitude, with all channels included in the calculation.

The *absolute two-dimensional spike waveform spread* is calculated similarly to the above method but applies a fixed threshold of 20 μV.

The spike waveform of individual units typically had a larger negative peak at the trough than positive peaks. A small number of single units (~1%) did, however, have a positive peak that was significantly larger than their trough. These units were recognized and labeled in the dataset (positive spikes), and they may represent putative axonal spikes (252, 253).

4.8 Quality metrics.

To describe the quality of the selected single units, several quality metrics were calculated and provided with the dataset, along with the properties of single units described above. Quality metrics were computed using the SpikeMetrics module of the SpikeInterface open-source Python framework (254). Most of these metrics are based on the code developed at the Allen Institute for Brain Science (255). The complete list and detailed description of the quality metrics can be found on the GitHub page of these software (listed also in the Code Availability section) and in the documentation of the Allen Software Development Kit (https://allensdk.readthedocs.io/en/latest/_static/examples/nb/ecephys_quality_metrics.html), here we provide only a short description. Distributions of some of these metrics are presented in Fig. 24.

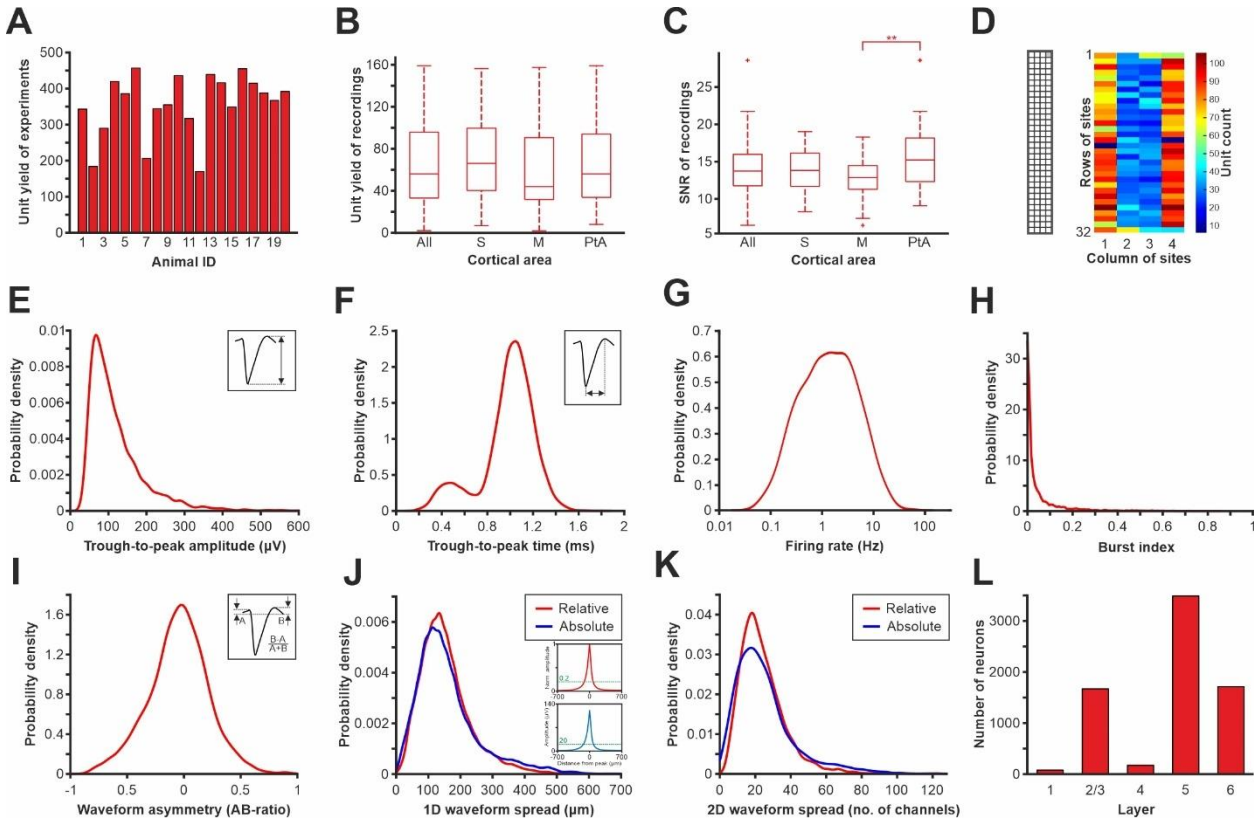

Figure 23. Results of spike sorting and distributions of single unit properties*. (a) Unit yield of each experiment (n = 20 rats). (b) Boxplots showing the distribution of unit yields of recordings (n = 109), also broken down by cortical areas (S, somatosensory; M, motor; PtA, parietal association cortex). (c) Boxplots illustrating the distribution of the signal-to-noise ratio (SNR) of recordings estimated by averaging the SNR of single units found in the recordings. **p < 0.01 (one-way ANOVA with Tukey's honestly significant difference post hoc test). (d) Distribution of all single units (n = 7126) based on their soma location (corresponding to the peak waveform channel) plotted according to the recording site layout (on the left). Sites 64 and 65 were shorted (sites with dark blue color in the middle of columns 1 and 4). (e–k) Probability density functions showing the distribution of single unit properties. (e) The distribution of trough-to-peak amplitudes of all single units. The inset shows the calculation method of this property (see also the Methods section for more details). (f) Distribution of the trough-to-peak times of all units. This property was defined as the time period between the trough and the subsequent positive peak of the spike waveform (inset). (g) Distribution of firing rates. Note that the x-axis is on a logarithmic scale. (h) Distribution*

of burst index values. (i) Distribution of AB-ratios showing the spike waveform asymmetry. The inset shows the calculation method of the AB-ratio. (j) Distribution of one-dimensional (vertical) relative (red) and absolute (blue) spike waveform spreads of single units. The insets show the average spread of the spike waveforms calculated from normalized (top) and absolute (down) spike amplitudes of all units. The threshold level used to compute the vertical spike waveform spreads are indicated with green dashed lines in the insets. (k) Distribution of two-dimensional relative (red) and absolute (blue) spike waveform spreads calculated using the same thresholds as applied for the computation of the vertical spike waveform spreads in panel j. (l) Laminar distribution of sorted cortical single units.

Presence ratio. Fraction of the recording in which spikes of the unit are present (range, 0–1).

Amplitude cutoff. Estimate of the rate of missed spikes (false negative rate) based on the amplitude histogram of spikes (range, 0–0.5).

ISI violations. Rate showing refractory-period violations based on the work of Hill et al.(256). Lower values indicate less contamination from the spikes of other single units.

Isolation distance. The calculation of this metric is based on the principal components of the spike waveforms and the Mahalanobis distance between spikes (257, 258). It shows the degree of separation of a unit cluster compared to other clusters. A higher value reflects a better isolation.

L-ratio. The Mahalanobis distance and chi-squared inverse cumulative distribution function (given the assumption that the spikes in the cluster distribute normally in each dimension) are used to find the probability of cluster membership for each spike (258, 259). Lower values indicate units with better quality.

d'. The classification accuracy between single units based on linear discriminant analysis (256). This feature is also computed in the principal component space.

Nearest-neighbors hit rate and miss rate. Non-parametric estimate of unit contamination using nearest-neighbor classification (260).

Silhouette score. A standard metric for quantifying cluster overlap (261).

Maximum drift. Maximum change (in μm) in the position of the spike waveform throughout the recording. This feature can be used to identify recordings with a high amount of probe motion relative to the brain tissue (255).

Cumulative drift. Cumulative change (in μm) in position of the spike waveform throughout the recording(254).

Signal-to-noise ratio (*SNR)*. Ratio of the spike amplitude and the noise in the recording. The noise level was estimated using the median absolute deviation (MAD) formula implemented in SpikeMetrics.

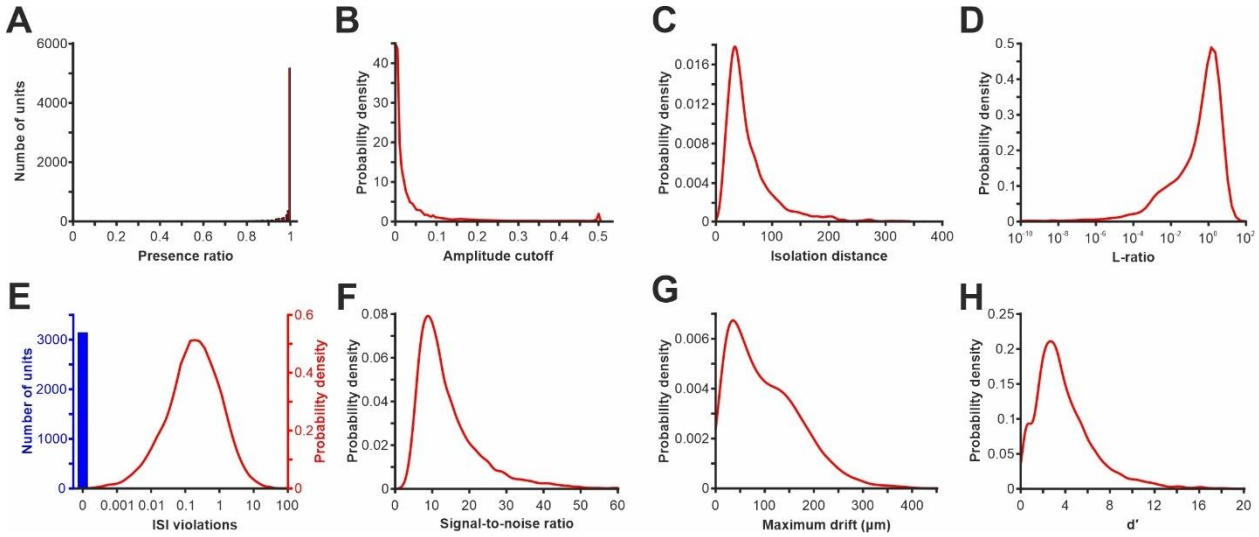

Figure 24. Quality assessment of the spike sorting based on various quality metrics. *(a) Histogram showing the distribution of the presence ratios. (b–h) Probability density*

functions illustrating the distributions of quality metrics. Distribution of (b) amplitude cutoffs, (c) isolation distances, (d) L-ratios (note that the x-axis is plotted on a logarithmic scale), (e) interspike interval (ISI) violations (note that because a large fraction of units has an ISI violation of zero, these zero values are demonstrated as a single column (in blue); the height of the column is not proportional to the distribution of other ISI values), (f) signal-to-noise ratios, (g) maximum drifts, and (h) d' of all single units.

4.9 Laminar localization of recording sites and single units.

For each single unit, we determined the cortical layer where the soma of the neuron was located. We considered the peak waveform channel (i.e., the channel where the amplitude of the spike waveform of the particular unit was the largest) as the soma position of a particular neuron. This is usually a good estimate of the real position of the cell body of neurons (262). Then, cortical layer boundaries and laminar positions of recording sites were estimated based on the Nissl-stained brain sections and various electrophysiological features were extracted from the cortical local field potentials (LFP; 0.1–300 Hz) and multi-unit activity (MUA; 300–5000 Hz). Using data from all channels, we created LFP and MUA depth profiles of the cortical slow-wave activity (SWA) from short (few second long) segments of continuous traces (see examples in Fig. B). Furthermore, in recordings where a sufficient level of MUA could be recorded, we detected the onset of active phases (phases showing high spiking activity, also called up-states) of the SWA using a MUA-based state detection algorithm developed in one of our previous studies (263). Then, we computed the average LFP and MUA depth profiles of these active phases. Combining the anatomical landmarks obtained from the histology with the features extracted from the cortical activity during SWA(236), we could identify the laminar location of single units with a relatively high reliability. However, some uncertainty may remain in the case of units located near the border of layers or, due to slight brain dimpling, in the case of units located in superficial layers. The laminar location of units and recording sites is also provided in the dataset.

4.10 Data records

The dataset and corresponding metadata are publicly available via the G-Node Infrastructure (GIN, https:// gin.g-node.org/) provided by the German Neuroinformatics Node of the International Neuroinformatics Coordination Facility (https://gin.g-node.org/UlbertLab/High_Resolution_Cortical_Spikes)(264). Each recording and corresponding metadata, single unit properties and quality metrics were packaged in the Neurodata Without Borders: Neurophysiology version 2.0 (NWB:N 2.0) data format(227) with custom MATLAB scripts using the MatNWB application programming interface (API). A single NWB file was created from each recording (n = 109). NWB files were placed in the appropriate folder based on the identifier of the animal (from Rat01 to Rat20), insertion sequence (Insertion1 or Insertion2) and cortical depth (from Depth1 to Depth3). The filename of the NWB file (identifier) was constructed by concatenating the above information (e.g., Rat01_Insertion2_Depth3).

The NWB file, which, in terms of storage, is based on the Hierarchical Data Format (HDF5), contains several main groups which are similar to directories. The acquisition group contains the continuous wideband 128-channel data (‘wideband_multichannel_recording’) in a compressed form, as well as several parameters related to the raw data such as the measurement unit or the data conversion number. The general group contains metadata about the experiments and consists of several subgroups, related to the recording probe (‘general/devices’; ‘general/extracellular_ephys’) or the subjects of the experiments (‘general/subject’). Former subgroups carry information about the probe location (brain area and stereotaxic coordinates) and the relative positions and laminar location of recordings sites, while the latter contains metadata about the animal (e.g., sex, species, subject ID, or weight). Information about spike sorting and single units and corresponding data are available in the units group. For each unit, we included here the mean and standard deviation of their spike waveform on all channels, calculated both from the filtered (‘mean_waveform_all_channels_filt’; ‘waveform_sd_all_channels_filt’) and the wideband data (‘mean_waveform_all_channels_raw’; ‘waveform_sd_all_channels_raw’). For an easier visualization of the spike waveform in two dimensions, we have also added an array which contains the mean spike waveform in the 32 × 4 shape of the array

(‘mean_waveform_all_channels_filt_32 × 4’; ‘mean_waveform_all_ channels_raw_32 × 4’). Furthermore, the spike waveform recorded on the channel with the largest spike (i.e., peak waveform channel) was saved separately (‘mean_waveform_peak_channel_filt’, ‘mean_waveform_peak_ channel_raw’). All single unit properties and cluster quality metrics described in the Methods section, as well as the spike times and spike count of each unit were saved in the units group. However, if needed, potential future users can use the provided wideband recordings to redo the spike sorting either by applying different parameters in Kilosort2 or using other spike sorting algorithms. Furthermore, to aid users in selecting and analyzing a subset of this dataset appropriate for their research goals, we also created an NWB file (‘allSingleUnits.nwb’) which contains all single units with all the properties listed above, along with the identifier of the recording (‘units/ session_id’) and the cortical area (‘units/cortical_area’) they originate from. Besides the NWB files, two CSV files are included in the dataset. The first (‘Animal_characteristics_and_targeted_ cortical_areas’) contains the information shown in Table 3, while the second CSV file (‘Recording_characteristics’) lists several useful properties for each NWB file including the file size, the duration of the recording, the cortical area, the single unit yield, the average signal-to-noise ratio of single units, the degree of power line (50 Hz) noise contamination, as well as the RMS noise and RMS signal levels.

Table 3. *Animal characteristics, targeted cortical areas and corresponding stereotaxic coordinates. CoA, Cortical Area; I1, frst insertion site; I2, second insertion site; M1, primary motor cortex; M2 secondary motor cortex; PtA, parietal association cortex; S1HL, hindlimb* region of the primary somatosensory cortex; S1Tr, trunk region of the primary somatosensory cortex; AP, anterior-posterior; ML, medial-lateral.

Animal ID	Weight (g)	Sex	CoA (I1)	AP (I1)	ML (I1)	CoA (I2)	AP (I2)	ML (I3)
Rat01	320	F	S1HL	-2.28	2.44	M1	-1.92	1.39
Rat02	300	F	PtA	-3.12	2.41	M2	-3.24	1.57
Rat03	340	F	S1HL	-1.95	2.44	M1	-1.95	1.87
Rat04	390	F	PtA	-3.6	2.5	S1Tr	-2.4	2.4
Rat05	390	M	PtA	-3.25	2.36	PtA	-3.5	1.45
Rat06	400	M	S1Tr	-2.75	1.99	M1	-2.7	1.6
Rat07	320	M	S1HL	-2.16	2.63	-	-	-
Rat08	320	F	PtA	-3.48	2.96	PtA	-3.36	2.0
Rat09	200	F	M1	-3.12	2.14	M2	-3.12	1.66
Rat10	280	F	PtA	-3.24	2.04	M2	-3.24	1.5
Rat11	240	F	PtA	-3.48	2.32	PtA	-3.48	1.8
Rat12	310	M	S1Tr	-2.5	2.49	M1	-2.5	1.76
Rat13	390	M	S1Tr	-2.64	2.35	M1	-2.64	1.59
Rat14	260	F	S1Tr	-2.8	2.1	M1	-2.9	1.85
Rat15	270	M	PtA	-3.4	2.28	PtA	-3.4	1.31
Rat16	280	F	S1Tr	-2.5	2.68	M1	-2.6	1.66
Rat17	390	M	S1Tr	-2.7	2.49	M1	-2.9	1.97
Rat18	380	M	S1HL	-2.35	1.95	M1	-2.35	1.52

Rat19	290	M	S1Tr	-2.9	2.67	M1	-2.9	1.85
Rat20	240	F	PtA	-3.2	2.25	M1	-3.0	1.71

Table 4. *Single unit yield statistics (average±standard deviation) calculated for brain regions, insertions and recordings*.

	All	S	M	PtA
Total unit yield	7126	2518	2362	2249
Average unit yield per animal	356.45±86.06	-	-	-
Number of penetrations	39	12	15	12
Average unit yield per penetration	182.79±65.13	209.83±56.57	157.47±59.19	187.42±72.79
Number of recordings	109	35	41	33
Average unit yield per recording	65.40±40.98	71.94±40.71	57.61±39.17	68.15±43.11

4.11 Technical validation of cortical activity data

The cortical dataset (n = 109 recordings; ~0.9 TB overall size) was collected using a single-shank silicon-based multielectrode providing dense sampling of brain electrical activity (Fig. 19A). Rats were anesthetized with ketamine/ xylazine cocktail which is known to induce slow-wave activity (SWA) in the thalamocortical system of rodents (Fig. 19B, C)(11, 139, 236, 248). During SWA, the neocortex shows characteristic patterns of electrical activity, for example, alternating phases of high and low spiking activity (Fig. 19C). The peak frequency of the ketamine/ xylazine-induced SWA is usually between 1 and 2 Hz in rats (236, 265) (Fig. 19D). In our dataset, we measured an average peak frequency of 1.29 ± 0.44 Hz suggesting an ordinary appearance of SWA (Fig. 19E). The fluorescent marks left in the brain

tissue by the dye painted on the probe were used to identify the cortical recording location, that is, the tracks caused by the two probe insertions in the cortex (Fig. 19F). After we have found the brain sections containing these fluorescent marks, anatomical features provided by Nissl-staining were used to identify the boundaries of cortical layers and to determine the laminar location of recording sites (Fig. 19F). To sample data from all layers, cortical electrical activity was recorded in most cases from two to three depths (depending on the thickness of the cortex; Fig. 20). The laminar position of the soma of single units was estimated using the combination of anatomical (e.g., layer borders) and electrophysiological features (local field potential and multi-unit activity depth profiles (236); Fig. 20). Estimated noise and signal levels of the cortical recordings are shown in Fig. 21 (see the Methods section on the detailed procedures of noise and signal level calculation). The quality of most of the recordings was high, with high signal (spiking activity) and low noise levels. Only a few measurements (~10) were contaminated with higher levels of noise.

Single-unit activity was extracted from the continuous wideband data using spike sorting, then various spatial and temporal features of the single units were calculated to characterize our dataset and to assess its quality (Figs. 21–23). The neocortex is composed of two main neuron types, inhibitory (GABAergic) interneurons and excitatory principal cells. These two neuron classes can be discriminated based on the durations of their extracellular action potentials: interneurons generate usually narrow spikes, while most principal cell fire wide spikes (265). To demonstrate example cortical single units from our dataset, in Fig. 22 we show the high-resolution spike waveforms of a neuron with a narrow spike (Fig. 22A), a putative principal cell firing wide spikes (Fig. 22B), as well as a small collection of units with various spike waveforms (Fig. 22C). The spike waveform of the putative principal cell shows also a propagating pattern indicating the backpropagation of the action potential from the soma to the apical dendritic tree (Fig. 22B). This feature is characteristic of pyramidal cells and was observed in previous studies (251, 266).

In total, we sorted more than 7000 single units, with around 2300 units from each of the three main cortical areas (Table 4). On average, about 350 neurons could be sorted from the data obtained in a single rat (Fig. 23A; Table 4) and 180 units from a single penetration (Table 4).

From a single recording acquired at a particular cortical depth, we could extract around 65 neurons on average (range: 2–159) and there was no statistically significant difference in the unit yield between the three cortical areas (one-way ANOVA, $F(2, 108) = 1.27$, $p = 0.286$; Fig. 23B; Table 4). The quality of recordings was also estimated by averaging the SNR of neurons sorted from these recordings (Fig. 23C). Interestingly, we found a statistically significant difference between the SNR values of cortical areas the quality of data acquired from the parietal association cortex was significantly better than the quality of motor cortical recordings ($p = 0.0022$). The cause behind this difference in quality is most likely the sequence of probe insertion. We have found a significant difference in the RMS signal levels (Wilcoxon Rank Sum Test; $p = 0.00034$) and also in the SNR values (two-sample t-test; $p = 0.0066$) between recordings obtained after the first and the second probe insertion. Both RMS signal levels (mean ± SD: 13.56 ± 5.23 μVRMS vs. 10.41 ± 4.23 μVRMS) and SNR values (14.79 ± 3.22 vs. 12.98 ± 3.54) were significantly higher after the first insertion compared to the second probe penetration. Furthermore, more single units were sorted from the data obtained after the first insertion (4377 units vs. 2749 units) and the amplitudes of these units also were significantly higher (Wilcoxon Rank Sum Test, $p = 3.51 \times 10{-}30$; mean ± SD: 128.07 ± 85.84 μV vs. 108.82 ± 68.76 μV). Recordings from the motor cortex were obtained in more cases after inserting the probes the second time ($n = 14$; 70% of the second insertions) compared to data acquired from the parietal association and somatosensory cortices ($n = 4$ and $n = 1$ second insertions, respectively). We also calculated the distribution of single units at the recording sites of the array by assigning each unit to the site corresponding to its peak waveform channel (Fig. 23D). Here we can see that most units were detected near sites located closer to the edge of the silicon shank. The reason behind this, about twofold difference is that besides neurons located in front of edge sites, cells located next to edge sites (in the cortical tissue next to the probe shank) were assigned to these sites, while only those neurons which are in front of center sites were assigned to center sites.

We also computed several spatial and temporal attributes of the mean spike waveform, as well as properties related to the firing patterns of single units (Fig. 23E–K). The mean amplitude of the spike waveforms calculated from the filtered (300–6000 Hz) recordings was 120.64 ± 80.23 μV (Fig. 23E), while the spike durations showed the typical bimodal

distribution (Hartigan's dip test; $p = 0.023$) characteristic of the neocortex with shorter durations corresponding to putative interneurons and longer durations to putative principal cells (Fig. 23F). The firing rate of units showed a lognormal distribution, as described previously (Fig. 23G)(267). High-resolution recordings also allow to examine the spatial spread of the spike waveforms. On average, the vertical spread of spike waveforms was about 160 μm (Fig. 22J), while, considering the whole, two-dimensional array, spike waveforms could be recorded with around 25 recording sites simultaneously (Fig. 23K). Based on the laminar location of the single units, almost half of the recorded neurons were located in layer 5, while around the quarter of all neurons originated from layer 2/3 and another quarter from layer 6 (Fig. 23I). Only a small fraction of units were located in layers 1 and 4. This is in agreement with the findings of previous studies showing that in the neocortex the strongest activity during SWA can be recorded in layer 5, while the unit activity decreases both above and below this layer (139, 236, 268).

Finally, we provide here the results of several spike sorting quality metrics (Fig. 24). The distribution of the values of most of these metrics was similar to metrics calculated from a large dataset of single units collected in a recent study with Neuropixels probes from mice (255). We also support their approach for single unit inclusion described in the study, that is, keeping all units with an appropriate quality and then, based on the calculated quality metrics as well as on spike waveform properties demonstrated above, future users can filter the collection of single units and select a subset of these based on their research goals. At the time of writing, the ARP data repository of the HUN-REN network reported 863 downloads of this dataset, which includes data related to the thalamic study.

5 Discussion

In neuroscience, freely available cortical recordings from high-density probes are still an exception, but especially from subcortical structures. High-density probe acquisitions offer a spatial and temporal resolution leap that gives a much more detailed understanding of neural processes and dynamics. The most significant advantage of databases of cortical or subcortical high-density recordings is that they can provide a wide range of ways to help understand the activity of particular structures at the nuclei or neuronal level. Together with the spike-sorted single units and the various associated metrics, it can help with neuronal classification, delineate layers or nuclei, and improve understanding of how the brain works in different states, such as sleep or anesthesia. Beyond understanding specific structures, it can also aid comprehension of the mechanisms of complex neural circuits such as the thalamocortical network.

The spike sorting results and various single-unit-related properties (e.g., firing rate, burst index, spike waveform characteristics) allowed us to classify and characterize neurons in more detail. However, it should be noted that any anesthetic influences brain activity and does not fully reflect the activity that occurs in natural sleep. Furthermore, micro-movements can cause artifacts and discrepancies in the processed data, and we attempted to mitigate these influences.

Spike-sorting algorithms and manual curation may impact the accuracy and reliability of the results despite efforts made to ensure accuracy and reliability. Technical limitations and human factors are always present in this type of analysis. While every reasonable step has been taken to minimize their influence, it is possible that some degree of error may still be present.

This thesis provides the first evidence that spontaneous population activity patterns propagate in the rodent thalamus *in vivo* during anesthesia and slow-wave sleep. Furthermore, findings indicate that neurons within higher-order thalamic nuclei in the dorsal region are most likely to show propagating activity. During up-states, activity tends to travel along the dorsoventral axis, with a preference for the ventral to dorsal direction. The thalamus generally showed

various spatiotemporal activity patterns during natural sleep and anesthesia. However, neuronal activity in the thalamus of anesthetized animals was more streamlined and homogeneous. For example, we noticed that most of the up-states during anesthesia propagated from the ventral to the dorsal area with slight variation in their trajectories, as shown in Figure 5. In natural sleep, ventral-to-dorsal propagation occurred less frequently, and the spread of multiunit activity (MUA) was faster than the propagation of thalamic activity observed under anesthesia, as shown in Figure 10. Furthermore, cortical population activity induced by ketamine/xylazine anesthesia, recorded using multi-shank silicon probes, consistently showed stereotypical propagation patterns where many cortical up-states began at the anterior shanks and then moved posteriorly, as illustrated in Figures 6 and 7. The portion of cortical up-states that propagated from anterior to posterior was about the same as the portion of thalamic up-states that predominantly propagated from ventral to dorsal (~50% of up-states), while the ratios of other propagation patterns were significantly lower (3-10%; Fig. 15A and B). These findings support the recent theory, suggesting that the closely coupled neocortex and thalamus operate together as a unified slow-wave generating system (269). However, the ventral-to-dorsal propagation of thalamic activity was more prominent in thalamic multiunit activity (MUA) depth profiles locked with cortical up-states compared to those associated with thalamic up-states (Fig. 14 vs. Fig. 13). This suggests that the neocortex may significantly influence the shaping of population activity in the thalamus.

Since its discovery, several characteristics of slow-wave propagation have been reported in human and animal models. Numerous studies using high-density EEG recordings in humans have confirmed that individual spontaneous slow-waves occurring during NREM sleep can originate from any part of the cortex and typically travel along the anterior-posterior axis with distinct trajectories (7, 178, 206). Although global slow-waves can originate from within the cortex, they tend to originate primarily in the insula or cingulate gyrus. Subsequently, they propagate in an anterior-posterior direction, terminating in cortical regions of the parietal or occipital regions (7, 178). The average speed of spontaneous slow-waves in humans is 2.2 m/s, and their propagation delays range from 40 to 360 ms (7, 178).

Hangya and colleagues published a study using ECoG recordings to look into the spatiotemporal dynamics of slow-wave propagation at a finer spatial scale of about 1 cm (181). Found that mesoscale slow-waves have sophisticated spatiotemporal dynamics compared to macroscale slow-waves collected with EEG recordings. These mesoscale slow-waves show different propagation patterns, such as convergence, divergence, or circular patterns (181).

Many experimental approaches have been used to study the propagation of spontaneous cortical slow-waves in rodents. These techniques include voltage-sensitive dye imaging, two-photon and wide-field calcium imaging, and multi-electrode and micro-ECoG recordings (135, 180, 184, 194-196, 199-201, 203, 204, 270, 271). These *in vivo* studies have investigated slow-wave properties in naturally sleeping and anesthetized animals. In the anesthetized models, a range of anesthetics have been used to evoke slow-waves, including urethane, ketamine/xylazine, isoflurane and chloral hydrate. In rats, just like humans, spontaneous global slow-waves in the neocortex tend to propagate along the anterior-posterior axis, both during anesthesia (196, 200) and NREM sleep (271). However, slow-waves studied in localized cortical areas could show different propagation patterns (e.g., propagation along the medial-lateral axis in the visual cortex; (272)) or showed no preferred direction of propagation (135, 194, 199). In mice, similar to rats and humans, the majority of studies have observed that cortical slow-waves tend to travel along the anterior-to-posterior axis (180, 184, 186, 188, 192, 195, 197, 201, 203, 204), predominantly propagating in the anterior-to-posterior direction (184, 186, 195, 201, 202, 204). However, research has shown that there is slow-wave propagation along the medial-lateral axis in the mouse visual cortex (203).

In rodents, the *in vivo* cortical slow-waves spread significantly slower than in humans, with speeds between 10 to 100 mm/s (180, 183, 184, 187, 194-196, 200, 203, 204, 272, 273). Additionally, the propagation of cortical population activity was slightly slower *in vitro* (5-10 mm/s; (136, 274)). Our results concerning the propagation of cortical slow-waves align well with the earlier findings. We observed that, even in a small cortical area (~ 1.5 mm), up-states tended to move from the anterior to the posterior direction at speed (~ 38 mm/s)

consistent with the speeds reported in previous research. Interestingly, the study conducted by Reyes-Puerta and colleagues, which involved examining slow-waves in urethane-anesthetized rats through voltage-sensitive dye imaging and silicon probe recordings in cortical areas of similar extent (~1.5 mm), revealed a spatiotemporal pattern of cortical up-state propagation that closely resembled our findings (see comparison between Fig. 15C and D, and Fig. 15E and F in (194)). They discovered that the average propagation speed of spontaneous cortical slow-waves is approximately 35 mm/s, which is very similar to the average speed observed in our cortical recordings.

Fewer studies have investigated the spatiotemporal dynamics of slow-waves under the cortex. In rats anesthetized with chloral hydrate, Ushimaru, and colleagues found that neurons in ventral anterior and ventromedial (VA/VM) thalamic nuclei, as well as in the reticular thalamic (Rt) nucleus, fire notably earlier (approximately at the start of up-states) compared to neurons located in the VL nucleus and layer 5 of the frontal cortex (207). Furthermore, in ketamine/xylazine-anesthetized rats, Slezia and colleagues found that thalamocortical neurons located in different thalamic nuclei (VPM, VPL and Po) fire at distinct phases of up-states (205). For instance, population activity in the Po preceded firing in VPM/VPL nuclei with a time lag of about 100 ms. Our findings are consistent with the delay observed in these nuclei. In our thalamic recordings, population activity in the ventral parts of the Po started on average several tens of milliseconds earlier than MUA in the VPM (see Fig. 14). The leading role of Po in up-state generation is further supported by the study of Sheroziya and Timofeev (204), where they found that in ketamine/xylazine anesthetized mice, the Po was among the first structures to fire during up-states, along with frontal and motor cortices, and the parafascicular (PF) thalamic nucleus. Thalamocortical structures with the latest activity were the posterior cortex and the anteroventral (AV) thalamic nucleus. In our simultaneous cortical and thalamic recordings, in both rats and mice, we observed that MUA in ventral parts of the Po tended to start before population activity during cortical up-states and also preceded MUA in adjacent thalamic nuclei (see Figs. 6 and 8).

Interestingly, a human study using EEG and depth electrode recordings found only short-time lags between spontaneous cortical and thalamic slow-waves in pharmacoresistant

epileptic patients (206). Thalamic slow-waves started nearly simultaneously in all examined thalamic nuclei (i.e., the anterior thalamus, mediodorsal, and ventral anterior nuclei) shortly after cortical slow-waves. While methods based on field potentials might be less precise in determining propagation patterns of smaller neuronal populations compared to MUA-based methods, the study suggests that similar to rodents, the propagation of slow-waves does not occur in every region of the thalamus.

What could potentially explain the observed preference for ventral-to-dorsal propagation in the thalamus? Most of the dorsal thalamic nuclei investigated in this study (e.g., Po, LD, or LP nuclei) are classified as higher-order nuclei that receive abundant input connections from pyramidal cells located in layer 5 of the neocortex (24). For example, in the Po, thalamocortical neurons are strongly innervated by giant excitatory terminals originating in layer 5 of the somatosensory cortex (275-277). A multitude of *in vivo* and *in vitro* animal studies revealed the pivotal role of neurons located in cortical layer 5 in the initiation and propagation dynamics of cortical up-states (136, 139, 140, 195, 236, 278, 279). Furthermore, it is well established that sensory cortices, such as the primary somatosensory or visual cortex, exhibit topographical organization. Since the Po primarily receives its inputs from the somatosensory cortex, whereas the more dorsally located LP nucleus is interconnected with visual cortical areas, and considering the anterior positioning of the somatosensory cortex relative to the visual cortex, it is reasonable to predict that, during up-states traveling from anterior to posterior cortical areas, MUA induced by the firing of cortical layer 5 pyramidal cells in the Po would precede neuronal activity in the LP, as was also observed in our data. Thus, we speculate that MUA propagation occurring in the thalamus is primarily a consequence of the horizontal propagation of cortical slow-waves. In this scenario, thalamocortical neurons are sequentially activated via the intense firing of layer 5 pyramidal cells. Consequently, the anterior-to-posterior cortical slow-wave propagation would translate to a ventral-to-dorsal propagation in the thalamus.

The above theory is supported by our observation that up-states displaying cortical anterior-to-posterior propagation were detected in comparable proportions to thalamic up-states with ventral-to-dorsal propagation (see Fig. 15). In addition, cortical up-states traveling in the

opposite direction (posterior-to-anterior) were frequently observed with dorsal-to-ventral thalamic propagation (Fig. 15), providing further support for our hypothesis. Furthermore, if cortical up-state propagation is relayed to higher-order nuclei via layer 5 pyramidal cells, this would partially explain the gradual propagation observed between Po and LP nuclei (e.g., Fig. 18), since somatosensory and visual cortical areas are practically adjacent to each other. For instance, an up-state traversing the somatotopic map of the somatosensory cortex towards the adjacent visual cortex through horizontal cortico-cortical connections would reach the visual cortex with minimal delay and continue its course across the retinotopic map. If layer 5 cortical inputs are topographically organized within these nuclei, this cortical propagation would appear in the thalamus as a relatively smooth MUA propagation both within and between Po and LP, aligning with our observations in thalamic recordings. Finally, the observed ~100 ms delay between the up-state initiation and the termination of MUA propagation in the dorsal thalamus closely mirrors the ~100 ms time lag of slow-waves found between the frontal and posterior areas of the neocortex (195). The similarity in time lags between the cortex and the thalamus implies that the propagation speed of cortical slow-waves must be higher than that of thalamic slow-waves, given that up-states have to travel greater distances across the cortical mantle than thalamic up-states between thalamic nuclei. In agreement with this assumption, in our thalamocortical recordings, we observed a more than three times faster propagation of cortical up-states compared to propagation of thalamic up-states.

In several of our thalamic recordings, we noticed that population activity in adjacent higher-order thalamic nuclei (e.g., Po and LD) may decouple, that is, the gradual MUA propagation between these areas was absent, and MUA propagated separately within each nucleus, or no MUA propagation was observed at all. This decoupling phenomenon was more frequent under lighter anesthesia or during slow-wave sleep. As observed in prior studies, these states are characterized by increased variability and complexity in cortical propagation patterns (180, 182). These studies demonstrated that lighter anesthesia leads to an increased spatiotemporal complexity of cortical activity, manifesting in a higher number of distinct propagation patterns/modes (exhibiting more diverse spatiotemporal patterns) and an increased propagation speed compared to deeper levels of anesthesia (180, 182). Similar

results were found for the transition from anesthetized states to wakefulness (280). In our study, we also observed an increase in the number of distinct thalamic MUA patterns and in the speed of MUA propagation between light anesthesia and slow-wave sleep (Fig. 18).

While our observations provide strong evidence for the occurrence of spontaneous activity propagation in the rodent thalamus, it is important to discuss the limitations of our study. First, despite our efforts to comprehensively explore the activity of the thalamus, not all thalamic nuclei were investigated here. For example, we did not record the activity of midline and intralaminar thalamic nuclei, due to their complicated access with silicon probes, irregular geometries, and smaller volumes relative to the nuclei we examined. These factors would complicate the targeting and identification of these nuclei, and thus the reliable detection of MUA propagation. However, we can not rule out the possibility that propagation of thalamic population activity might also occur in these nuclei. Second, we did not perform spike sorting and single-unit activity analysis in this study. Nevertheless, we would not expect any qualitative change in our results by analyzing single-unit activity instead of MUA, since propagation of thalamic up-states could be reliably identified based on the population activity alone. However, an in-depth analysis of thalamic activity on a single unit level could yield deeper insights into the properties of thalamic propagation patterns in future investigations. Third, cortical population activity was obtained only from a local cortical area (~1.5 mm along the anterior-posterior axis) which limits our field of view to observe cortical up-state propagation. Extending our observation by involving a larger cortical area (e.g., by implanting multiple silicon probes into the cortex), would enable a more comprehensive examination of the interplay between cortical and thalamic population activity. Finally, in some of our thalamic recordings from anesthetized rats we noticed that neuronal activity patterns might change over time (suddenly or over longer time periods), transitioning from exhibiting MUA propagation (indicating a state with higher neuronal synchronization) to displaying no propagation in the same thalamic nuclei (reflecting a less synchronized state), and vice versa. This implies that the actual brain state (e.g., the depth of anesthesia) could also have a strong impact on ongoing thalamic activity patterns, and that MUA propagation might occur even in more thalamic nuclei than actually observed, since a consistent depth of ketamine/xylazine anesthesia is challenging to maintain.

6 Conclusions

The findings of the thalamocortical study demonstrate that spontaneous population activity within the dorsal thalamus shows propagating patterns in vivo during both anesthesia and slow-wave sleep. Furthermore, our findings indicate that during up-states, the activity tends to propagate along the dorsoventral axis, with a greater prevalence in the ventral-dorsal direction. This ventral-dorsal propagation was observed during natural sleep, although multiunit activity (MUA) propagation occurred faster and less frequently than in anesthetized animals. The results on the direction and speed of cortical propagation waves (~38 mm/s) were consistent with previous findings in the literature, which indicated a predominant anterior-posterior propagation of up-starts. In a subset of thalamic recordings, it was observed that the propagating population activity in adjacent high-order thalamic nuclei (e.g., Po or LD) was separable. MUA propagation within each nucleus was confined or completely lacking a propagation pattern. The explanation for this phenomenon is likely in the number and propagation speed of more complex thalamic MUA patterns that appear in light anesthesia or slow-wave natural sleep.

7 Summary,Összefoglaló

Recent studies have shown that slow-waves (SWs), prominent during anesthesia and deep sleep, shows complex dynamics and propagate across neocortical areas. However, it is unclear if similar propagation occurs within the thalamus. This dissertation explores the propagation of population activity within the thalamus of ketamine/xylazine-anesthetized rats and mice, using high-density silicon probes. Propagating activity is predominantly detected in dorsal thalamic nuclei, including the posterior (Po), lateral posterior (LP), and laterodorsal (LD) nuclei. Activity most of the time propagate along the dorsoventral axis, with over half of the upstates showing ventral-to-dorsal propagation. Simultaneous recordings from the neocortex and thalamus under anesthesia revealed a weak but noticeable correlation between cortical and thalamic propagation patterns. In vivo recordings from naturally sleeping rats showed propagating activity patterns in the thalamus during slow-wave sleep, but they exhibited patterns with a lower frequency and faster propagation than those under anesthesia. These findings suggest that spontaneous population activity propagation is intrinsic to the thalamocortical network during synchronized brain states like deep sleep or anesthesia. This research could contribute to a deeper understanding of these states as intricate neural processes. Subsequent studies should examine how different anesthetics influence thalamocortical activity and the distinct functions of various thalamic nuclei across different brain states. Analyzing single-unit activities from each thalamic nucleus might offer valuable insights into some of the unresolved questions.

A significant limitation in neuroscience is the scarcity of publicly available high-resolution neural recordings. This thesis also presents a dataset recorded from the neocortex of twenty rats anesthetized with ketamine/xylazine. The dataset contains raw neural recordings, spike times, extracellular spike waveforms, and unit properties in a standardized format. We provide technical validation, presenting distributions of derived unit properties and various spike sorting quality metrics. This dataset offers numerous benefits, such as facilitating detailed analyses of neuronal firing patterns, aiding neuron classification, and serving input for spike-sorting algorithms and data processing methods. Additionally, it may be used to investigate laminar-specific neuronal activity during slow oscillations.

A közelmúlt kutatási eredményei rámutattak arra, hogy az altatás és a mélyalvás során dominánsan megjelenő lassú hullámok összetett téridő mintázatokkal írhatók le. Azonban a vizsgálatok főként a kéregi régiókra korlátozódtak, míg a kéreg alatti területeken, mint például a thalamus, nem volt egyértelmű, hogy hasonló terjedési mintázatok megjelenhetnek-e. Disszertációmban ketamin/xylazin keverékével altatott és természetesen alvó rágcsáló modellekben, magas kontakt sűrűségű szilícium elektródák segítségével vizsgáltam a kortikothalamikus aktivitás mintázatait. Az eddigi megfigyelések alapján elmondható, hogy elsősorban a dorzális thalamus magjaiban figyelhető meg domináns terjedő aktivitás a dorzoventrális tengely mentén, kiemelve olyan magokat, mint a poszterior mag (Po), a laterális poszterior (LP) vagy a laterodorsális (LD) magok. A domináns terjedő aktivitás mintázatok felénél megállapítható, hogy az esetek felében a terjedés iránya a ventrális oldal felől a dorzális irányba mutat. Továbbá, a szimultán kérgi és thalamikus elvezetések altatás alatt gyenge, de észrevehető korrelációt mutattak a kortikális és thalamikus terjedési mintázatok között. A természetes alvás során rögzített elvezetésekben azonosított terjedő aktivitási mintázatok alacsonyabb frekvenciával és gyorsabb terjedéssel rendelkeztek, mint az altatás alatt regisztráltak. Az eredmények abba az irányba mutatnak, hogy a thalamokortikális hálózat működésében a spontán populációs aktivitás terjedő mintázatai erősen kötődnek a szinkronizált agyi állapotokhoz. A jövőben ezen eredmények hozzájárulhatnak az alvás és altatás hátterében meghúzódó mechanizmusok teljesebb megértéséhez.

Az idegtudományban manapság is kuriózumnak számítanak a szabadon elérhető, nagy téridőbeli felbontással készült felvételek. A ketamin/xylazin altatott patkányból készült kérgi adatbázisunk tartalmazza a nyers felvételeket, tüzelési időpontokat, tüske hullámformákat és egysejt aktivitáshoz köthető egyéb tulajdonságokat standardizált formátumban. Az elkészült technikai validáció, amit biztosítunk, tartalmaz még számos egysejthez, illetve a sejtválogatáshoz köthető metrikát. Az ilyen típusú adathalmazok olyan lehetőségeket nyitnak meg más kutatók előtt is, amelyek segíthetik a tüzelési mintázatok megértését illetve akár az neuronok osztályozását. Továbbá, fontos bemenet lehet a különböző spike-sorting algoritmusok fejlesztéséhez vagy bármilyen kapcsolódó feldolgozási eljáráshoz.

8 References

1. Maquet P. The role of sleep in learning and memory. Science. 2001;294(5544):1048-52.

2. Payne JD, Stickgold R, Swanberg K, Kensinger EA. Sleep preferentially enhances memory for emotional components of scenes. Psychol Sci. 2008;19(8):781-8.

3. Cousins JN, Fernández G. The impact of sleep deprivation on declarative memory. Prog Brain Res. 2019;246:27-53.

4. Harding EC, Franks NP, Wisden W. Sleep and thermoregulation. Current Opinion in Physiology. 2020;15:7-13.

5. Inoué S, Honda K, Komoda Y. Sleep as neuronal detoxification and restitution. Behavioural Brain Research. 1995;69(1):91-6.

6. Bryant PA, Trinder J, Curtis N. Sick and tired: does sleep have a vital role in the immune system? Nature Reviews Immunology. 2004;4(6):457-67.

7. Massimini M, Huber R, Ferrarelli F, Hill S, Tononi G. The sleep slow oscillation as a traveling wave. J Neurosci. 2004;24(31):6862-70.

8. Steriade M, McCormick DA, Sejnowski TJ. Thalamocortical Oscillations in the Sleeping and Aroused Brain. Science. 1993;262(5134):679-85.

9. Steriade M, Nunez A, Amzica F. Intracellular analysis of relations between the slow (< 1 Hz) neocortical oscillation and other sleep rhythms of the electroencephalogram. The Journal of Neuroscience. 1993;13(8):3266-83.

10. Steriade M, Nuñez A, Amzica F. A novel slow (< 1 Hz) oscillation of neocortical neurons in vivo: depolarizing and hyperpolarizing components. J Neurosci. 1993;13(8):3252-65.

11. Crunelli V, Hughes SW. The slow (<1 Hz) rhythm of non-REM sleep: a dialogue between three cardinal oscillators. Nat Neurosci. 2010;13(1):9-17.

12. Chauvette S, Crochet S, Volgushev M, Timofeev I. Properties of Slow Oscillation during Slow-Wave Sleep and Anesthesia in Cats. The Journal of Neuroscience. 2011;31(42):14998-5008.

13. Jun JJ, Steinmetz NA, Siegle JH, Denman DJ, Bauza M, Barbarits B, Lee AK, Anastassiou CA, Andrei A, Aydın Ç, Barbic M, Blanche TJ, Bonin V, Couto J, Dutta B, Gratiy SL, Gutnisky DA, Häusser M, Karsh B, Ledochowitsch P, Lopez CM, Mitelut C, Musa S, Okun M, Pachitariu M, Putzeys J, Rich PD, Rossant C, Sun WL, Svoboda K, Carandini M, Harris KD, Koch C, O'Keefe J, Harris TD. Fully integrated silicon probes for high-density recording of neural activity. Nature. 2017;551(7679):232-6.

14. Horváth C, Tóth LF, Ulbert I, Fiáth R. Dataset of cortical activity recorded with high spatial resolution from anesthetized rats. Scientific Data. 2021;8(1):180.

15. Sherman SM, Guillery RW. Functional Connections of Cortical Areas: A New View from the Thalamus: The MIT Press; 2013 23 Jan 2014.

16. Sherman SM. Thalamus plays a central role in ongoing cortical functioning. Nature Neuroscience. 2016;19(4):533-41.

17. Usrey WM, Sherman SM. Corticofugal circuits: Communication lines from the cortex to the rest of the brain. J Comp Neurol. 2019;527(3):640-50.

18. Puelles L, Rubenstein JL. Forebrain gene expression domains and the evolving prosomeric model. Trends Neurosci. 2003;26(9):469-76.

19. Puelles L, Rubenstein JL. Expression patterns of homeobox and other putative regulatory genes in the embryonic mouse forebrain suggest a neuromeric organization. Trends Neurosci. 1993;16(11):472-9.

20. Puelles L. Brain segmentation and forebrain development in amniotes. Brain Research Bulletin. 2001;55:695-710.

21. Puelles L. A segmental morphological paradigm for understanding vertebrate forebrains. Brain Behav Evol. 1995;46(4-5):319-37.

22. Puelles E, Annino A, Tuorto F, Usiello A, Acampora D, Czerny T, Brodski C, Ang SL, Wurst W, Simeone A. Otx2 regulates the extent, identity and fate of neuronal progenitor domains in the ventral midbrain. Development. 2004;131(9):2037-48.

23. Jones EG. The thalamus: Springer Science & Business Media; 2012.

24. Sherman SM. The thalamus is more than just a relay. Curr Opin Neurobiol. 2007;17(4):417-22.

25. Sherman SM, Guillery RW. Exploring the thalamus: Elsevier; 2001.

26. Sherman SM, Guillery RW, Sherman SM. Exploring the thalamus and its role in cortical function. 2nd ed. Cambridge, Mass: MIT Press; 2006.

27. Jones EG. The thalamus. 2nd ed. Cambridge, UK: Cambridge University Press; 2007.

28. Erişir A, Van Horn SC, Sherman SM. Relative numbers of cortical and brainstem inputs to the lateral geniculate nucleus. Proc Natl Acad Sci U S A. 1997;94(4):1517-20.

29. Deschênes M, Veinante P, Zhang ZW. The organization of corticothalamic projections: reciprocity versus parity. Brain Res Brain Res Rev. 1998;28(3):286-308.

30. Groh A, De Kock CP, Wimmer VC, Sakmann B, Kuner T. Driver or coincidence detector: modal switch of a corticothalamic giant synapse controlled by spontaneous activity and short-term depression. Journal of Neuroscience. 2008;28(39):9652-63.

31. Bokor H, Frère SG, Eyre MD, Slézia A, Ulbert I, Lüthi A, Acsády L. Selective GABAergic control of higher-order thalamic relays. Neuron. 2005;45(6):929-40.

32. Barthó P, Freund TF, Acsády L. Selective GABAergic innervation of thalamic nuclei from zona incerta. Eur J Neurosci. 2002;16(6):999-1014.

33. Nakagawa Y. Development of the thalamus: From early patterning to regulation of cortical functions. Wiley Interdiscip Rev Dev Biol. 2019;8(5):e345.

34. Jager P, Moore G, Calpin P, Durmishi X, Salgarella I, Menage L, Kita Y, Wang Y, Kim DW, Blackshaw S, Schultz SR, Brickley S, Shimogori T, Delogu A. Dual midbrain and forebrain origins of thalamic inhibitory interneurons. Elife. 2021;10.

35. Jorfi M, Skousen JL, Weder C, Capadona JR. Progress towards biocompatible intracortical microelectrodes for neural interfacing applications. Journal of Neural Engineering. 2015;12(1):011001.

36. Avendan C, Stepniewska I, Rausell E, Reinoso-Suarez F. Segregation and heterogeneity of thalamic cell populations projecting to superficial layers of posterior parietal cortex: a retrograde tracer study in cat and monkey. Neuroscience. 1990;39(3):547-59.

37. Guillery RW. A study of Golgi preparations from the dorsal lateral geniculate nucleus of the adult cat. J Comp Neurol. 1966;128(1):21-50.

38. Szentágothai J, Hámori J, Tömböl T. Degeneration and electron microscope analysis of the synaptic glomeruli in the lateral geniculate body. Exp Brain Res. 1966;2(4):283-301.

39. Unzai T, Kuramoto E, Kaneko T, Fujiyama F. Quantitative Analyses of the Projection of Individual Neurons from the Midline Thalamic Nuclei to the Striosome and Matrix Compartments of the Rat Striatum. Cerebral Cortex. 2015;27(2):1164-81.

40. Lanciego JL, Gonzalo N, Castle M, Sanchez-Escobar C, Aymerich MS, Obeso JA. Thalamic innervation of striatal and subthalamic neurons projecting to the rat entopeduncular nucleus. Eur J Neurosci. 2004;19(5):1267-77.

41. Rodriguez-Moreno J, Rollenhagen A, Arlandis J, Santuy A, Merchan-Pérez A, DeFelipe J, Lübke JHR, Clasca F. Quantitative 3D Ultrastructure of Thalamocortical Synapses from the "Lemniscal" Ventral Posteromedial Nucleus in Mouse Barrel Cortex. Cerebral Cortex. 2017;28(9):3159-75.

42. Casas-Torremocha D, Porrero C, Rodriguez-Moreno J, García-Amado M, Lübke JHR, Núñez Á, Clascá F. Posterior thalamic nucleus axon terminals have different structure and functional impact in the motor and somatosensory vibrissal cortices. Brain Struct Funct. 2019;224(4):1627-45.

43. Guillery RW, Sherman SM. Thalamic relay functions and their role in corticocortical communication: generalizations from the visual system. Neuron. 2002;33(2):163-75.

44. Guillery RW. Anatomical evidence concerning the role of the thalamus in corticocortical communication: a brief review. J Anat. 1995;187 (Pt 3)(Pt 3):583-92.

45. Rodriguez-Moreno J, Porrero C, Rollenhagen A, Rubio-Teves M, Casas-Torremocha D, Alonso-Nanclares L, Yakoubi R, Santuy A, Merchan-Pérez A, DeFelipe J. Area-specific synapse structure in branched posterior nucleus axons reveals a new level of complexity in thalamocortical networks. Journal of Neuroscience. 2020;40(13):2663-79.

46. Familtsev D, Quiggins R, Masterson SP, Dang W, Slusarczyk AS, Petry HM, Bickford ME. Ultrastructure of geniculocortical synaptic connections in the tree shrew striate cortex. J Comp Neurol. 2016;524(6):1292-306.

47. Ohno S, Kuramoto E, Furuta T, Hioki H, Tanaka YR, Fujiyama F, Sonomura T, Uemura M, Sugiyama K, Kaneko T. A Morphological Analysis of Thalamocortical Axon Fibers of Rat Posterior Thalamic Nuclei: A Single Neuron Tracing Study with Viral Vectors. Cerebral Cortex. 2011;22(12):2840-57.

48. Nakamura H, Hioki H, Furuta T, Kaneko T. Different cortical projections from three subdivisions of the rat lateral posterior thalamic nucleus: a single-neuron tracing study with viral vectors. European Journal of Neuroscience. 2015;41(10):1294-310.
49. Arbuthnott G, MacLeod N, Maxwell D, Wright A. Distribution and synaptic contacts of the cortical terminals arising from neurons in the rat ventromedial thalamic nucleus. Neuroscience. 1990;38(1):47-60.
50. Scott JC, Omar JA, Tanya RS, Saundra LP, Amalia NG, Margot E, Barry WC. Thalamic Control of Layer 1 Circuits in Prefrontal Cortex. The Journal of Neuroscience. 2012;32(49):17813.
51. Jones EG. The thalamic matrix and thalamocortical synchrony. Trends Neurosci. 2001;24(10):595-601.
52. Jones EG. Viewpoint: the core and matrix of thalamic organization. Neuroscience. 1998;85(2):331-45.
53. Clascá F, Rubio-Garrido P, Jabaudon D. Unveiling the diversity of thalamocortical neuron subtypes. Eur J Neurosci. 2012;35(10):1524-32.
54. Descheˆnes M, Bourassa J, Parent A. Two different types of thalamic fibers innervate the rat striatum. Brain Research. 1995;701(1):288-92.
55. Sherman SM, Guillery RW. Functional organization of thalamocortical relays. J Neurophysiol. 1996;76(3):1367-95.
56. Reichova I, Sherman SM. Somatosensory corticothalamic projections: distinguishing drivers from modulators. J Neurophysiol. 2004;92(4):2185-97.
57. Sherman SM, Guillery RW. On the actions that one nerve cell can have on another: Distinguishing “drivers” from “modulators”. Proceedings of the National Academy of Sciences. 1998;95(12):7121-6.
58. Herkenham M. Laminar organization of thalamic projections to the rat neocortex. Science. 1980;207(4430):532-5.
59. Clascá F, Porrero C, Galazo M, Rubio Garrido P, Evangelio M. Anatomy and Development of Multispecific Thalamocortical Axons: Implications for Cortical Dynamics and Evolution. 2015. p. 69-92.

60. Bickford ME, Zhou N, Krahe TE, Govindaiah G, Guido W. Retinal and tectal "driver-like" inputs converge in the shell of the mouse dorsal lateral geniculate nucleus. The Journal of Neuroscience. 2015;35(29):10523-34.

61. Kuramoto E, Ohno S, Furuta T, Unzai T, Tanaka YR, Hioki H, Kaneko T. Ventral Medial Nucleus Neurons Send Thalamocortical Afferents More Widely and More Preferentially to Layer 1 than Neurons of the Ventral Anterior–Ventral Lateral Nuclear Complex in the Rat. Cerebral Cortex. 2013;25(1):221-35.

62. Llinás RR. Intrinsic electrical properties of mammalian neurons and CNS function: a historical perspective. Front Cell Neurosci. 2014;8:320.

63. Meuth SG, Kanyshkova T, Meuth P, Landgraf P, Munsch T, Ludwig A, Hofmann F, Pape HC, Budde T. Membrane resting potential of thalamocortical relay neurons is shaped by the interaction among TASK3 and HCN2 channels. J Neurophysiol. 2006;96(3):1517-29.

64. Broicher T, Kanyshkova T, Meuth P, Pape HC, Budde T. Correlation of T-channel coding gene expression, IT, and the low threshold Ca2+ spike in the thalamus of a rat model of absence epilepsy. Mol Cell Neurosci. 2008;39(3):384-99.

65. Leist M, Datunashvilli M, Kanyshkova T, Zobeiri M, Aissaoui A, Cerina M, Romanelli MN, Pape HC, Budde T. Two types of interneurons in the mouse lateral geniculate nucleus are characterized by different h-current density. Sci Rep. 2016;6:24904.

66. Hashimoto K. Mechanisms for the resonant property in rodent neurons. Neurosci Res. 2020;156:5-13.

67. Amarillo Y, Zagha E, Mato G, Rudy B, Nadal MS. The interplay of seven subthreshold conductances controls the resting membrane potential and the oscillatory behavior of thalamocortical neurons. J Neurophysiol. 2014;112(2):393-410.

68. Zobeiri M, Chaudhary R, Datunashvili M, Heuermann RJ, Lüttjohann A, Narayanan V, Balfanz S, Meuth P, Chetkovich DM, Pape HC, Baumann A, van Luijtelaar G, Budde T. Modulation of thalamocortical oscillations by TRIP8b, an auxiliary subunit for HCN channels. Brain Struct Funct. 2018;223(3):1537-64.

69. Zhu J, Heggelund P. Muscarinic regulation of dendritic and axonal outputs of rat thalamic interneurons: a new cellular mechanism for uncoupling distal dendrites. J Neurosci. 2001;21(4):1148-59.

70. McCormick DA, Pape HC. Acetylcholine inhibits identified interneurons in the cat lateral geniculate nucleus. Nature. 1988;334(6179):246-8.

71. Crunelli V, Lőrincz ML, Connelly WM, David F, Hughes SW, Lambert RC, Leresche N, Errington AC. Dual function of thalamic low-vigilance state oscillations: rhythm-regulation and plasticity. Nat Rev Neurosci. 2018;19(2):107-18.

72. Cox CL. Complex regulation of dendritic transmitter release from thalamic interneurons. Curr Opin Neurobiol. 2014;29:126-32.

73. Llinás RR, Ribary U, Jeanmonod D, Kronberg E, Mitra PP. Thalamocortical dysrhythmia: A neurological and neuropsychiatric syndrome characterized by magnetoencephalography. Proc Natl Acad Sci U S A. 1999;96(26):15222-7.

74. Clemente-Perez A, Makinson SR, Higashikubo B, Brovarney S, Cho FS, Urry A, Holden SS, Wimer M, Dávid C, Fenno LE, Acsády L, Deisseroth K, Paz JT. Distinct Thalamic Reticular Cell Types Differentially Modulate Normal and Pathological Cortical Rhythms. Cell Rep. 2017;19(10):2130-42.

75. Halnes G, Augustinaite S, Heggelund P, Einevoll GT, Migliore M. A Multi-Compartment Model for Interneurons in the Dorsal Lateral Geniculate Nucleus. PLOS Computational Biology. 2011;7(9):e1002160.

76. Zhou NA, Maire PS, Masterson SP, Bickford ME. The mouse pulvinar nucleus: Organization of the tectorecipient zones. Visual Neuroscience. 2017;34:E011.

77. Krubitzer L, Kaas J. The evolution of the neocortex in mammals: how is phenotypic diversity generated? Curr Opin Neurobiol. 2005;15(4):444-53.

78. Pierret T, Lavallée P, Deschênes M. Parallel streams for the relay of vibrissal information through thalamic barreloids. J Neurosci. 2000;20(19):7455-62.

79. Bruno RM, Sakmann B. Cortex is driven by weak but synchronously active thalamocortical synapses. Science. 2006;312(5780):1622-7.

80. Wimmer VC, Bruno RM, de Kock CP, Kuner T, Sakmann B. Dimensions of a projection column and architecture of VPM and POm axons in rat vibrissal cortex. Cereb Cortex. 2010;20(10):2265-76.

81. Thompson SM, Robertson RT. Organization of subcortical pathways for sensory projections to the limbic cortex. II. Afferent projections to the thalamic lateral dorsal nucleus in the rat. J Comp Neurol. 1987;265(2):189-202.

82. Takahashi T. The organization of the lateral thalamus of the hooded rat. Journal of Comparative Neurology. 1985;231(3):281-309.

83. Juavinett AL, Kim EJ, Collins HC, Callaway EM. A systematic topographical relationship between mouse lateral posterior thalamic neurons and their visual cortical projection targets. Journal of Comparative Neurology. 2020;528(1):99-111.

84. Shibata H. Organization of retrosplenial cortical projections to the laterodorsal thalamic nucleus in the rat. Neuroscience Research. 2000;38(3):303-11.

85. Shibata H, Naito J. Organization of anterior cingulate and frontal cortical projections to the anterior and laterodorsal thalamic nuclei in the rat. Brain Res. 2005;1059(1):93-103.

86. Wilton LA, Baird AL, Muir JL, Honey RC, Aggleton JP. Loss of the thalamic nuclei for "head direction" impairs performance on spatial memory tasks in rats. Behav Neurosci. 2001;115(4):861-9.

87. Bezdudnaya T, Keller A. Laterodorsal nucleus of the thalamus: A processor of somatosensory inputs. J Comp Neurol. 2008;507(6):1979-89.

88. McFarland NR, Haber SN. Thalamic relay nuclei of the basal ganglia form both reciprocal and nonreciprocal cortical connections, linking multiple frontal cortical areas. J Neurosci. 2002;22(18):8117-32.

89. Kakei S, Hoffman DS, Strick PL. Direction of action is represented in the ventral premotor cortex. Nat Neurosci. 2001;4(10):1020-5.

90. Kuramoto E, Furuta T, Nakamura KC, Unzai T, Hioki H, Kaneko T. Two types of thalamocortical projections from the motor thalamic nuclei of the rat: a single neuron-tracing study using viral vectors. Cereb Cortex. 2009;19(9):2065-77.

91. Winer JA, Miller LM, Lee CC, Schreiner CE. Auditory thalamocortical transformation: structure and function. Trends Neurosci. 2005;28(5):255-63.

92. LeDoux JE. Emotion circuits in the brain. Annual review of neuroscience. 2000;23(1):155-84.

93. Anderson LA, Christianson GB, Linden JF. Stimulus-specific adaptation occurs in the auditory thalamus. J Neurosci. 2009;29(22):7359-63.
94. Sillito AM, Jones HE. Corticothalamic interactions in the transfer of visual information. Philos Trans R Soc Lond B Biol Sci. 2002;357(1428):1739-52.
95. Butti C, Raghanti MA, Sherwood CC, Hof PR. The neocortex of cetaceans: cytoarchitecture and comparison with other aquatic and terrestrial species. Annals of the New York Academy of Sciences. 2011;1225(1):47-58.
96. Wagstyl K, Larocque S, Cucurull G, Lepage C, Cohen JP, Bludau S, Palomero-Gallagher N, Lewis LB, Funck T, Spitzer H, Dickscheid T, Fletcher PC, Romero A, Zilles K, Amunts K, Bengio Y, Evans AC. BigBrain 3D atlas of cortical layers: Cortical and laminar thickness gradients diverge in sensory and motor cortices. PLOS Biology. 2020;18(4):e3000678.
97. von Economo C. Cellular Structure of the Human Cerebral Cortex: Translated and edited by L.C. Triarhou (Thessaloniki)Plus poster: 'The 107 Cortical Cytoarchitectonic Areas of Constantin von Economo and Georg N. Koskinas in the Adult Human Brain'. Triarhou LC, editor: S.Karger AG; 2009 07 Jul 2009.
98. Abeles M. Corticonics: Neural Circuits of the Cerebral Cortex. Cambridge: Cambridge University Press; 1991.
99. De Nò RL. Physiology of the nervous system. (No Title). 1949:288.
100. Defelipe J. The evolution of the brain, the human nature of cortical circuits, and intellectual creativity. Front Neuroanat. 2011;5:29.
101. DeFelipe J, Fariñas I. The pyramidal neuron of the cerebral cortex: morphological and chemical characteristics of the synaptic inputs. Prog Neurobiol. 1992;39(6):563-607.
102. Peters A, Jones EG. Cerebral Cortex: Functional properties of cortical cells: Plenum Press; 1984.
103. Steriade MM, McCarley RW. Brain Control of Wakefulness and Sleep: Springer US; 2007.
104. Steriade M, Timofeev I, Grenier F. Natural waking and sleep states: a view from inside neocortical neurons. Journal of neurophysiology. 2001;85(5):1969-85.

105. Nuñez A, Amzica F, Steriade M. Electrophysiology of cat association cortical cells in vivo: intrinsic properties and synaptic responses. J Neurophysiol. 1993;70(1):418-30.
106. Connors BW, Gutnick MJ, Prince DA. Electrophysiological properties of neocortical neurons in vitro. J Neurophysiol. 1982;48(6):1302-20.
107. Connors BW, Gutnick MJ. Intrinsic firing patterns of diverse neocortical neurons. Trends Neurosci. 1990;13(3):99-104.
108. Steriade M, Timofeev I. Neuronal plasticity in thalamocortical networks during sleep and waking oscillations. Neuron. 2003;37(4):563-76.
109. Somogyi P, Tamás G, Lujan R, Buhl EH. Salient features of synaptic organisation in the cerebral cortex. Brain Res Brain Res Rev. 1998;26(2-3):113-35.
110. Markram H, Toledo-Rodriguez M, Wang Y, Gupta A, Silberberg G, Wu C. Interneurons of the neocortical inhibitory system. Nat Rev Neurosci. 2004;5(10):793-807.
111. Freund TF, Buzsáki G. Interneurons of the hippocampus. Hippocampus. 1996;6(4):347-470.
112. Somogyi P. A specific 'axo-axonal' interneuron in the visual cortex of the rat. Brain Res. 1977;136(2):345-50.
113. Ascoli GA, Alonso-Nanclares L, Anderson SA, Barrionuevo G, Benavides-Piccione R, Burkhalter A, Buzsáki G, Cauli B, Defelipe J, Fairén A, Feldmeyer D, Fishell G, Fregnac Y, Freund TF, Gardner D, Gardner EP, Goldberg JH, Helmstaedter M, Hestrin S, Karube F, Kisvárday ZF, Lambolez B, Lewis DA, Marin O, Markram H, Muñoz A, Packer A, Petersen CC, Rockland KS, Rossier J, Rudy B, Somogyi P, Staiger JF, Tamas G, Thomson AM, Toledo-Rodriguez M, Wang Y, West DC, Yuste R. Petilla terminology: nomenclature of features of GABAergic interneurons of the cerebral cortex. Nat Rev Neurosci. 2008;9(7):557-68.
114. Azevedo FA, Carvalho LR, Grinberg LT, Farfel JM, Ferretti RE, Leite RE, Jacob Filho W, Lent R, Herculano-Houzel S. Equal numbers of neuronal and nonneuronal cells make the human brain an isometrically scaled-up primate brain. J Comp Neurol. 2009;513(5):532-41.
115. Pelvig DP, Pakkenberg H, Stark AK, Pakkenberg B. Neocortical glial cell numbers in human brains. Neurobiol Aging. 2008;29(11):1754-62.

116. Hobson JA, Pace-Schott EF. The cognitive neuroscience of sleep: neuronal systems, consciousness and learning. Nat Rev Neurosci. 2002;3(9):679-93.
117. Sharma S, Kavuru M. Sleep and Metabolism: An Overview. International Journal of Endocrinology. 2010;2010:270832.
118. Anafi RC, Kayser MS, Raizen DM. Exploring phylogeny to find the function of sleep. Nature Reviews Neuroscience. 2019;20(2):109-16.
119. Siegel JM. Do all animals sleep? Trends Neurosci. 2008;31(4):208-13.
120. Cirelli C, Tononi G. Is sleep essential? PLoS Biol. 2008;6(8):e216.
121. Nath RD, Bedbrook CN, Abrams MJ, Basinger T, Bois JS, Prober DA, Sternberg PW, Gradinaru V, Goentoro L. The jellyfish Cassiopea exhibits a sleep-like state. Current Biology. 2017;27(19):2984-90. e3.
122. Nickel M. Kinetics and rhythm of body contractions in the sponge Tethya wilhelma (Porifera: Demospongiae). J Exp Biol. 2004;207(Pt 26):4515-24.
123. Berry RB, Budhiraja R, Gottlieb DJ, Gozal D, Iber C, Kapur VK, Marcus CL, Mehra R, Parthasarathy S, Quan SF, Redline S, Strohl KP, Davidson Ward SL, Tangredi MM. Rules for scoring respiratory events in sleep: update of the 2007 AASM Manual for the Scoring of Sleep and Associated Events. Deliberations of the Sleep Apnea Definitions Task Force of the American Academy of Sleep Medicine. J Clin Sleep Med. 2012;8(5):597-619.
124. Bódizs R. Alvás, álom, bioritmusok. Budapest: Medicina. 2000.
125. Blume C, del Giudice R, Wislowska M, Lechinger J, Schabus M. Across the consciousness continuum–from unresponsive wakefulness to sleep. Frontiers in Human Neuroscience. 2015;9:105.
126. Jouvet M. Paradoxical sleep as a programming system. Journal of Sleep Research. 1998;7(S1):1-5.
127. Lacroix MM, de Lavilléon G, Lefort J, El Kanbi K, Bagur S, Laventure S, Dauvilliers Y, Peyron C, Benchenane K. Improved sleep scoring in mice reveals human-like stages. BioRxiv. 2018:489005.
128. Benington JH, Frank MG. Cellular and molecular connections between sleep and synaptic plasticity. Progress in Neurobiology. 2003;69(2):71-101.

129. Killgore WDS. Effects of sleep deprivation on cognition. In: Kerkhof GA, Dongen HPAv, editors. Progress in Brain Research. 185: Elsevier; 2010. p. 105-29.
130. Jike M, Itani O, Watanabe N, Buysse DJ, Kaneita Y. Long sleep duration and health outcomes: A systematic review, meta-analysis and meta-regression. Sleep Medicine Reviews. 2018;39:25-36.
131. Destexhe A, Contreras D, Steriade M. Spatiotemporal analysis of local field potentials and unit discharges in cat cerebral cortex during natural wake and sleep states. Journal of Neuroscience. 1999;19(11):4595-608.
132. Wilson CJ, Groves PM. Spontaneous firing patterns of identified spiny neurons in the rat neostriatum. Brain Res. 1981;220(1):67-80.
133. Mölle M, Marshall L, Gais S, Born J. Grouping of spindle activity during slow oscillations in human non-rapid eye movement sleep. J Neurosci. 2002;22(24):10941-7.
134. Isomura Y, Sirota A, Ozen S, Montgomery S, Mizuseki K, Henze DA, Buzsáki G. Integration and segregation of activity in entorhinal-hippocampal subregions by neocortical slow oscillations. Neuron. 2006;52(5):871-82.
135. Luczak A, Barthó P, Marguet SL, Buzsáki G, Harris KD. Sequential structure of neocortical spontaneous activity in vivo. Proceedings of the National Academy of Sciences. 2007;104(1):347-52.
136. Sanchez-Vives MV, McCormick DA. Cellular and network mechanisms of rhythmic recurrent activity in neocortex. Nat Neurosci. 2000;3(10):1027-34.
137. Lőrincz ML, Gunner D, Bao Y, Connelly WM, Isaac JTR, Hughes SW, Crunelli V. A Distinct Class of Slow (~0.2–2 Hz) Intrinsically Bursting Layer 5 Pyramidal Neurons Determines UP/DOWN State Dynamics in the Neocortex. The Journal of Neuroscience. 2015;35(14):5442-58.
138. Steriade M, Amzica F, Contreras D. Synchronization of fast (30-40 Hz) spontaneous cortical rhythms during brain activation. The Journal of Neuroscience. 1996;16(1):392-417.
139. Sakata S, Harris KD. Laminar structure of spontaneous and sensory-evoked population activity in auditory cortex. Neuron. 2009;64(3):404-18.
140. Chauvette S, Volgushev M, Timofeev I. Origin of Active States in Local Neocortical Networks during Slow Sleep Oscillation. Cerebral Cortex. 2010;20(11):2660-74.

141. Shu Y, Hasenstaub A, McCormick DA. Turning on and off recurrent balanced cortical activity. Nature. 2003;423(6937):288-93.

142. Crunelli V, Lörincz ML, Errington AC, Hughes SW. Activity of cortical and thalamic neurons during the slow (<1 Hz) rhythm in the mouse in vivo. Pflugers Arch. 2012;463(1):73-88.

143. Marder E, Abbott L, Turrigiano GG, Liu Z, Golowasch J. Memory from the dynamics of intrinsic membrane currents. Proceedings of the national academy of sciences. 1996;93(24):13481-6.

144. Major G, Larkum ME, Schiller J. Active properties of neocortical pyramidal neuron dendrites. Annual review of neuroscience. 2013;36:1-24.

145. Steriade M, Contreras D, Dossi RC, Nunez A. The slow (< 1 Hz) oscillation in reticular thalamic and thalamocortical neurons: scenario of sleep rhythm generation in interacting thalamic and neocortical networks. Journal of Neuroscience. 1993;13(8):3284-99.

146. Favero M, Castro-Alamancos MA. Synaptic cooperativity regulates persistent network activity in neocortex. J Neurosci. 2013;33(7):3151-63.

147. Castro-Alamancos MA, Favero M. NMDA receptors are the basis for persistent network activity in neocortex slices. Journal of Neurophysiology. 2015;113(10):3816-26.

148. Neske GT, Patrick SL, Connors BW. Contributions of diverse excitatory and inhibitory neurons to recurrent network activity in cerebral cortex. Journal of Neuroscience. 2015;35(3):1089-105.

149. Waters J, Helmchen F. Background synaptic activity is sparse in neocortex. Journal of Neuroscience. 2006;26(32):8267-77.

150. Rudolph M, Pospischil M, Timofeev I, Destexhe A. Inhibition determines membrane potential dynamics and controls action potential generation in awake and sleeping cat cortex. Journal of neuroscience. 2007;27(20):5280-90.

151. Haider B, Duque A, Hasenstaub AR, McCormick DA. Neocortical network activity in vivo is generated through a dynamic balance of excitation and inhibition. Journal of Neuroscience. 2006;26(17):4535-45.

152. Schwindt P, Spain W, Crill W. Calcium-dependent potassium currents in neurons from cat sensorimotor cortex. Journal of Neurophysiology. 1992;67(1):216-26.
153. Crochet S, Petersen CCH. Correlating whisker behavior with membrane potential in barrel cortex of awake mice. Nature Neuroscience. 2006;9(5):608-10.
154. Poulet JFA, Petersen CCH. Internal brain state regulates membrane potential synchrony in barrel cortex of behaving mice. Nature. 2008;454(7206):881-5.
155. Gentet LJ, Avermann M, Matyas F, Staiger JF, Petersen CC. Membrane potential dynamics of GABAergic neurons in the barrel cortex of behaving mice. Neuron. 2010;65(3):422-35.
156. Vyazovskiy VV, Olcese U, Hanlon EC, Nir Y, Cirelli C, Tononi G. Local sleep in awake rats. Nature. 2011;472(7344):443-7.
157. MacDonald JF, Bartlett MC, Mody I, Pahapill P, Reynolds JN, Salter MW, Schneiderman JH, Pennefather PS. Actions of ketamine, phencyclidine and MK-801 on NMDA receptor currents in cultured mouse hippocampal neurones. J Physiol. 1991;432:483-508.
158. Liu J, Ji XQ, Zhu XZ. Comparison of psychic emergence reactions after (+/-)-ketamine and (+)-ketamine in mice. Life Sci. 2006;78(16):1839-44.
159. Rudolph U, Antkowiak B. Molecular and neuronal substrates for general anaesthetics. Nat Rev Neurosci. 2004;5(9):709-20.
160. Boucetta S, Jones BE. Activity profiles of cholinergic and intermingled GABAergic and putative glutamatergic neurons in the pontomesencephalic tegmentum of urethane-anesthetized rats. J Neurosci. 2009;29(14):4664-74.
161. Pirker S, Schwarzer C, Wieselthaler A, Sieghart W, Sperk G. GABA(A) receptors: immunocytochemical distribution of 13 subunits in the adult rat brain. Neuroscience. 2000;101(4):815-50.
162. Hevers W, Hadley SH, Lüddens H, Amin J. Ketamine, but not phencyclidine, selectively modulates cerebellar GABA(A) receptors containing alpha6 and delta subunits. J Neurosci. 2008;28(20):5383-93.
163. Hedler L, Stamm G, Weitzell R, Starke K. Functional characterization of central alpha-adrenoceptors by yohimbine diastereomers. Eur J Pharmacol. 1981;70(1):43-52.

164. Nicholas AP, Pieribone V, Hökfelt T. Distributions of mRNAs for alpha-2 adrenergic receptor subtypes in rat brain: an in situ hybridization study. J Comp Neurol. 1993;328(4):575-94.

165. Wang M, Ramos BP, Paspalas CD, Shu Y, Simen A, Duque A, Vijayraghavan S, Brennan A, Dudley A, Nou E, Mazer JA, McCormick DA, Arnsten AF. Alpha2A-adrenoceptors strengthen working memory networks by inhibiting cAMP-HCN channel signaling in prefrontal cortex. Cell. 2007;129(2):397-410.

166. Zhang H, Watrous AJ, Patel A, Jacobs J. Theta and Alpha Oscillations Are Traveling Waves in the Human Neocortex. Neuron. 2018;98(6):1269-81.e4.

167. Shin D, Peelman K, Lien AD, Del Rosario J, Haider B. Narrowband gamma oscillations propagate and synchronize throughout the mouse thalamocortical visual system. Neuron. 2023;111(7):1076-85.e8.

168. Bhattacharya S, Brincat SL, Lundqvist M, Miller EK. Traveling waves in the prefrontal cortex during working memory. PLOS Computational Biology. 2022;18(1):e1009827.

169. Buzsáki G, Draguhn A. Neuronal oscillations in cortical networks. Science. 2004;304(5679):1926-9.

170. Fuster JM. Cortex and mind: Unifying cognition: Oxford university press; 2002.

171. Delis I, Ince RAA, Sajda P, Wang Q. Neural Encoding of Active Multi-Sensing Enhances Perceptual Decision-Making via a Synergistic Cross-Modal Interaction. J Neurosci. 2022;42(11):2344-55.

172. Roelfsema PR, Engel AK, König P, Singer W. Visuomotor integration is associated with zero time-lag synchronization among cortical areas. Nature. 1997;385(6612):157-61.

173. Uhlhaas P, Pipa G, Lima B, Melloni L, Neuenschwander S, Nikolić D, Singer W. Neural synchrony in cortical networks: history, concept and current status. Frontiers in Integrative Neuroscience. 2009;3.

174. Maynard EM, Nordhausen CT, Normann RA. The Utah Intracortical Electrode Array: A recording structure for potential brain-computer interfaces. Electroencephalography and Clinical Neurophysiology. 1997;102(3):228-39.

175. Shoham D, Glaser DE, Arieli A, Kenet T, Wijnbergen C, Toledo Y, Hildesheim R, Grinvald A. Imaging cortical dynamics at high spatial and temporal resolution with novel blue voltage-sensitive dyes. Neuron. 1999;24(4):791-802.

176. Axonal conduction delays. Scholarpedia. 2012;7:1451.

177. Girard P, Hupé JM, Bullier J. Feedforward and feedback connections between areas V1 and V2 of the monkey have similar rapid conduction velocities. J Neurophysiol. 2001;85(3):1328-31.

178. Murphy M, Riedner BA, Huber R, Massimini M, Ferrarelli F, Tononi G. Source modeling sleep slow waves. Proceedings of the National Academy of Sciences. 2009;106(5):1608-13.

179. Riedner BA, Vyazovskiy VV, Huber R, Massimini M, Esser S, Murphy M, Tononi G. Sleep homeostasis and cortical synchronization: III. A high-density EEG study of sleep slow waves in humans. Sleep. 2007;30(12):1643-57.

180. Dasilva M, Camassa A, Navarro-Guzman A, Pazienti A, Perez-Mendez L, Zamora-López G, Mattia M, Sanchez-Vives MV. Modulation of cortical slow oscillations and complexity across anesthesia levels. Neuroimage. 2021;224:117415.

181. Hangya B, Tihanyi BT, Entz L, Fabó D, Erőss L, Wittner L, Jakus R, Varga V, Freund TF, Ulbert I. Complex Propagation Patterns Characterize Human Cortical Activity during Slow-Wave Sleep. The Journal of Neuroscience. 2011;31(24):8770-9.

182. Pazienti A, Galluzzi A, Dasilva M, Sanchez-Vives MV, Mattia M. Slow waves form expanding, memory-rich mesostates steered by local excitability in fading anesthesia. iScience. 2022;25(3):103918.

183. Fucke T, Suchanek D, Nawrot MP, Seamari Y, Heck DH, Aertsen A, Boucsein C. Stereotypical spatiotemporal activity patterns during slow-wave activity in the neocortex. J Neurophysiol. 2011;106(6):3035-44.

184. Greenberg A, Abadchi JK, Dickson CT, Mohajerani MH. New waves: Rhythmic electrical field stimulation systematically alters spontaneous slow dynamics across mouse neocortex. Neuroimage. 2018;174:328-39.

185. Afrashteh N, Inayat S, Bermudez-Contreras E, Luczak A, McNaughton BL, Mohajerani MH. Spatiotemporal structure of sensory-evoked and spontaneous activity

revealed by mesoscale imaging in anesthetized and awake mice. Cell Rep. 2021;37(10):110081.

186. Brier LM, Landsness EC, Snyder AZ, Wright PW, Baxter GA, Bauer AQ, Lee JM, Culver JP. Separability of calcium slow waves and functional connectivity during wake, sleep, and anesthesia. Neurophotonics. 2019;6(3):035002.

187. Ferezou I, Bolea S, Petersen CCH. Visualizing the Cortical Representation of Whisker Touch: Voltage-Sensitive Dye Imaging in Freely Moving Mice. Neuron. 2006;50(4):617-29.

188. Liang Y, Song C, Liu M, Gong P, Zhou C, Knöpfel T. Cortex-Wide Dynamics of Intrinsic Electrical Activities: Propagating Waves and Their Interactions. The Journal of Neuroscience. 2021;41(16):3665-78.

189. MacDowell CJ, Buschman TJ. Low-Dimensional Spatiotemporal Dynamics Underlie Cortex-wide Neural Activity. Curr Biol. 2020;30(14):2665-80.e8.

190. Mohajerani MH, Chan AW, Mohsenvand M, LeDue J, Liu R, McVea DA, Boyd JD, Wang YT, Reimers M, Murphy TH. Spontaneous cortical activity alternates between motifs defined by regional axonal projections. Nat Neurosci. 2013;16(10):1426-35.

191. Mohajerani MH, McVea DA, Fingas M, Murphy TH. Mirrored bilateral slow-wave cortical activity within local circuits revealed by fast bihemispheric voltage-sensitive dye imaging in anesthetized and awake mice. J Neurosci. 2010;30(10):3745-51.

192. Niethard N, Ngo HV, Ehrlich I, Born J. Cortical circuit activity underlying sleep slow oscillations and spindles. Proc Natl Acad Sci U S A. 2018;115(39):E9220-e9.

193. Petersen CC, Grinvald A, Sakmann B. Spatiotemporal dynamics of sensory responses in layer 2/3 of rat barrel cortex measured in vivo by voltage-sensitive dye imaging combined with whole-cell voltage recordings and neuron reconstructions. J Neurosci. 2003;23(4):1298-309.

194. Reyes-Puerta V, Yang JW, Siwek ME, Kilb W, Sun JJ, Luhmann HJ. Propagation of spontaneous slow-wave activity across columns and layers of the adult rat barrel cortex in vivo. Brain Struct Funct. 2016;221(9):4429-49.

195. Stroh A, Adelsberger H, Groh A, Rühlmann C, Fischer S, Schierloh A, Deisseroth K, Konnerth A. Making Waves: Initiation and Propagation of Corticothalamic Ca2+ Waves In Vivo. Neuron. 2013;77(6):1136-50.

196. Takagaki K, Zhang C, Wu J-Y, Lippert MT. Crossmodal propagation of sensory-evoked and spontaneous activity in the rat neocortex. Neurosci Lett. 2008;431(3):191-6.

197. Vanni MP, Chan AW, Balbi M, Silasi G, Murphy TH. Mesoscale Mapping of Mouse Cortex Reveals Frequency-Dependent Cycling between Distinct Macroscale Functional Modules. The Journal of Neuroscience. 2017;37(31):7513-33.

198. Xiao D, Vanni MP, Mitelut CC, Chan AW, LeDue JM, Xie Y, Chen ACN, Swindale NV, Murphy TH. Mapping cortical mesoscopic networks of single spiking cortical or sub-cortical neurons. eLife. 2017;6:e19976.

199. Xu W, Huang X, Takagaki K, Wu JY. Compression and reflection of visually evoked cortical waves. Neuron. 2007;55(1):119-29.

200. Greenberg A, Dickson CT. Spontaneous and electrically modulated spatiotemporal dynamics of the neocortical slow oscillation and associated local fast activity. Neuroimage. 2013;83:782-94.

201. Matsui T, Murakami T, Ohki K. Transient neuronal coactivations embedded in globally propagating waves underlie resting-state functional connectivity. Proceedings of the National Academy of Sciences. 2016;113(23):6556-61.

202. Niethard N, Ngo H-VV, Ehrlich I, Born J. Cortical circuit activity underlying sleep slow oscillations and spindles. Proceedings of the National Academy of Sciences. 2018;115(39):E9220-E9.

203. Ruiz-Mejias M, Ciria-Suarez L, Mattia M, Sanchez-Vives MV. Slow and fast rhythms generated in the cerebral cortex of the anesthetized mouse. J Neurophysiol. 2011;106(6):2910-21.

204. Sheroziya M, Timofeev I. Global intracellular slow-wave dynamics of the thalamocortical system. J Neurosci. 2014;34(26):8875-93.

205. Slézia A, Hangya B, Ulbert I, Acsády L. Phase advancement and nucleus-specific timing of thalamocortical activity during slow cortical oscillation. J Neurosci. 2011;31(2):607-17.

206. Ujma PP, Szalárdy O, Fabó D, Erőss L, Bódizs R. Thalamic activity during scalp slow waves in humans. Neuroimage. 2022;257:119325.
207. Ushimaru M, Ueta Y, Kawaguchi Y. Differentiated Participation of Thalamocortical Subnetworks in Slow/Spindle Waves and Desynchronization. The Journal of Neuroscience. 2012;32(5):1730-46.
208. Hubel DH. Tungsten Microelectrode for Recording from Single Units. Science. 1957;125(3247):549-50.
209. Gray CM, Maldonado PE, Wilson M, McNaughton B. Tetrodes markedly improve the reliability and yield of multiple single-unit isolation from multi-unit recordings in cat striate cortex. Journal of neuroscience methods. 1995;63(1-2):43-54.
210. Hoffman KL, McNaughton BL. Coordinated reactivation of distributed memory traces in primate neocortex. Science. 2002;297(5589):2070-3.
211. Wise KD, Anderson DJ, Hetke JF, Kipke DR, Najafi K. Wireless implantable microsystems: high-density electronic interfaces to the nervous system. Proceedings of the IEEE. 2004;92:76-97.
212. Campbell PK, Jones KE, Huber RJ, Horch KW, Normann RA. A silicon-based, three-dimensional neural interface: manufacturing processes for an intracortical electrode array. IEEE Trans Biomed Eng. 1991;38(8):758-68.
213. Campbell PK, Jones KE, Huber RJ, Horch KW, Normann RA. A silicon-based, three-dimensional neural interface: manufacturing processes for an intracortical electrode array. IEEE Transactions on Biomedical Engineering. 1991;38(8):758-68.
214. Jones KE, Campbell PK, Normann RA. A glass/silicon composite intracortical electrode array. Annals of Biomedical Engineering. 1992;20(4):423-37.
215. Nordhausen CT, Maynard EM, Normann RA. Single unit recording capabilities of a 100 microelectrode array. Brain Res. 1996;726(1-2):129-40.
216. Reed JL, Pouget P, Qi H-X, Zhou Z, Bernard MR, Burish MJ, Haitas J, Bonds AB, Kaas JH. Widespread spatial integration in primary somatosensory cortex. Proceedings of the National Academy of Sciences. 2008;105(29):10233-7.
217. Stevenson IH, Kording KP. How advances in neural recording affect data analysis. Nature Neuroscience. 2011;14(2):139-42.

218. Stringer C, Pachitariu M, Steinmetz N, Reddy CB, Carandini M, Harris KD. Spontaneous behaviors drive multidimensional, brainwide activity. Science. 2019;364(6437):eaav7893.

219. Fiáth R, Raducanu BC, Musa S, Andrei A, Lopez CM, Van Hoof C, Ruther P, Aarts A, Horváth D, Ulbert I. A silicon-based neural probe with densely-packed low-impedance titanium nitride microelectrodes for ultrahigh-resolution in vivo recordings. Biosensors and Bioelectronics. 2018;106:86-92.

220. Steinmetz NA, Aydin C, Lebedeva A, Okun M, Pachitariu M, Bauza M, Beau M, Bhagat J, Böhm C, Broux M, Chen S, Colonell J, Gardner RJ, Karsh B, Kloosterman F, Kostadinov D, Mora-Lopez C, O'Callaghan J, Park J, Putzeys J, Sauerbrei B, van Daal RJJ, Vollan AZ, Wang S, Welkenhuysen M, Ye Z, Dudman JT, Dutta B, Hantman AW, Harris KD, Lee AK, Moser EI, O'Keefe J, Renart A, Svoboda K, Häusser M, Haesler S, Carandini M, Harris TD. Neuropixels 2.0: A miniaturized high-density probe for stable, long-term brain recordings. Science. 2021;372(6539).

221. Hanisch RJ, Farris A, Greisen EW, Pence WD, Schlesinger BM, Teuben PJ, Thompson RW, Warnock A. Definition of the flexible image transport system (FITS). Astronomy & Astrophysics. 2001;376(1):359-80.

222. Wilkinson MD, Dumontier M, Aalbersberg IJ, Appleton G, Axton M, Baak A, Blomberg N, Boiten J-W, da Silva Santos LB, Bourne PE, Bouwman J, Brookes AJ, Clark T, Crosas M, Dillo I, Dumon O, Edmunds S, Evelo CT, Finkers R, Gonzalez-Beltran A, Gray AJG, Groth P, Goble C, Grethe JS, Heringa J, 't Hoen PAC, Hooft R, Kuhn T, Kok R, Kok J, Lusher SJ, Martone ME, Mons A, Packer AL, Persson B, Rocca-Serra P, Roos M, van Schaik R, Sansone S-A, Schultes E, Sengstag T, Slater T, Strawn G, Swertz MA, Thompson M, van der Lei J, van Mulligen E, Velterop J, Waagmeester A, Wittenburg P, Wolstencroft K, Zhao J, Mons B. The FAIR Guiding Principles for scientific data management and stewardship. Scientific Data. 2016;3(1):160018.

223. Hanisch RJ, Farris A, Greisen EW, Pence WD, Schlesinger BM, Teuben PJ, Thompson RW, Warnock A. Definition of the Flexible Image Transport System (FITS)*. A&A. 2001;376(1):359-80.

224. Brun R, Rademakers F. ROOT — An object oriented data analysis framework. Nuclear Instruments and Methods in Physics Research Section A: Accelerators, Spectrometers, Detectors and Associated Equipment. 1997;389(1):81-6.

225. Rübel O, Tritt A, Ly R, Dichter BK, Ghosh S, Niu L, Baker P, Soltesz I, Ng L, Svoboda K, Frank L, Bouchard KE. The Neurodata Without Borders ecosystem for neurophysiological data science. Elife. 2022;11.

226. Griffin PC, Khadake J, LeMay KS, Lewis SE, Orchard S, Pask A, Pope B, Roessner U, Russell K, Seemann T, Treloar A, Tyagi S, Christiansen JH, Dayalan S, Gladman S, Hangartner SB, Hayden HL, Ho WWH, Keeble-Gagnère G, Korhonen PK, Neish P, Prestes PR, Richardson MF, Watson-Haigh NS, Wyres KL, Young ND, Schneider MV. Best practice data life cycle approaches for the life sciences. F1000Res. 2017;6:1618.

227. Oliver R, Andrew T, Benjamin D, Thomas B, Nicholas C, Nathan C, Thomas JD, Max D, Jean-Christophe F-R, Nile G, Michael G, Justin TK, Lawrence N, Doruk O, William S, Ivan S, Friedrich TS, Karel S, Ng L, Loren MF, Kristofer B. NWB:N 2.0: An Accessible Data Standard for Neurophysiology. bioRxiv. 2019:523035.

228. Tritt AJ, Rübel O, Dichter B, Ly R, Kang D, Chang EF, Frank LM, Bouchard K, editors. HDMF: Hierarchical Data Modeling Framework for Modern Science Data Standards. 2019 IEEE International Conference on Big Data (Big Data); 2019 9-12 Dec. 2019.

229. Horvath C, Ulbert I, Fiath R. Propagating population activity patterns during spontaneous slow waves in the thalamus of rodents. Neuroimage. 2024;285:120484.

230. Fiáth R, Márton AL, Mátyás F, Pinke D, Márton G, Tóth K, Ulbert I. Slow insertion of silicon probes improves the quality of acute neuronal recordings. Scientific Reports. 2019;9(1):111.

231. Paxinos G, Franklin, K.B.J. The mouse brain in stereotaxic coordinates, Compact 2nd ed. Amsterdam ; Boston.: Elsevier Academic Press; 2004.

232. Paxinos G, Watson, C. The rat brain in stereotaxic coordinates, 6th ed. Amsterdam ; Boston: Elsevier Academic Press; 2007.

233. Sanders JI, Kepecs A. A low-cost programmable pulse generator for physiology and behavior. Front Neuroeng. 2014;7:43.

234. van Daal RJJ, Aydin Ç, Michon F, Aarts AAA, Kraft M, Kloosterman F, Haesler S. Implantation of Neuropixels probes for chronic recording of neuronal activity in freely behaving mice and rats. Nature Protocols. 2021;16(7):3322-47.

235. Fiáth R, Beregszászi P, Horváth D, Wittner L, Aarts AA, Ruther P, Neves HP, Bokor H, Acsády L, Ulbert I. Large-scale recording of thalamocortical circuits: in vivo electrophysiology with the two-dimensional electronic depth control silicon probe. J Neurophysiol. 2016;116(5):2312-30.

236. Fiáth R, Kerekes BP, Wittner L, Tóth K, Beregszászi P, Horváth D, Ulbert I. Laminar analysis of the slow wave activity in the somatosensory cortex of anesthetized rats. Eur J Neurosci. 2016;44(3):1935-51.

237. Fiáth R, Raducanu BC, Musa S, Andrei A, Lopez CM, van Hoof C, Ruther P, Aarts A, Horváth D, Ulbert I. A silicon-based neural probe with densely-packed low-impedance titanium nitride microelectrodes for ultrahigh-resolution in vivo recordings. Biosens Bioelectron. 2018;106:86-92.

238. Fiáth R, Meszéna D, Somogyvári Z, Boda M, Barthó P, Ruther P, Ulbert I. Recording site placement on planar silicon-based probes affects signal quality in acute neuronal recordings. Scientific Reports. 2021;11(1):2028.

239. Klee JL, Kiliaan AJ, Lipponen A, Battaglia FP. Reduced firing rates of pyramidal cells in the frontal cortex of APP/PS1 can be restored by acute treatment with levetiracetam. Neurobiol Aging. 2020;96:79-86.

240. Neto JP, Lopes G, Frazão J, Nogueira J, Lacerda P, Baião P, Aarts A, Andrei A, Musa S, Fortunato E, Barquinha P, Kampff AR. Validating silicon polytrodes with paired juxtacellular recordings: method and dataset. J Neurophysiol. 2016;116(2):892-903.

241. Kocsis B, Martínez-Bellver S, Fiáth R, Domonkos A, Sviatkó K, Schlingloff D, Barthó P, Freund TF, Ulbert I, Káli S, Varga V, Hangya B. Huygens synchronization of medial septal pacemaker neurons generates hippocampal theta oscillation. Cell Rep. 2022;40(5):111149.

242. Klein L, Pothof F, Raducanu BC, Klon-Lipok J, Shapcott KA, Musa S, Andrei A, Aarts AA, Paul O, Singer W, Ruther P. High-density electrophysiological recordings in

macaque using a chronically implanted 128-channel passive silicon probe. J Neural Eng. 2020;17(2):026036.

243. Buccino AP, Hurwitz CL, Garcia S, Magland J, Siegle JH, Hurwitz R, Hennig MH. SpikeInterface, a unified framework for spike sorting. eLife. 2020;9:e61834.

244. Pachitariu M, Steinmetz N, Kadir S, Carandini M, Kenneth D H. Kilosort: realtime spike-sorting for extracellular electrophysiology with hundreds of channels. bioRxiv. 2016:061481.

245. Rossant C, Kadir SN, Goodman DFM, Schulman J, Hunter MLD, Saleem AB, Grosmark A, Belluscio M, Denfield GH, Ecker AS, Tolias AS, Solomon S, Buzsaki G, Carandini M, Harris KD. Spike sorting for large, dense electrode arrays. Nat Neurosci. 2016;19(4):634-41.

246. Szarowski DH, Andersen MD, Retterer S, Spence AJ, Isaacson M, Craighead HG, Turner JN, Shain W. Brain responses to micro-machined silicon devices. Brain Res. 2003;983(1-2):23-35.

247. Chen L, Hartner J, Dong T, Li A, Watson B, Shih A. Flexible High-Resolution Force and Dimpling Measurement System for Pia and Dura Penetration During In Vivo Microelectrode Insertion Into Rat Brain. IEEE Trans Biomed Eng. 2021;68(8):2602-12.

248. Neske GT. The Slow Oscillation in Cortical and Thalamic Networks: Mechanisms and Functions. Frontiers in Neural Circuits. 2016;9.

249. Mizuseki K, Royer S, Diba K, Buzsáki G. Activity dynamics and behavioral correlates of CA3 and CA1 hippocampal pyramidal neurons. Hippocampus. 2012;22(8):1659-80.

250. Peter CP, Joshua HS, Nicholas AS, Sara M, György B. CellExplorer: a graphical user interface and a standardized pipeline for visualizing and characterizing single neurons. bioRxiv. 2020:2020.05.07.083436.

251. Jia X, Siegle JH, Bennett C, Gale SD, Denman DJ, Koch C, Olsen SR. High-density extracellular probes reveal dendritic backpropagation and facilitate neuron classification. Journal of Neurophysiology. 2019;121(5):1831-47.

252. Robbins A, Fox S, Holmes G, Scott R, Barry J. Short duration waveforms recorded extracellularly from freely moving rats are representative of axonal activity. Frontiers in Neural Circuits. 2013;7.

253. Sun SH, Almasi A, Yunzab M, Zehra S, Hicks DG, Kameneva T, Ibbotson MR, Meffin H. Analysis of extracellular spike waveforms and associated receptive fields of neurons in cat primary visual cortex. The Journal of Physiology. 2021;599(8):2211-38.

254. Buccino AP, Hurwitz CL, Garcia S, Magland J, Siegle JH, Hurwitz R, Hennig MH. SpikeInterface, a unified framework for spike sorting. Elife. 2020;9.

255. Siegle JH, Jia X, Durand S, Gale S, Bennett C, Graddis N, Heller G, Ramirez TK, Choi H, Luviano JA, Groblewski PA, Ahmed R, Arkhipov A, Bernard A, Billeh YN, Brown D, Buice MA, Cain N, Caldejon S, Casal L, Cho A, Chvilicek M, Cox TC, Dai K, Denman DJ, de Vries SEJ, Dietzman R, Esposito L, Farrell C, Feng D, Galbraith J, Garrett M, Gelfand EC, Hancock N, Harris JA, Howard R, Hu B, Hytnen R, Iyer R, Jessett E, Johnson K, Kato I, Kiggins J, Lambert S, Lecoq J, Ledochowitsch P, Lee JH, Leon A, Li Y, Liang E, Long F, Mace K, Melchior J, Millman D, Mollenkopf T, Nayan C, Ng L, Ngo K, Nguyen T, Nicovich PR, North K, Ocker GK, Ollerenshaw D, Oliver M, Pachitariu M, Perkins J, Reding M, Reid D, Robertson M, Ronellenfitch K, Seid S, Slaughterbeck C, Stoecklin M, Sullivan D, Sutton B, Swapp J, Thompson C, Turner K, Wakeman W, Whitesell JD, Williams D, Williford A, Young R, Zeng H, Naylor S, Phillips JW, Reid RC, Mihalas S, Olsen SR, Koch C. Survey of spiking in the mouse visual system reveals functional hierarchy. Nature. 2021;592(7852):86-92.

256. Daniel NH, Samar BM, David K. Quality Metrics to Accompany Spike Sorting of Extracellular Signals. The Journal of Neuroscience. 2011;31(24):8699.

257. Schmitzer-Torbert N, Jackson J, Henze D, Harris K, Redish AD. Quantitative measures of cluster quality for use in extracellular recordings. Neuroscience. 2005;131(1):1-11.

258. Harris KD, Hirase H, Leinekugel X, Henze DA, Buzsáki G. Temporal Interaction between Single Spikes and Complex Spike Bursts in Hippocampal Pyramidal Cells. Neuron. 2001;32(1):141-9.

259. Schmitzer-Torbert N, Redish AD. Neuronal activity in the rodent dorsal striatum in sequential navigation: separation of spatial and reward responses on the multiple T task. J Neurophysiol. 2004;91(5):2259-72.
260. Chung JE, Magland JF, Barnett AH, Tolosa VM, Tooker AC, Lee KY, Shah KG, Felix SH, Frank LM, Greengard LF. A Fully Automated Approach to Spike Sorting. Neuron. 2017;95(6):1381-94.e6.
261. Rousseeuw PJ. Silhouettes: A graphical aid to the interpretation and validation of cluster analysis. Journal of Computational and Applied Mathematics. 1987;20:53-65.
262. Buccino AP, Kordovan M, Ness TV, Merkt B, Häfliger PD, Fyhn M, Cauwenberghs G, Rotter S, Einevoll GT. Combining biophysical modeling and deep learning for multielectrode array neuron localization and classification. Journal of neurophysiology. 2018;120(3):1212-32.
263. Fiáth R, Kerekes BP, Wittner L, Tóth K, Beregszászi P, Horváth D, Ulbert I. Laminar analysis of the slow wave activity in the somatosensory cortex of anesthetized rats. European Journal of Neuroscience. 2016;44(3):1935-51.
264. Horváth C TL, Ulbert I, Fiáth R. Dataset of cortical activity recorded with high spatial resolution from anesthetized rats. G-Node.
265. Sharma AV, Wolansky T, Dickson CT. A comparison of sleeplike slow oscillations in the hippocampus under ketamine and urethane anesthesia. J Neurophysiol. 2010;104(2):932-9.
266. Yulia B, Yael A, Alexander GG, Carl RS, Harvey AS. Dendritic Backpropagation and the State of the Awake Neocortex. The Journal of Neuroscience. 2007;27(35):9392.
267. Buzsáki G, Mizuseki K. The log-dynamic brain: how skewed distributions affect network operations. Nature Reviews Neuroscience. 2014;15(4):264-78.
268. Fiáth R, Raducanu BC, Musa S, Andrei A, Lopez CM, Welkenhuysen M, Ruther P, Aarts A, Ulbert I. Fine-scale mapping of cortical laminar activity during sleep slow oscillations using high-density linear silicon probes. Journal of Neuroscience Methods. 2019;316:58-70.
269. Crunelli V, David F, Lőrincz ML, Hughes SW. The thalamocortical network as a single slow wave-generating unit. Curr Opin Neurobiol. 2015;31:72-80.

270. Ferezou I, Haiss F, Gentet LJ, Aronoff R, Weber B, Petersen CC. Spatiotemporal dynamics of cortical sensorimotor integration in behaving mice. Neuron. 2007;56(5):907-23.
271. Vyazovskiy VV, Faraguna U, Cirelli C, Tononi G. Triggering slow waves during NREM sleep in the rat by intracortical electrical stimulation: effects of sleep/wake history and background activity. J Neurophysiol. 2009;101(4):1921-31.
272. Wanger T, Takagaki K, Lippert MT, Goldschmidt J, Ohl FW. Wave propagation of cortical population activity under urethane anesthesia is state dependent. BMC Neuroscience. 2013;14(1):78.
273. Han F, Caporale N, Dan Y. Reverberation of recent visual experience in spontaneous cortical waves. Neuron. 2008;60(2):321-7.
274. Reig R, Mattia M, Compte A, Belmonte C, Sanchez-Vives MV. Temperature Modulation of Slow and Fast Cortical Rhythms. Journal of Neurophysiology. 2010;103(3):1253-61.
275. Bourassa J, Pinault D, Deschênes M. Corticothalamic Projections from the Cortical Barrel Field to the Somatosensory Thalamus in Rats: A Single-fibre Study Using Biocytin as an Anterograde Tracer. European Journal of Neuroscience. 1995;7(1):19-30.
276. Hoogland PV, Welker E, Van der Loos H. Organization of the projections from barrel cortex to thalamus in mice studied with Phaseolus vulgaris-leucoagglutinin and HRP. Exp Brain Res. 1987;68(1):73-87.
277. Veinante P, Lavallée P, Deschênes M. Corticothalamic projections from layer 5 of the vibrissal barrel cortex in the rat. J Comp Neurol. 2000;424(2):197-204.
278. Beltramo R, D'Urso G, Dal Maschio M, Farisello P, Bovetti S, Clovis Y, Lassi G, Tucci V, De Pietri Tonelli D, Fellin T. Layer-specific excitatory circuits differentially control recurrent network dynamics in the neocortex. Nature Neuroscience. 2013;16(2):227-34.
279. Wester JC, Contreras D. Columnar interactions determine horizontal propagation of recurrent network activity in neocortex. J Neurosci. 2012;32(16):5454-71.
280. Liang Y, Liang J, Song C, Liu M, Knöpfel T, Gong P, Zhou C. Complexity of cortical wave patterns of the wake mouse cortex. Nature Communications. 2023;14(1):1434.

9 Bibliography of the candidate's publications

Publications connected to the thesis

Horváth, C., I. Ulbert and R. Fiáth (2024). "Propagating population activity patterns during spontaneous slow waves in the thalamus of rodents." NeuroImage **285**: 120484.

Horváth C, Tóth LF, Ulbert I, Fiáth R. Dataset of cortical activity recorded with high spatial resolution from anesthetized rats. Scientific Data. 2021;8(1):180.

Publications not related to the thesis

C Horváth, K Csikós, B Árkossy, E Klein, P Ruther, I Ulbert and R Fiáth. Polymer-based laminar probes with an ultra-long flexible spiral-shaped cable for in vivo neural recordings. SENSORS *AND ACTUATORS B: CHEMICAL*, 136220, 2024.

10 Acknowledgments

I am deeply thankful to my supervisor, Dr. Richárd Fiáth, for his professional support over the years and for giving me the opportunity to conduct my doctoral studies within the Integrative Neuroscience Research Group. I also extend my sincere gratitude to the members of the Ulbert Lab at the Research Centre for Natural Sciences for cultivating such an excellent working environment. Last but not least, I owe my parents and my partner a debt of gratitude for their immeasurable support and endless patience.